

THESIS FOR THE DEGREE OF DOCTOR OF PHILOSOPHY

Graphene spin circuits and spin-orbit phenomena  
in van der Waals heterostructures with  
topological insulators

DMITRII KHOKHRIAKOV

Department of Microtechnology and Nanoscience (MC2)

*Quantum Device Physics Laboratory*

CHALMERS UNIVERSITY OF TECHNOLOGY

Göteborg, Sweden 2021

Graphene spin circuits and spin-orbit phenomena in van der Waals heterostructures with topological insulators

DMITRII KHOKHRIAKOV

Göteborg, Sweden 2021

ISBN 978-91-7905-470-0

COPYRIGHT © DMITRII KHOKHRIAKOV, 2021

Doktorsavhandlingar vid Chalmers tekniska högskola

Ny serie Nr 4937

ISSN 0346-718X

Quantum Device Physics Laboratory

Department of Microtechnology and Nanoscience (MC2)

Chalmers University of Technology

SE-412 96 Göteborg, Sweden

Telephone: +46 (0)31-772 1000

## Cover

Artistic drawings of a graphene-based majority spin logic gate and spin-charge conversion by spin-galvanic effect in a graphene-topological insulator heterostructure.

Printed by Chalmers Reproservice

Göteborg, Sweden 2021

Graphene spin circuits and spin-orbit phenomena in van der Waals heterostructures with topological insulators  
Thesis for the degree of Doctor of Philosophy  
DMITRII KHOKHRIAKOV  
Quantum Device Physics Laboratory  
Department of Microtechnology and Nanoscience (MC2)  
Chalmers University of Technology

## ABSTRACT

Spintronics offers an alternative approach to conventional charge-based information processing by using the electron spin for next-generation non-volatile memory and logic technologies. To realize such technologies, it is necessary to develop spin-polarized current sources, spin interconnects, charge-to-spin conversion processes, and gate-tunable spintronic functionalities. The recently emerged two-dimensional (2D) and topological materials represent a promising platform to realize such spin-based phenomena. Due to its small spin-orbit coupling (SOC), graphene was predicted to preserve electron spin coherence for a long time, making it an ideal material for spin communication. In contrast, topological insulators (TIs) have high SOC and develop a nontrivial band structure with insulating bulk but conducting spin-polarized surface states. Combining these materials in van der Waals heterostructures has been predicted to give rise to unique proximity-induced spin-orbit phenomena that may be used for electrical control of spin polarization.

In this thesis, we experimentally prove that the large-area chemical vapor deposited (CVD) graphene is an excellent material choice for the realization of robust spin interconnects, which are capable of spin communication over channel lengths exceeding 34  $\mu\text{m}$ . Utilizing such graphene, we realize a spin summation operation in multiterminal devices and employ it to construct a prototype spin majority logic gate operating with pure spin currents. In topological insulators, we electrically detect the spin-momentum locking and reveal how the bulk and surface conducting channels affect the charge-to-spin conversion efficiency. Finally, by combining graphene and TIs in hybrid devices, we confirm the emergence of a strong proximity-induced SOC with a Rashba spin texture in graphene. We further show that in such heterostructures a spin-charge conversion capability is induced in graphene via the spin-galvanic effect at room temperature and reveal its strong tunability in magnitude and sign by the gate voltage. These findings demonstrate the robust performance of graphene as a spin interconnect for emerging spin-logic architectures and present all-electrical and gate-tunable spintronic devices based on graphene-TI heterostructures, paving the way for next-generation spin-based computing.

**Keywords:** Spintronics, Graphene, Topological insulator, Van der Waals heterostructures, Proximity effect, Spin-charge conversion



# ACKNOWLEDGEMENTS

I would like to express my deepest gratitude to my supervisor Professor Saroj Prasad Dash. Thank you for giving me the opportunity to carry out this PhD work in your group, and for dedicating much of your time to discussing the ideas and results. Your positive attitude and the habit to look on the bright side of things were really inspiring throughout these years.

Thank you André Dankert for your valuable mentorship at the beginning of my PhD. I learned a lot from you about the device fabrication and measurement techniques, and all the practical aspects to keep the lab in order.

I also want to thank my current and previous colleagues in the spintronics group. Bogdan Karpiak, Anamul Md. Hoque, Bing Zhao, and Priyamvada Bhaskar, thank you for all the valuable discussions, support, and company. In addition, during my project, I had the honor to supervise and work together with many master students, who significantly contributed to my thesis. For this, I thank Isabel Harrysson Rodrigues, Linnea Andersson, Jianyang Zhao, Arimande Engström, and Lars Sjöström.

I would like to thank Dag Winkler, Tomas Löfwander, Avgust Yurgens, Per Lundgren, Alexei Kalaboukhov, Annika Holtringer, Susannah Carlsson, Linda Brånell, Debora Perlheden, Maria Tremblay, Floriana Lombardi, Andrey Danilov, Attila Geresdi, Tord Claeson, Samuel Lara Avila, Janine Splettstoesser, Thilo Bauch, Åsa Haglund, Sergey Kubatkin, and Mikael Fogelström for the examination of the project and the assistance with administrative and other matters. I would also like to thank all the colleagues at QDP and MC2 for creating a pleasant working environment.

Much of the thesis work was performed in the cleanroom, and I want to thank the staff of the Nanofabrication Laboratory for always being happy to help and having the patience to answer all of my questions about the tools. A special thanks goes to Niclas Lindvall, Marcus Rommel, Henrik Frederiksen, and Mahdad Sadeghi. Also, I thank Lars Jönsson for the help with hardware in the lab.

I am grateful for the useful discussions and fruitful collaboration with the group of Professor Stephan Roche.

I would like to thank my family for their endless care and support, and the old and new friends for making this chapter of my life as happy and exciting as it was. Specially, thank you Filip for always being by my side, Pontus for all the fun board games, and Jasper for the wonderful hikes and a great ski trip.

Finally, I would like to acknowledge the financial support of this doctoral program from the Swedish Research council and the Graphene Flagship. In addition, I would like to thank the consortium of the Erasmus Mundus Master of Nanoscience and Nanotechnology program for providing me with a scholarship during my master thesis, without which I would not have been able to enroll at Chalmers in the first place.



## LIST OF PUBLICATIONS

This thesis is mainly based on the work reported in the following appended papers:

- [I] D. Khokhriakov, B. Karpiak, A. M. Hoque, B. Zhao, S. Parui, and S. P. Dash, “Robust Spin Interconnect with Isotropic Spin Dynamics in Chemical Vapor Deposited Graphene Layers and Boundaries”, *ACS Nano* **14**, 15864–15873 (2020).
- [II] D. Khokhriakov, B. Karpiak, A. M. Hoque, and S. P. Dash, “Two-dimensional spintronic circuit architectures on large scale graphene”, *Carbon* **161**, 892–899 (2020).
- [III] A. Dankert, P. Bhaskar, D. Khokhriakov, I. H. Rodrigues, B. Karpiak, M. V. Kamalakar, S. Charpentier, I. Garate, and S. P. Dash, “Origin and evolution of surface spin current in topological insulators”, *Physical Review B* **97**, 125414 (2018).
- [IV] D. Khokhriakov, A. W. Cummings, K. Song, M. Vila, B. Karpiak, A. Dankert, S. Roche, and S. P. Dash, “Tailoring emergent spin phenomena in Dirac material heterostructures”, *Science Advances* **4**, eaat9349 (2018).
- [V] D. Khokhriakov, A. M. Hoque, B. Karpiak, and S. P. Dash, “Gate-tunable spin-galvanic effect in graphene-topological insulator van der Waals heterostructures at room temperature”, *Nature Communications* **11**, 3657 (2020).

Other publications not included in the thesis:

- B. Zhao, B. Karpiak, D. Khokhriakov, A. Johansson, A. M. Hoque, X. Xu, Y. Jiang, I. Mertig, and S. P. Dash, “Unconventional Charge-Spin Conversion in Weyl-Semimetal WTe<sub>2</sub>”, *Advanced Materials* **32**, 2000818 (2020).
- B. Zhao, D. Khokhriakov, Y. Zhang, H. Fu, B. Karpiak, A. M. Hoque, X. Xu, Y. Jiang, B. Yan, and S. P. Dash, “Observation of charge to spin conversion in Weyl semimetal WTe<sub>2</sub> at room temperature”, *Physical Review Research* **2**, 013286 (2020).
- A. M. Hoque, D. Khokhriakov, B. Karpiak, and S. P. Dash, “Charge-spin conversion in layered semimetal TaTe<sub>2</sub> and spin injection in van der Waals heterostructures”, *Physical Review Research* **2**, 033204 (2020).
- B. Zhao, A. M. Hoque, D. Khokhriakov, B. Karpiak, and S. P. Dash, “Charge-spin conversion signal in WTe<sub>2</sub> van der Waals hybrid devices with a geometrical design”, *Applied Physics Letters* **117**, 242401 (2020).
- B. Karpiak, A. W. Cummings, K. Zollner, M. Vila, D. Khokhriakov, A. M. Hoque, A. Dankert, P. Svedlindh, J. Fabian, S. Roche, and S. P. Dash, “Magnetic proximity in a van der Waals heterostructure of magnetic insulator and graphene”, *2D Materials* **7**, 015026 (2019).
- B. Zhao, D. Khokhriakov, B. Karpiak, A. M. Hoque, L. Xu, L. Shen, Y. P. Feng, X. Xu, Y. Jiang, and S. P. Dash, “Electrically controlled spin-switch and evolution of Hanle spin precession in graphene”, *2D Materials* **6**, 035042 (2019).
- B. Irfan, A. Dankert, P. Bhasker, D. Khokhriakov, S. P. Dash, and R. Chatterjee, “Surface dominated magnetotransport in Bi<sub>2</sub>Te<sub>2.15</sub>Se<sub>0.85</sub> topological insulator”, *Journal of Applied Physics* **124**, 214302 (2018).



# GLOSSARY

## Abbreviations

2D	Two-dimensional
3D	Three-dimensional
AMR	Anisotropic magnetoresistance
ARPES	Angle resolved photoemission spectroscopy
BS	$\text{Bi}_2\text{Se}_3$
BSTS	$\text{Bi}_{1.5}\text{Sb}_{0.5}\text{Te}_{1.7}\text{Se}_{1.3}$
BLG	Bilayer graphene
CVD	Chemical vapor deposition
CNP	Charge neutrality point
DFT	Density functional theory
DOS	Density of states
DP	D'yakonov-Perel'
EY	Elliott-Yafet
FM	Ferromagnet
Gr	Graphene
GMR	Giant magnetoresistance
HDD	Hard disc drive
hBN	Hexagonal boron nitride
HS	Heterostructure
ISHE	Inverse spin Hall effect
MTJ	Magnetic tunnel junction
NM	Nonmagnet
PIA	Pseudospin inversion asymmetry
QL	Quintuple layer
QAHE	Quantum anomalous Hall effect
SOC	Spin-orbit coupling
SEM	Scanning electron microscope
SML	Spin-momentum locking
SV	Spin valve
SHE	Spin Hall effect
SCC	Spin-charge conversion
SGE	Spin-galvanic effect
SLG	Single-layer graphene
STT	Spin transfer torque
SOT	Spin-orbit torque
TI	Topological insulator
TMR	Tunnel magnetoresistance

TB	Tunnel barrier
TMD	Transition metal dichalcogenide
TRS	Time reversal symmetry
TLG	Trilayer graphene
VZ	Valley-Zeeman
WAL	Weak antilocalization
WL	Weak localization

## Symbols

$L$	Channel length
$\tau_s$	Spin lifetime
$\tau_p$	Momentum scattering time
$N_{\uparrow\downarrow}$	Spin-dependent available states
$P$	Spin polarization
$P_i$	Injector spin polarization
$P_d$	Detector spin polarization
$\sigma$	Conductivity
$\sigma_0$	Residual conductivity
$\sigma_{\uparrow\downarrow}$	Spin-dependent conductivity
$R_P$	Resistance for parallel magnetization orientation
$R_{AP}$	Resistance for antiparallel magnetization orientation
$D_s$	Spin diffusion coefficient
$D_c$	Charge diffusion coefficient
$d_c$	Critical HgTe thickness
$\lambda_s$	Spin diffusion length
$\widetilde{\lambda}_s$	Complex renormalization of the spin diffusion length
$n$	Carrier concentration
$n^*$	Residual carrier concentration
$n_s$	Spin density
$\mu$	Mobility
$t$	Dielectric thickness
$V$	Voltage
$V_g$	Gate voltage
$V_0$	Offset voltage
$V_{NL}$	Nonlocal voltage
$V_{NL}^P$	Nonlocal voltage for parallel magnetization orientation
$V_{NL}^{AP}$	Nonlocal voltage for antiparallel magnetization orientation
$E_F$	Fermi energy
$v_F$	Fermi velocity
$\nu$	Density of states
$\ell_{\text{mfp}}$	Mean free path
$\mu_{\uparrow\downarrow}$	Spin-dependent electrochemical potential

$I$	Bias current
$W$	Channel width
$\Omega$	Spin relaxation matrix
$\omega_L$	Larmor spin precession frequency
$g$	Landé factor
$B$	Magnetic field
$B_{\parallel}$	Magnetic field parallel to the easy magnetization direction
$B_{\perp}$	Out-of-plane magnetic field
$T$	Temperature
$\lambda$	SOC strength
$k$	Electron wave vector
$\xi$	Spin lifetime anisotropy ratio
$\tau_{\perp}$	Lifetime of out-of-plane spins
$\tau_{\parallel}$	Lifetime of in-plane spins
$\theta$	Spin Hall angle
$\alpha$	Conversion efficiency of the spin-galvanic effect
$R_s^{gr}$	Graphene channel spin resistance
$\Delta_{\text{EY}}$	Effective SOC strength of EY mechanism
$\Delta_{\text{DP}}$	Effective SOC strength of DP mechanism
$\beta$	Angle of the magnetic field
$\ell_{\phi}$	Phase coherence length
$R_{\text{sq}}$	Sheet resistance of graphene
$\lambda_{\text{IEE}}$	Inverse Edelstein effect length

## Constants

$e$	Electron charge: $e = 1.602\,176 \times 10^{-19} \text{ C}$
$\varepsilon$	Relative dielectric constant: $\varepsilon_{\text{SiO}_2} = 3.9$
$\varepsilon_0$	Vacuum dielectric constant: $\varepsilon_0 = 8.854\,187 \times 10^{-12} \text{ F m}^{-1}$
$h$	Planck's constant: $h = 6.626\,070 \times 10^{-34} \text{ J s} = 4.135\,667 \times 10^{-15} \text{ eV s}$
$\hbar$	Reduced Planck's constant: $\hbar = 1.054\,571 \times 10^{-34} \text{ J s} = 6.582\,119 \times 10^{-16} \text{ eV s}$
$\mu_B$	Bohr magneton: $\mu_B = 9.274\,009 \times 10^{-24} \text{ J T}^{-1}$



# CONTENTS

<b>Abstract</b>	<b>iii</b>
<b>Acknowledgements</b>	<b>v</b>
<b>List of publications</b>	<b>vii</b>
<b>Glossary</b>	<b>ix</b>
<b>Contents</b>	<b>xiii</b>
<b>1 Introduction</b>	<b>1</b>
<b>2 Background</b>	<b>5</b>
2.1 Spin polarization . . . . .	5
2.2 Spin injection . . . . .	6
2.3 Spin-orbit coupling and spin relaxation . . . . .	7
2.4 Graphene . . . . .	8
2.5 Nonlocal spin transport . . . . .	10
2.6 Topological insulators . . . . .	12
<b>3 State of the art</b>	<b>15</b>
3.1 Graphene spintronics . . . . .	15
3.1.1 Spin transport in graphene . . . . .	15
3.1.2 Graphene for spin logic . . . . .	20
3.2 Topological insulators . . . . .	23
3.3 Proximity effects in Gr-TMD heterostructures . . . . .	27
3.3.1 Quantum transport and magnetotransport . . . . .	27
3.3.2 Spin transport . . . . .	29
3.3.3 Spin lifetime anisotropy . . . . .	30
3.3.4 Spin-charge conversion . . . . .	33
3.4 Heterostructures of graphene and TIs . . . . .	38
3.4.1 Band hybridization and proximity-induced spin textures . .	38
3.4.2 Electrical characterization of Gr-TI HSs . . . . .	40
<b>4 Graphene-based spintronic devices</b>	<b>45</b>
4.1 Graphene for robust spin interconnects . . . . .	45
4.1.1 Spin transport across CVD graphene layer boundaries . . .	45

4.1.2	Isotropic spin dynamics in inhomogeneous graphene channels	48
4.2	Spintronic circuit architectures for spin logic applications	50
4.2.1	Spin transport in large-area multiterminal devices	50
4.2.2	Spin majority logic gate	53
<b>5</b>	<b>Graphene-topological insulator heterostructures</b>	<b>59</b>
5.1	Spin-momentum locking in topological insulators	59
5.1.1	Detection of spin-momentum locking via spin precession	63
5.2	Proximity-induced spin-orbit coupling in graphene-topological insulator heterostructures	66
5.3	Spin-galvanic effect in graphene-topological insulator heterostructures	70
5.3.1	SGE detection by magnetization rotation	70
5.3.2	SGE detection by spin-switch and spin precession	72
<b>6</b>	<b>Summary and Outlook</b>	<b>77</b>
	<b>References</b>	<b>81</b>
	<b>Appended papers</b>	<b>99</b>
	<b>Paper I</b>	<b>101</b>
	<b>Paper II</b>	<b>117</b>
	<b>Paper III</b>	<b>135</b>
	<b>Paper IV</b>	<b>145</b>
	<b>Paper V</b>	<b>167</b>

# 1 Introduction

The invention of a semiconductor transistor in 1947 was one of the most important achievements in human history. These devices became the basic building blocks in modern electronics, sparked the field of electronic data processing, and marked the beginning of the Information Age. Nowadays, electronics has revolutionized almost all areas of our society, where microcontrollers, computers, and artificial intelligence are widely used for automation, home appliances, medicine, transportation, navigation, communications, and entertainment.

The remarkable pace of the technological advancement in the electronics industry over the last 70 years, driven by the ever-increasing demands for faster processing rates, improved power efficiency, and larger information storage capacity, was made possible by the developments in condensed matter physics and the progress in semiconductor manufacturing technology. It was noticed that the number of transistors per unit area on a chip doubles approximately every 2 years, an empirical trend known as Moore's law [1]. This exponential growth was maintained by a continuous shrinking of the transistor dimensions over the past decades. However, it is believed that in the near future this trend could no longer be sustained as the minimum feature size of nanoelectronic components approaches the fundamental atomic limit. In addition, in such small devices, quantum mechanical effects lead to increased leakage currents that pose heat dissipation and power consumption issues. To cope with these issues and continue the development of electronics beyond Moore's law, alternative routes and prospective architectures for future computing electronic devices are being investigated.

Spintronics offers an alternative approach to conventional charge-based information processing by using the quantum mechanical spin of electrons to record, store, transfer, and manipulate information [2]. The spin of an electron is its intrinsic angular momentum that governs magnetic interactions of individual particles via the associated magnetic moment. Being the quantized degree of freedom, it can take only two discrete values that are referred to as spin-up ( $\uparrow$ ) and spin-down ( $\downarrow$ ), which can be alternatives to the ON and OFF states in conventional transistors. Due to the relatively small amount of energy needed to change the spin state of an electron, this approach can yield computing devices with decreased power consumption and increased operation speed owing to the integration of spin-based non-volatile memory and logic [3–5].

The unpaired spins in magnetic materials give rise to their macroscopic magnetization properties. To describe the magnetoresistance phenomenon in ferro-

magnetic metals, the notion of asymmetric scattering in spin-up and spin-down conducting channels was first introduced by Mott in 1936 [6]. Later, this approach was also utilized to explain the giant magnetoresistance (GMR) [7, 8] and tunnel magnetoresistance (TMR) [9, 10] effects discovered in thin magnetic films separated by thin nonmagnetic layers. These effects offered a convenient way to electrically read the magnetization states of ferromagnets and rapidly revolutionized the computer memory industry where they were incorporated into the read heads in hard disc drives (HDDs), which allowed a dramatic increase in data storage density. These remarkable discoveries established the research field of spintronics, provided first-generation spintronic devices to the market, and were honored by a Nobel prize in 2007.

Besides applications in computer memory, spintronics research also strives to realize information transfer and processing in the spin domain. The first proposal for a spin field-effect transistor was given by Datta and Das in 1990 [11]. The proposed device was comprised of ferromagnetic source and drain contacts connected by a spin-coherent channel, where the polarization of the propagating spins can be controlled by the gate electric field via tunable spin-orbit coupling. Since then, various materials have been investigated to develop long-distance spin transport in nonmagnetic channels, efficient spin injection and detection, and spin manipulation. A good spin interconnect should retain the injected spin polarization over sufficiently long time and length scales, which are characterized by spin lifetime  $\tau_s$  and spin diffusion length  $\lambda_s$ . Initial studies could demonstrate spin injection from ferromagnetic materials into conventional metals [12, 13] and semiconductors [14, 15], yet the room-temperature spin transport parameters were limited.

In recent years, the field of spintronics experienced a notable boost with the advent of a new family of two-dimensional materials. Graphene is the first isolated single-layer material, initially obtained by mechanical exfoliation in 2004 [16]. It consists of carbon atoms arranged in a hexagonal lattice and exhibits a plethora of extraordinary electrical, mechanical, and optical properties stemming from its ultimate thickness and unprecedented surface to volume ratio [17]. It is a semimetal described by linear energy dispersion hosting massless Dirac fermions with ultra-high mobility [18]. This discovery of a new condensed matter system with rich physics was honored by a Nobel prize in 2010. Graphene has also become one of the central materials in spintronics since the first spin transport experiments revealed its excellent spintronic capabilities with remarkably long spin lifetime and spin diffusion length [19]. Owing to its low intrinsic spin-orbit coupling (SOC), state-of-the-art devices could achieve lifetimes  $\tau_s > 12$  ns in exfoliated graphene, and CVD graphene was shown to support spin transport for distances  $L > 30$   $\mu\text{m}$  at room temperature [20, 21]. However, this low SOC does not allow to achieve active control over spin polarization using the electric field in pristine graphene.

With the expansion of the 2D materials family with semiconducting transition metal dichalcogenides (TMDs), insulating hexagonal boron nitride (hBN), mag-



netic layers, and novel topological states of matter such as topological insulators (TIs) and Dirac and Weyl semimetals, novel device structures and functionalities became possible [22, 23]. Unlike graphene, TMDs and TIs are usually comprised of heavy elements that possess large SOC, which can potentially be utilized in spintronics to achieve spin manipulation [24]. In this respect, topological insulators are especially interesting since their high intrinsic SOC causes the inversion of the band structure, which leads to the emergence of topologically protected conducting states on their surface whereas the bulk stays insulating [25]. Moreover, these surface states host massless Dirac fermions with a unique helical spin texture that locks electron spin perpendicularly to its momentum, a phenomenon called the spin-momentum locking (SML). Because of this, topological materials are promising for spin-charge conversion and spin-orbit torque magnetization switching with applications in magnetic memory, whereas the robustness of their conductive states against defects, provided by their nontrivial topological order, is favorable for applications in future electronics. The theoretical discoveries of such topological phases of matter were honored by a Nobel prize in 2016.

Besides the intriguing properties of individual 2D materials, their layered structure allows to stack arbitrary layers on top of each other to form van der Waals heterostructures with ultra-sharp and clean interfaces without the need for matching lattice constants [26–28]. These hybrid systems offer an attractive approach to design complex structures with tailored properties, which can exhibit physical effects unobtainable in isolated materials. Following this approach to combine high-SOC materials in heterostructures with graphene can provide a convenient way to utilize both the good spin transport properties of graphene and spin-orbit effects of heavy materials in a single device, enabling novel functionalities for emerging spintronic applications and next-generation devices.

The research activities performed in this thesis can be divided into two main lines. First, we investigated the spin transport properties of large-area CVD graphene to assess the role of its intrinsic inhomogeneities, study the spin diffusion in branched channels with non-collinear ferromagnets, and realize a prototype spin majority logic gate. Second, we studied spin-orbit proximity effects in heterostructures of graphene and topological insulators to demonstrate the emergence of an increased SOC and spin-charge conversion by the spin-galvanic effect in graphene. Because of this, the thesis is structured as follows: Chapter 2 introduces basic concepts and describes the theory behind common spin transport techniques and experiments. Chapter 3 provides a comprehensive overview of the state-of-the-art in the field of spintronics with graphene, topological insulators, and van der Waals heterostructures. In chapter 4 we combine the results of spin transport experiments performed in large-area CVD graphene. In particular, section 4.1 summarizes the results presented in paper I, where spin transport experiments across multilayer channels and layer boundaries in CVD graphene revealed its robust performance as a spin interconnect with isotropic spin dy-

namics at room temperature. Section 4.2 studies spin transport in multiterminal branched CVD graphene channels, which were found to preserve spin polarization over distances exceeding  $34\text{ }\mu\text{m}$ . In addition, the appearance of the symmetric and antisymmetric components in the Hanle spin precession signals was investigated in devices with noncollinear arrangements of ferromagnetic electrodes, as presented in paper II. Furthermore, a spin summation operation due to spin mixing in graphene was realized and employed to construct a prototype spin majority gate operating with pure diffusive spin currents. Chapter 5 summarizes the studies of graphene-TI heterostructures, where we focused on proximity-induced effects related to spin-orbit coupling. In particular, section 5.1 is based on results presented in paper III, where we studied the spin and quantum transport in the topological insulator BSTS, and performed the electrical detection of the spin-momentum locking in surface states of the TI. In addition, the charge-spin conversion signal was confirmed in spin precession measurements utilizing spin injection from the TI into the graphene at room temperature. Section 5.2 summarizes the results of spin transport experiments in Gr-TI heterostructures which are detailed in paper IV. The emergence of an enhanced SOC in proximitized graphene of  $\sim 1\text{ meV}$  was confirmed, exceeding the values seen in the pristine material by an order of magnitude. Section 5.3 expands the results presented in paper V, describing spin-charge conversion functionality induced in the graphene via the spin-galvanic effect (SGE) in Gr-TI heterostructures. The SGE is detected in multiple device configurations by various experimental signatures including the magnetization rotation, spin-switch, and Hanle spin precession measurements. Importantly, the spin-galvanic signal is shown to be strongly tunable in both magnitude and sign by the gate electric field. Finally, chapter 6 summarizes the obtained results and provides an outlook on possible directions for future studies in the field of spintronics with 2D materials.

## 2 Background

This chapter introduces the basic concepts of spintronics upon which this thesis is built. It discusses the notion of spin polarization in magnetic and nonmagnetic materials, introduces the tunneling magnetoresistance, describes the processes of spin injection, transport, and detection, and outlines the common modes of spin relaxation. In addition, it introduces the graphene and topological insulators, and discusses their properties relevant for spintronics.

### 2.1 Spin polarization

The use of the spin degree of freedom of electrons in addition to their charge opens numerous routes towards increasing the efficiency and functionality of future electronic devices. To realize this concept, it is necessary to understand spin lifetime, spin dynamics, and spin-dependent interactions in various materials, as well as to develop efficient approaches for the creation, transport, and control of information in the spin domain. To study these spintronic phenomena, most experiments rely on the creation of nonequilibrium spin accumulation in nonmagnetic materials.

For this, the most commonly used method involves the electrical injection of spins from a spin-polarized source, most often being a ferromagnetic (FM) material. In FMs, magnetism stems from the unpaired spins of electrons as they populate the available energy states according to the Pauli exclusion principle and Hund's rules to achieve the lowest energy state. Since the electrons tend to first occupy available states individually before pairing with opposite spins, unpaired spin states add up to a significant magnetic moment of the atom. This results in a splitting of the density of states (DOS) at the Fermi level, where the number of available states for majority spins (say, spin-up)  $N_{\uparrow}$  is larger than for the minority spin orientation (spin-down)  $N_{\downarrow}$ . This allows to define the spin polarization of a ferromagnet as

$$P = \frac{N_{\uparrow} - N_{\downarrow}}{N_{\uparrow} + N_{\downarrow}}. \quad (2.1)$$

The asymmetry between the two spin species was first pointed out by Mott in 1936, when he proposed the two-current model where the total conductivity of the system  $\sigma$  is comprised of the independent and unequal contributions of the spin-up  $\sigma_{\uparrow}$  and spin-down  $\sigma_{\downarrow}$  conducting channels:  $\sigma = \sigma_{\downarrow} + \sigma_{\uparrow}$ , associating the notion of spin polarization with electron current [6, 29]. All magnetic metals,

semiconductors, and insulators, as well as their interfaces with each other and with other non-magnetic materials, exhibit spin-dependent conductivity with the polarization of electron current expressed as

$$P = \frac{\sigma_{\uparrow} - \sigma_{\downarrow}}{\sigma_{\uparrow} + \sigma_{\downarrow}}. \quad (2.2)$$

Polarization values were experimentally obtained for common ferromagnetic metals Fe (45%), Co (42%), Ni (43%), and permalloy  $\text{Ni}_{0.8}\text{Fe}_{0.2}$  (37%) [30].

## 2.2 Spin injection

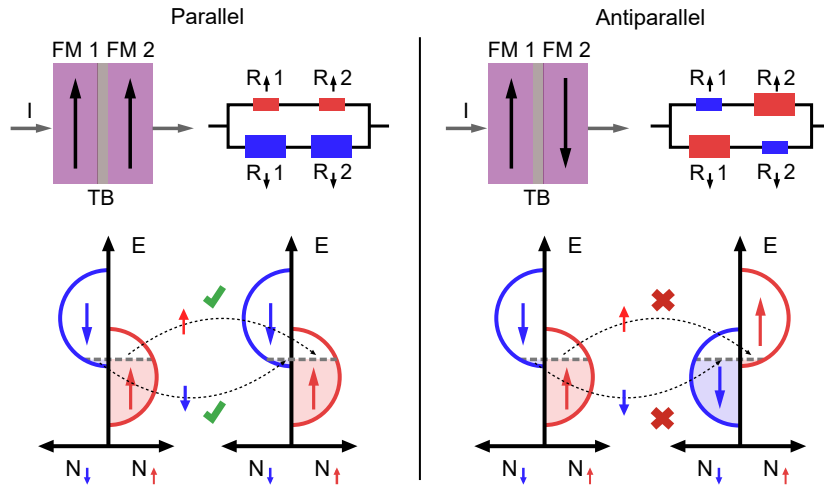


**Figure 2.1:** Electron tunneling in an MTJ comprised of two ferromagnetic layers separated by an insulating tunneling barrier. Schematics show the two-channel resistor model and the spin-resolved density of states for the parallel and antiparallel orientation of FM magnetizations, corresponding to the overall low and high resistance states respectively.

By passing an electron current through a FM/NM interface, a nonequilibrium spin accumulation could be injected in a normal metal for the first time by Jonson and Silsbee in 1985, where they also observed spin precession [31]. Shortly after, the giant magnetoresistance (GMR) effect was discovered by Albert Fert and Peter Grünberg in their studies of thin ferromagnet-normal metal-ferromagnet layers, where the resistance of the stack was shown to be strongly dependent on whether the magnetizations of the two FM layers are parallel or antiparallel [7, 8]. By replacing the middle nonmagnetic material with an insulating tunneling barrier (TB), a magnetic tunnel junction (MTJ) is formed, as shown in Figure 2.1 [9, 10]. The working principle of TMR and GMR devices are similar, as the spin-dependent DOS of each FM determines the probability of electron transport and the resulting resistance of the device, whereas the electron transfer occurs

either by a diffusive transport in the nonmagnetic material or by spin-conserving tunneling through a TB. Magnetic tunnel junctions are characterized by the tunnel magnetoresistance (TMR) ratio [32], expressed as

$$TMR = \frac{R_{AP} - R_P}{R_P} = \frac{2P_1P_2}{1 - P_1P_2}, \quad (2.3)$$

where  $R_P$  and  $R_{AP}$  are the MTJ resistance in the parallel and antiparallel state, and  $P_1$  and  $P_2$  denote spin polarization of electrons at the Fermi level for the two magnetic layers. As the achieved GMR and TMR ratios of  $\sim 50\%$  and  $\sim 600\%$  [33] were much higher than previously seen results with the anisotropic magnetoresistance (AMR  $\sim 1\%$ ), they could be rapidly industrialized and implemented in the read heads in magnetic memory devices, which allowed to greatly increase the information storage density in hard disc drives (HDDs).

## 2.3 Spin-orbit coupling and spin relaxation

In nonmagnetic materials, the DOS for spin-up and spin-down electrons is the same, and no spontaneous spin polarization exists in equilibrium. By electrical injection of spin-polarized current from a FM, a nonequilibrium spin density is formed at the interface. However, this imbalance between spin populations can have only a limited lifetime as it tends to relax back to the unpolarized equilibrium state. This spin relaxation is governed mainly by the spin-orbit coupling via several common mechanisms.

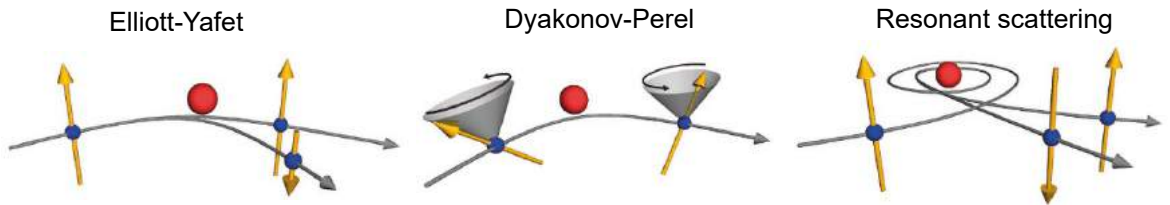


**Figure 2.2:** Spin relaxation mechanisms relevant for graphene. Illustrations of the Elliott-Yafet, D'yakonov-Perel', and resonant scattering by local magnetic moments. The blue dots are electrons/holes, yellow arrows represent their spin, red circles are the scattering centres, and grey cones represent the spin precession. Adapted from [34].

Spin-orbit coupling (SOC) is a central spin interaction, denoting the coupling between an electron's spin and its orbital angular momentum. The Elliott-Yafet (EY) and D'yakonov-Perel' (DP) mechanisms relate SOC and spin relaxation (Figure 2.2). The EY mechanism considers the spin relaxation induced by the mixture of spin-up and spin-down states during ordinary momentum scattering events by phonons or impurities in the presence of spin-orbit coupling induced

by lattice ions [2]. Since the spin flip in the EY mechanism happens during the momentum scattering, this process results in the spin lifetime being directly proportional to the momentum relaxation time  $\tau_s \sim \tau_p$ . The DP mechanism is present in systems lacking inversion symmetry, which introduces the spin splitting of the electron states. It can be described by an effective intrinsic momentum-dependent magnetic field that derives from the SOC in the band structure and induces spin precession and relaxation. Such spin precession about fluctuating magnetic fields changing as the scattering alters carrier momentum leads to slower spin dephasing for faster momentum relaxation  $\tau_s \sim \tau_p^{-1}$ .

Besides SOC, spin relaxation can be induced by the hyperfine interaction or resonant scattering. Hyperfine interaction describes the coupling between magnetic moments of electrons and nuclei, however, it is not relevant for systems with zero nuclear momentum, which is the case for the most common carbon isotope  $^{12}\text{C}$ . Alternatively, spin relaxation can occur due to the resonant spin-flip scattering on magnetic impurities (vacancies or adatoms) [35]. In this scenario, the carriers at resonant energies can spend considerable time in the exchange field created by the impurity, which induces spin relaxation by precession.

The strength of SOC and the prominence of spin relaxation mechanisms determine the capability of nonmagnetic materials to preserve and transport spin polarization. Low SOC is beneficial to suppress spin scattering and achieve a large spin lifetime  $\tau_s$  and spin diffusion coefficient  $D_s$ , which together define the spin diffusion length  $\lambda_s = \sqrt{D_s \tau_s}$ , the characteristic distance over which spin polarization can be transported. A combination of the low intrinsic SOC and the absence of hyperfine interactions make graphene one of the most interesting materials for applications in spintronics, as it exhibits the largest known  $\tau_s$  and  $\lambda_s$ , and can be combined in van der Waals heterostructures with other materials, including high-SOC layers.

## 2.4 Graphene

Graphene is a monolayer of carbon atoms arranged in a hexagonal lattice (Figure 2.3a). It is a prototypical two-dimensional material exhibiting semimetallic behavior with linear energy dispersion at low energies, forming Dirac cones at K and K' points in the Brillouin zone (Figure 2.3b). Because of this, carriers in graphene are described as relativistic massless Dirac fermions with high mobility, making this material interesting for electronics. The field effect allows to tune the carrier concentration in graphene across its Dirac point using the gate voltage, which provides a convenient way to probe both the hole and electron conduction in one device (Figure 2.3c). Although the lack of the band gap does not allow to completely switch OFF the electron current, which limits the use of graphene in field-effect transistors, the ability to control the carrier density and type are useful for studies of the emerging effects in graphene-based heterostructures.

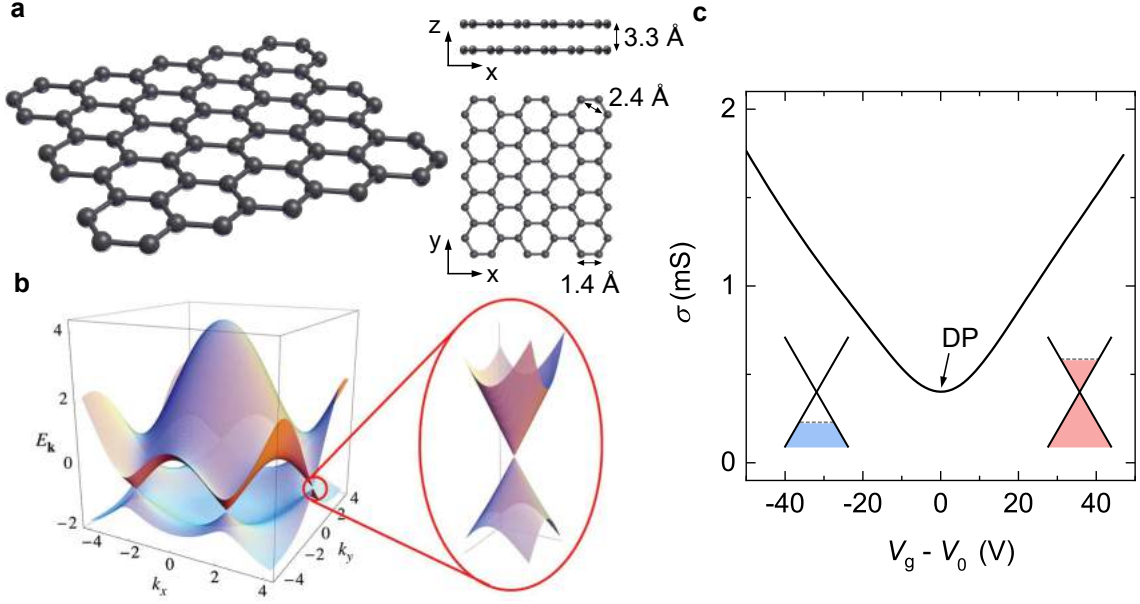


**Figure 2.3:** Properties of graphene. **a**, Crystal lattice of a monolayer graphene consists of carbon atoms arranged in a hexagonal structure. Multiple such layers held together by van der Waals forces form graphite. **b**, Conduction and valence bands of the monolayer graphene touch in the corners of a Brillouin zone, forming Dirac cones at the K and K' points. **c**, Conductivity of graphene as a function of the gate voltage. Adapted from [18].

The conductivity of graphene based on the Drude's equation can be expressed as [36]

$$\sigma = ne\mu, \quad (2.4)$$

where  $n$  is the carrier concentration,  $e$  is the electron charge, and  $\mu$  is the carrier mobility. Note that in real devices the conductivity does not vanish at the Dirac point, but rather reduces to a minimum value, which can be denoted as  $\sigma_0$ . This residual conductivity arises due to the charged impurities and the formation of electron-hole puddles at the Dirac point, which limits the minimum achievable carrier density to  $n^* \sim 5 \times 10^{11} \text{ cm}^{-2}$  [37, 38]. Using a parallel plate capacitor model, the additional carrier density induced in graphene by the gate voltage can be expressed as

$$n = \frac{\varepsilon\varepsilon_0}{te} (V - V_0), \quad (2.5)$$

where  $\varepsilon$  is the relative dielectric constant of the gate insulator ( $\varepsilon_{\text{SiO}_2}=3.9$ ),  $\varepsilon_0 = 8.85 \times 10^{-12} \text{ F m}^{-1}$  is the vacuum dielectric constant,  $t$  is the dielectric thickness,  $e$  is electron charge, and  $V_0$  is the effective gate voltage offset due to initial doping. Combining equations 2.4 and 2.5, it is possible to extract the field-effect mobility of graphene. In typical CVD graphene samples, it can take values  $\mu = 1000 - 10\,000 \text{ cm}^2 \text{ V}^{-1} \text{ s}^{-1}$ , and even larger for encapsulated and/or exfoliated graphene. The change in carrier density by the gate voltage is directly related to the shift

of the graphene Fermi level, which can be expressed as [39]

$$n = \left( \frac{E_F}{\hbar v_F} \right)^2 / \pi, \quad (2.6)$$

where  $v_F = 10^6$  m/s is the Fermi velocity in graphene, and  $\hbar = 6.58 \times 10^{-16}$  eV s is the reduced Planck's constant. Using the Einstein relation  $\sigma = e^2 \nu D_c$ , where  $\nu$  is the DOS of graphene, the diffusion coefficient of charge carriers can be obtained via

$$D_c = \frac{\sigma \hbar v_F}{4e^2 \sqrt{\pi n}}, \quad (2.7)$$

which is also related to the mean free path  $\ell_{\text{mfp}}$  and momentum scattering time  $\tau_p$  via  $D_c = v_F \ell_{\text{mfp}} / 2$  and  $\ell_{\text{mfp}} = v_F \tau_p$  [40].

## 2.5 Nonlocal spin transport

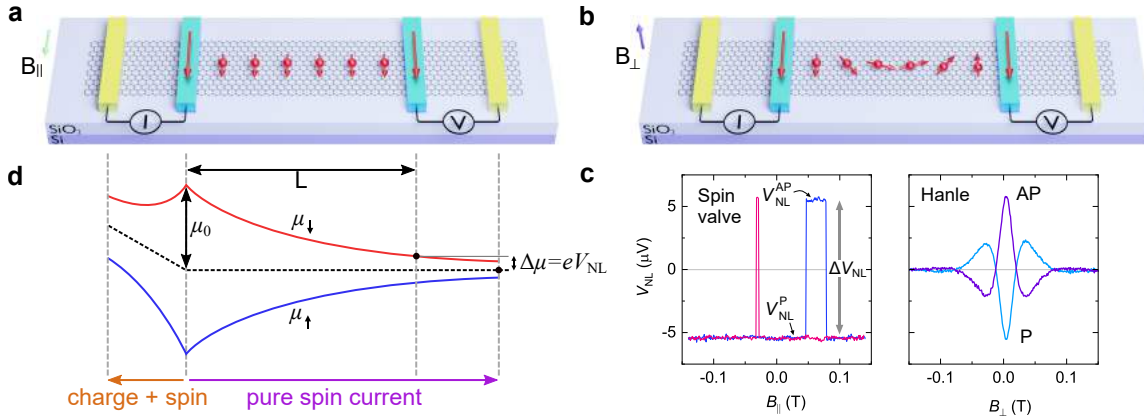


**Figure 2.4:** Nonlocal spin transport measurements in graphene. **a**, A schematic of the spin valve measurement configuration. **b**, A schematic of the Hanle spin precession measurement with the out-of-plane magnetic field. **c**, Representative measurements obtained in the spin valve and Hanle spin precession experiments. **d**, A sketch of the electrochemical potentials for spin-up and spin-down carriers.

Spin transport in graphene is commonly studied in a nonlocal measurement geometry. Figures 2.4a,b show a typical device geometry with the measurement configurations utilized for the spin valve (SV) and Hanle spin precession experiments. For these measurements, the electron current is applied between a FM contact and graphene, which creates spin accumulation  $n_s$  below the injector with spins parallel to its magnetization. This nonequilibrium spin density then diffuses in the channel as a spin current and can be detected as the nonlocal spin voltage by another FM contact in reference to a nonmagnetic electrode which is insensitive to the spin polarization. To measure a spin valve, the external magnetic field



is applied in plane along the easy magnetization switching direction of FM electrodes, which results in sudden changes in the detected voltage when the magnetic field flips the magnetization of either injector or detector. A typical SV signal is demonstrated in the left panel of Figure 2.4c. Such measurements can be explained by considering the profile of spin chemical potential  $\mu \propto n_s$  in the channel (Figure 2.4d), which can be used to express the nonlocal voltage at the detector as [41]

$$\Delta V_{NL} = V_{NL}^{AP} - V_{NL}^P = \frac{2\Delta\mu}{e} = \frac{P_d e D_s}{\sigma} n_s(L) = \frac{P_i P_d I \lambda_s}{\sigma W} e^{-L/\lambda_s}, \quad (2.8)$$

where  $V_{NL}^P$  and  $V_{NL}^{AP}$  are the nonlocal voltages for the parallel and antiparallel alignment of the FM magnetizations,  $P_i$  and  $P_d$  are spin injection and detection efficiency,  $D_s$  is the spin diffusion coefficient,  $I$  is the injection bias current,  $L$  and  $W$  are the channel length and width, and  $\lambda_s = \sqrt{D_s \tau_s}$  is the spin diffusion length.

Whereas the in-plane magnetic field  $B_{\parallel}$  in a spin valve experiment is used only to control the magnetization state of FM contacts, the application of a perpendicular field  $B_{\perp}$  can be utilized to directly control the dephasing of spins diffusing in the channel. The dynamics of the spin density in the presence of an arbitrary magnetic field is described by the Bloch-Torrey spin drift-diffusion equation [41–43]

$$-D_s \nabla^2 \mathbf{n}_s + \frac{\partial \mathbf{n}_s}{\partial t} = -\Omega \mathbf{n}_s + \omega_L \mathbf{n}_s \times \hat{\mathbf{e}}_B, \quad (2.9)$$

where  $\Omega$  is the matrix representing the spin relaxation rates for each direction (for an isotropic system,  $\Omega = 1/\tau_s \cdot \mathbb{1}$ ),  $\hat{\mathbf{e}}_B$  is a unit vector pointing parallel to the magnetic field, and  $\omega_L$  is the Larmor frequency of the spin precession

$$\omega_L = \frac{g \mu_B B_{\perp}}{\hbar}, \quad (2.10)$$

where  $g$  is the effective Landé factor ( $\sim 2$ ), and  $\mu_B$  is Bohr magneton. Considering the out-of-plane field, eq. 2.9 can be solved to obtain the expression for a Hanle spin precession curve

$$\Delta V_{NL}(B) = \text{Re} \left( \frac{P_i P_d I \widetilde{\lambda}_s}{\sigma W} e^{-L/\widetilde{\lambda}_s} \right), \quad (2.11)$$

where  $\widetilde{\lambda}_s$  is a complex renormalization of the spin relaxation length due to the effect of the magnetic field

$$\widetilde{\lambda}_s = \frac{\lambda_s}{\sqrt{1 + i\omega_L \tau_s}}. \quad (2.12)$$

Equation 2.11 can be used to fit the experimental Hanle spin precession data (right panel of Figure 2.4c), and allows to extract the spin transport parameters of

the system. To fit individual Hanle measurements without the subtraction of P and AP curves, an additional factor of 2 should be added in the denominator of eq. 2.11 since the Hanle amplitude is normally half that of a spin valve. In typical CVD graphene samples, we obtain spin relaxation time  $\tau_s \sim 200$  ps, spin diffusion coefficient  $D_s \sim 0.04 \text{ m}^2 \text{ s}^{-1}$ , and spin diffusion length  $\lambda_s \sim 3 \mu\text{m}$ .

## 2.6 Topological insulators

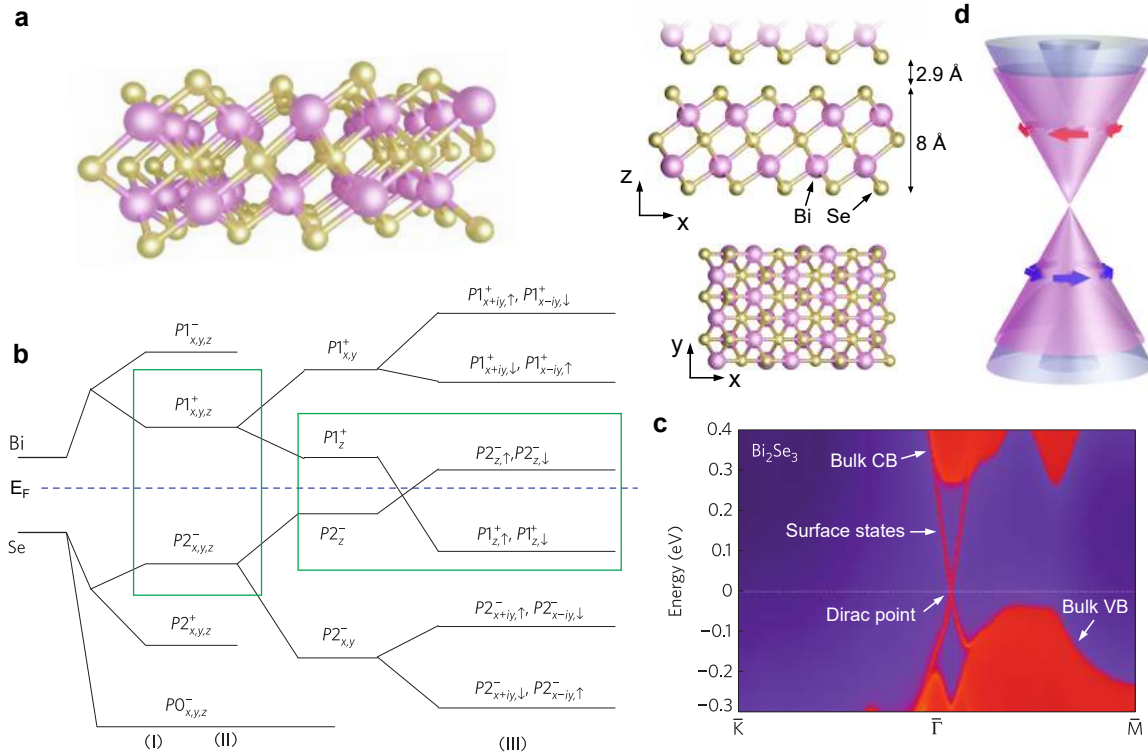


**Figure 2.5:** Properties of topological insulators. **a**, Crystal lattice of a prototypical TI Bi<sub>2</sub>Se<sub>3</sub>. **b**, A schematic of the evolution of atomic orbitals of Bi and Se into the conduction and valence bands of Bi<sub>2</sub>Se<sub>3</sub> at  $\Gamma$  point. Stages (I), (II), and (III) represent the effect of chemical bonding, crystal-field splitting, and SOC, respectively. **c**, The calculated band structure of Bi<sub>2</sub>Se<sub>3</sub> with conducting surface states and gapped bulk. The warmer color represents the higher local density of states. **d**, A schematic of the band structure of a TI with the Dirac cone on the surface. The arrows indicate the orientation of spin for a given momentum, which represents spin-momentum locking. Adapted from [44].

Topological insulators represent a novel state of matter, having a band gap in the bulk, but exhibiting conducting gapless states on the surface (or the edge in the 2D case), which are protected by time reversal symmetry. In fact, the first predicted TI material was graphene, as proposed by Kane and Mele in their seminal theoretical works [45, 46]. However, due to the low intrinsic SOC in

graphene, a topological state was not experimentally realized in this material. Instead, stable topological insulator phases were identified in three-dimensional layered crystals such as  $\text{Bi}_2\text{Se}_3$ ,  $\text{Bi}_2\text{Te}_3$ ,  $\text{Sb}_2\text{Te}_3$ , which have a relatively large band gap of  $\sim 0.3\text{ eV}$ , making their topological properties detectable even at room temperature.

Figure 2.5a shows a schematic of one quasi-monolayer of a  $\text{Bi}_2\text{Se}_3$  crystal, which is a quintuple layer formed by the three layers of Se and two layers of Bi covalently bonded to each other. A bulk of the material is comprised of multiple such quintuple layers which are bonded to each other by weak van der Waals forces. These materials become topologically nontrivial due to their strong intrinsic spin-orbit coupling, which induces the band inversion. This phenomenon is schematically shown in Figure 2.5b, where the evolution of the energy levels, originating from Bi and Se atoms, is shown at  $\Gamma$  point with the effects of chemical bonding, crystal field splitting, and SOC [44]. The states near the Fermi energy are formed from the 6p orbitals of Bi and 4p orbitals of Se, which become split and shifted in energy due to their interactions in a crystal. The SOC in these crystals is strong enough to reverse the order of the two energy levels closest to the Fermi level, which leads to the topological insulator state. This inverted structure necessitates the formation of a gapless surface state at the boundary between the topological insulator and any topologically trivial material, including the vacuum. Figure 2.5c shows an *ab initio* calculation of the band structure of  $\text{Bi}_2\text{Se}_3$ , where clear linearly dispersing states exist on the surface of the material, whereas the bulk states are gapped. Furthermore, the strong SOC aligns the spins in the surface states perpendicularly to their momentum, which results in a helical spin texture decorating the Dirac cone (Figure 2.5d). This spin texture leads to the formation of spin polarization in the surface states, which is referred to as the spin-momentum locking phenomenon. Alternatively, the creation of spin polarization by passing a current through topological surface states is described as the Edelstein effect [47]. This charge-spin conversion capability makes topological insulators interesting for applications in spintronics as spin generators/detectors, and can also be used in the emerging magnetic memory technologies based on spin-orbit torque [48, 49].



## 3 State of the art

This chapter aims to provide a broad perspective and context for the results obtained in this thesis by offering a comprehensive overview of the state-of-the-art in the field of spintronics with 2D materials. The developments in graphene spin transport are presented, and the prospects of its utilization in spin logic devices are discussed. The studies of spin polarization in topological insulators are summarized. Finally, a detailed review of the proximity-induced spin-orbit effects in graphene in heterostructures with transition metal dichalcogenides (TMDs) and topological insulators (TIs) is presented, covering the spin transport, spin lifetime anisotropy, and spin-charge conversion phenomena.

### 3.1 Graphene spintronics

Since its first isolation in 2004 by Andre Geim and Konstantin Novoselov, graphene has ignited a broad new research field of two-dimensional materials [16]. Due to the remarkable honeycomb 2D structure, graphene was shown to display many unique properties and exciting phenomena. Theoretical and experimental investigations have revealed the linear energy dispersion, ambipolar field effect, quantum Hall effect at room temperature, high carrier mobility, large thermal conductivity, great mechanical strength, high optical absorptivity, etc. [50]. In addition, graphene became one of the most important materials in spintronics as it was found to possess the longest spin lifetime among all investigated materials at room temperature, which is attributed to its minuscule intrinsic spin-orbit coupling. These properties suggest that graphene can be a perfect spin interconnect material suitable for long-distance spin transport, which motivated the scientific community to explore its spin-related functionality.

#### 3.1.1 Spin transport in graphene

The first study of spintronic properties of graphene has been performed in 2007 with exfoliated single- and few-layer samples contacted by spin-sensitive cobalt electrodes through a tunneling barrier [19]. Figure 3.1a shows a scanning electron microscope (SEM) picture of the device, consisting of a single layer of exfoliated graphene contacted by Co electrodes. Figure 3.1b shows the obtained non-local Hanle spin precession measurement and the extracted spin parameters. These pioneering experiments have confirmed good spin transport capabilities of graphene,

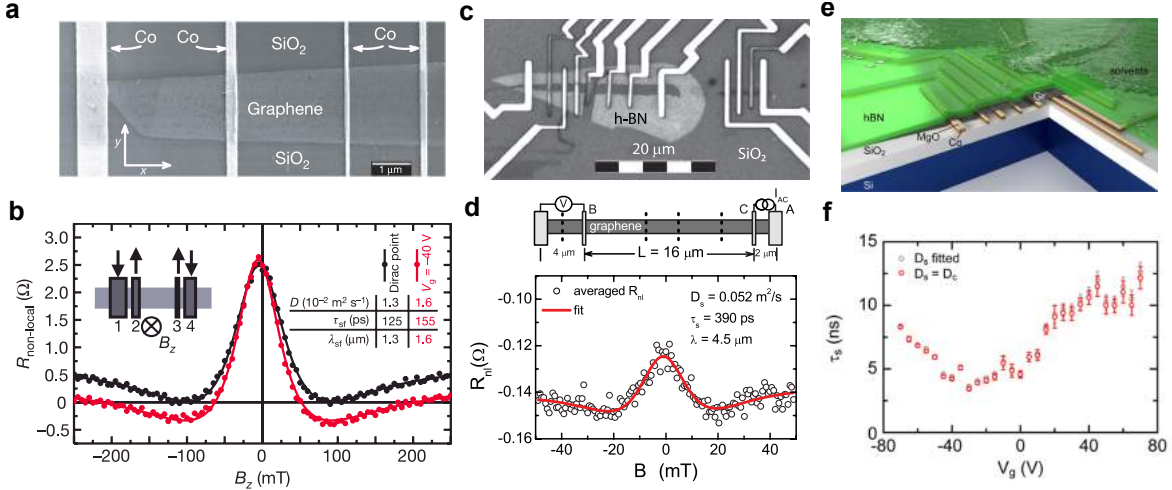


**Figure 3.1:** Spin transport experiments in exfoliated graphene. **a**, An SEM picture of a spintronic device in single-layer graphene contacted by tunnel FM contacts. **b**, A non-local Hanle spin precession measurement in graphene. **c**, An optical micrograph of the graphene nonlocal spin valve device on hBN substrate. **d**, A Hanle spin precession curve obtained in graphene on hBN. **e**, A schematic of the exfoliated graphene device protected by hBN on top and contacted with FM electrodes from the bottom. **f**, The extracted spin lifetime in hBN-protected devices. Adapted from [19, 20, 51].

however, the obtained spin lifetime values  $\tau_s \sim 100$  ps were several orders of magnitude lower than the theoretical predictions of  $\tau_s \sim \mu\text{s}$  [52]. To explain this discrepancy, further investigations addressed contact-induced relaxation, substrate effects, fabrication-induced impurities, structural defects, strain, and others. In particular, it was realized that to increase spin lifetime and spin diffusion length it is crucial to protect graphene from fabrication-induced defects and to use an optimal substrate. In this regard, the incorporation of hexagonal boron nitride (hBN) was shown to greatly improve the device quality (Figure 3.1c). hBN is an atomically flat 2D insulator with a similar lattice structure to graphene, which makes these materials highly compatible. Graphene placed on top of hBN benefits from reduced substrate roughness compared to SiO<sub>2</sub>, which improved its mobility and allowed to achieve greater spin transport parameters (Figure 3.1d) [51]. In addition, the van der Waals interactions between these layers were utilized to develop a dry transfer technique, which allows to transfer graphene flakes onto predefined substrates [53, 54]. By using this technique to transfer the exfoliated graphene flakes onto prepatterned magnetic tunnel electrodes, the graphene is never exposed to the solvents and resists, and the hBN layer remains in the final device to protect it from ambient contaminants (Figure 3.1e). These improvements led to the observation of the highest reported value of spin lifetime  $\tau_s = 12.6$  ns and spin diffusion length  $\lambda_s = 30.5 \mu\text{m}$  in such graphene devices (Figure 3.1f) [20].

Further development of graphene spintronics towards industrial applications prompts the utilization of scalable graphene growth techniques. For this pur-

pose, the epitaxial graphene on silicon carbide (SiC) and chemical vapor deposited (CVD) graphene on metal films were extensively studied. In the former, good spin transport performance was observed [55–57], however, the effects of the buffer layer and the special substrate hamper its further development. Alternatively, a relatively cheap method for producing wafer-scale graphene is CVD growth on metallic substrates. Although exfoliated and epitaxial samples generally exhibit larger carrier mobility values, the optimized CVD parameters can yield high-quality graphene with mobilities comparable to those seen in exfoliated devices. In addition, for practical applications, the CVD graphene has to be transferred from the metallic film onto an insulating substrate. This is usually done via the wet transfer process, in which the metallic foil is etched away and the graphene is deposited onto the substrate of interest while being submerged in a solvent. Optimizing this process is critical to avoid damage or unwanted doping in graphene. Alternatively, a dry transfer technique by an hBN stamp was shown to be compatible also with CVD graphene, allowing to lift the graphene off the metallic growth substrate and transfer it onto another substrate of interest [58]. This technique yields ultrahigh-mobility CVD graphene, but its scalability is currently limited by the need for wafer-scale hBN stamps, which requires further development of hBN CVD growth techniques.

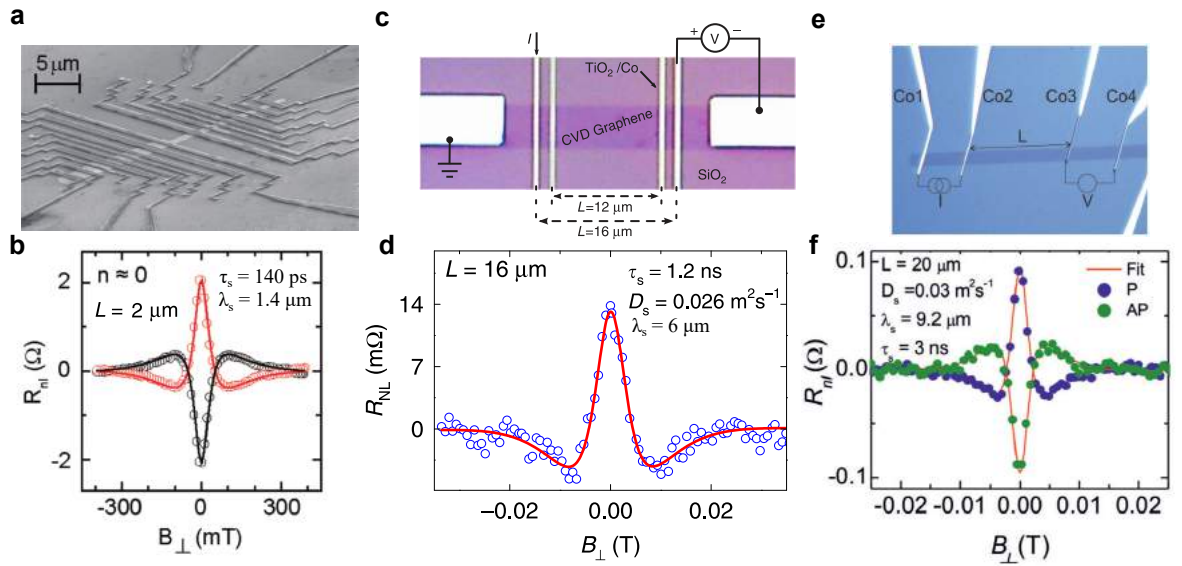


**Figure 3.2:** Spin transport experiments in CVD graphene. **a**, An SEM picture of a single-layer CVD graphene sample with multiple nonlocal spin valve devices. **b** Initial non-local Hanle spin precession measurements obtained in CVD graphene with channel length  $L = 2 \mu\text{m}$ . **c**, A CVD graphene spin transport device with  $L = 16 \mu\text{m}$ . **d**, Hanle spin precession curve obtained in a long channel. **e**, An optical image of a Pt-CVD grown graphene non-local spin transport device. **f**, A Hanle measurement performed in CVD graphene with the channel length  $L = 20 \mu\text{m}$ . Adapted from [21, 59, 60].

Initial spin transport studies in CVD graphene have shown that the extracted  $\tau_s$  and  $\lambda_s$  have comparable values to those observed in (non-encapsulated) exfoliated graphene samples (Figures 3.2a,b) [59]. In addition, whereas the length of the exfoliated channel is limited by the size of the graphene flake, CVD samples do not have such a limitation, which allowed fabricating and studying spin transport in long channels. These developments allowed to achieve spin transport over distances as large as  $16\text{ }\mu\text{m}$  in Cu-grown graphene (Figures 3.2c,d) [60], and up to  $30\text{ }\mu\text{m}$  in Pt-grown graphene (Figures 3.2e,f) [21]. Spin communication over such large distances is beneficial for the use of CVD graphene as a spin interconnect in scalable spin-logic applications.

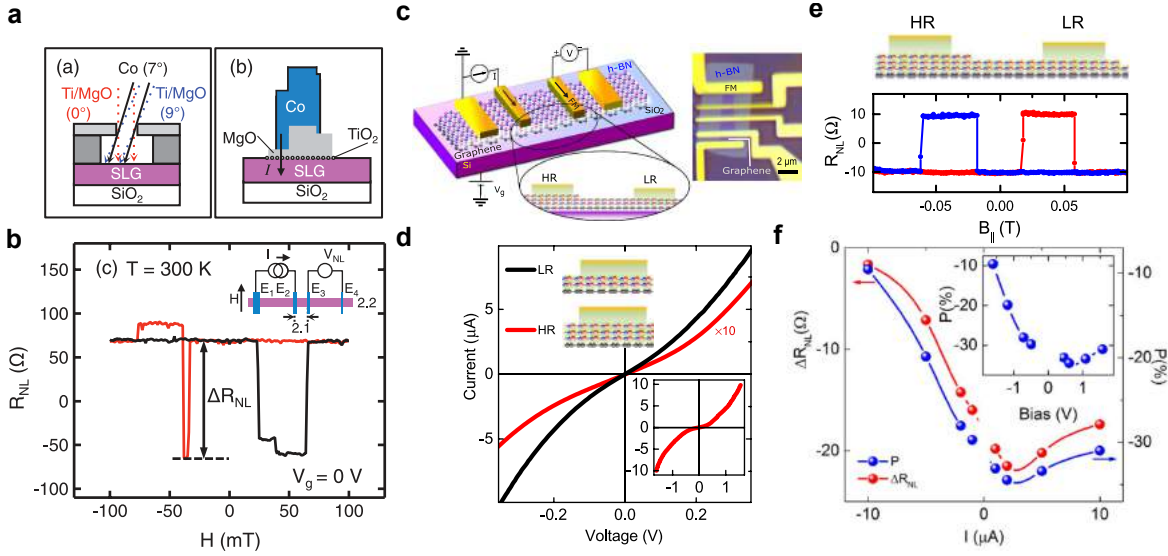


**Figure 3.3:** Tunnel barriers for efficient spin injection/detection. **a**, Schematics of the angle evaporation geometry and the resulting MgO tunnel barrier structure. **b**, A large nonlocal spin valve signal obtained with TiO<sub>2</sub>-seeded MgO tunnel barrier between Co and exfoliated graphene with channel length  $L = 2.1\text{ }\mu\text{m}$ . **c**, A schematic of the graphene-hBN heterostructure where the 2D insulator serves as a tunnel barrier as well as a protective top layer. Various thickness of hBN along the flake results in the formation of high and low resistance contacts (HR and LR). **d**, Three-terminal current-voltage characteristics of HR and LR hBN contacts show a nonlinearity, indicating the tunneling behavior. **e**, A large spin valve signal obtained with the hBN tunnel barrier. **f**, The extracted bias-dependent spin polarization of the tunnel FM contacts with CVD hBN tunnel barrier. Adapted from [61, 62].

The magnitude of the spin signal depends on the spin polarization at the interface between graphene and ferromagnetic contacts, which defines the amount of spins that can be injected. Because of the much larger conductivity of ferromagnetic metals compared to graphene, in ohmic contacts the injected spins can back-scatter into the FM and reduce the spin accumulation and the effective spin polarization [63]. To suppress such backscattering, a tunnel barrier is often



inserted between a FM and graphene. Over the years, such tunnel barriers were mainly fabricated from various oxide materials, such as MgO, TiO<sub>2</sub>, Al<sub>2</sub>O<sub>3</sub>, and SrO. Such tunnel barriers increase the FM contact interface resistance  $R_I$ , and the conductivity mismatch is considered suppressed if  $R_I$  exceeds the spin resistance of graphene  $R_{\text{Gr}}^s = R_{\text{sq}}W/\lambda_s$ . Figure 3.3a shows a representative structure of the FM contact with MgO tunnel barrier. A careful engineering of the interface geometry and barrier uniformity using a seeding layer of TiO<sub>2</sub> allowed to achieve spin polarization as high as 30% and a significant spin signal magnitude (Figure 3.3b) [61]. However, when growing thin ( $\sim$  few Å) metallic films, for example, of titanium, the atoms tend to accumulate in clusters and form islands, which reduce the quality of the resulting TiO<sub>2</sub> tunneling barrier due to the presence of pinholes after the oxidation. Interestingly, it was shown that hBN, besides serving as an encapsulation material, can be also utilized as an efficient tunnel barrier (Figure 3.3c). The absence of pinholes and low roughness in these devices allowed to achieve high-quality tunnel IV characteristics (Figure 3.3d) and large magnitudes of the spin signal with an evidence for the spin filtering in such structures (Figure 3.3e) [62]. These developments led to large spin polarization values of  $P \sim 30 - 65\%$  in exfoliated graphene-CVD hBN (Figure 3.3f) and the differential spin detection efficiency as large as 130% in fully encapsulated all-exfoliated devices [64], surpassing the values seen in common oxide barriers.

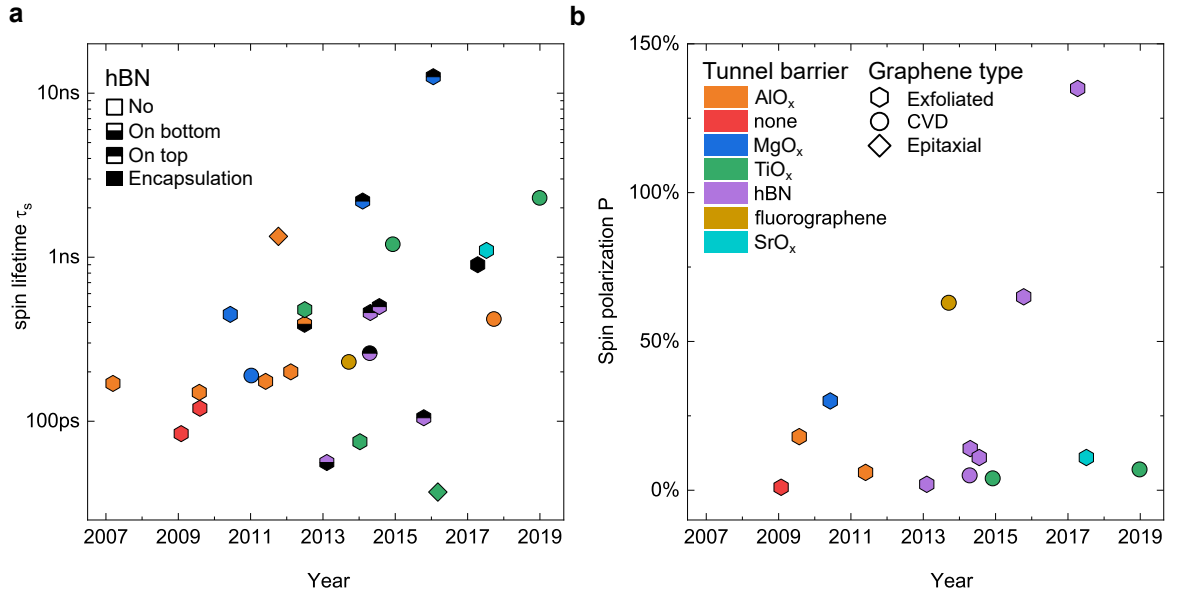


**Figure 3.4:** Developments in spin transport characteristics over time. **a**, Spin lifetime in graphene extracted from spin transport experiments with various tunnel barriers and device structures. **b**, Spin polarization obtained from spin transport experiments with various tunnel barriers in graphene. The data is collected from [19–21, 40, 51, 55, 57, 59–62, 64–77].

The main pursued avenues to improve spin injection and transport capabilities

in both exfoliated and CVD graphene concerned the quality of the channel, which defines spin lifetime, and the spin polarization at the interface between graphene and ferromagnetic contacts, which defines the amount of spins that can be injected. Figure 3.4a gives an overview of the spin lifetimes achieved in graphene devices over the years and shows that the modern fabrication techniques can yield long lifetimes in both the exfoliated and CVD graphene, with the largest values seen in graphene protected by hBN. Figure 3.4b presents the achieved effective spin polarization values of the interface between FM contacts and graphene over the years. This data shows that the use of hBN as a tunnel barrier and an encapsulation material can greatly increase both the spin lifetime and spin polarization, marking a promising direction for the design of future spintronic devices and urging to develop the techniques for wafer-scale growth and transfer of hBN.

### 3.1.2 Graphene for spin logic

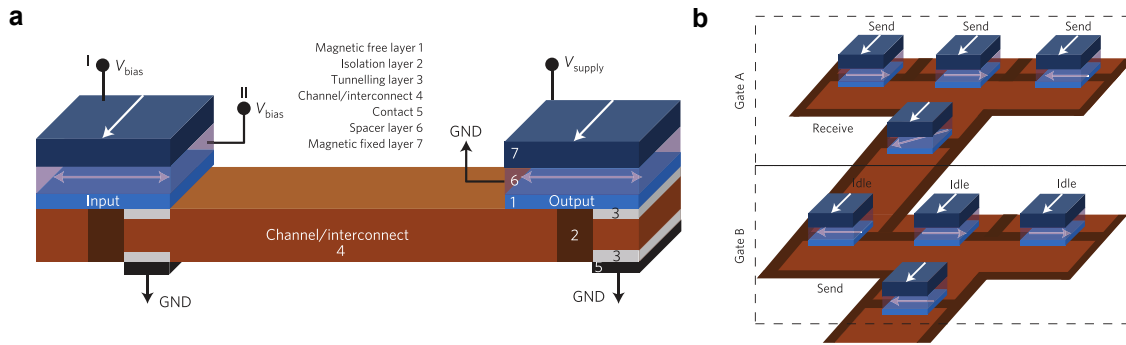


**Figure 3.5:** An all-spin logic device. **a**, A schematic of the device with magnetic spin injectors/detectors connected via a spin channel. The input can produce spin current that determines the output state by spin transfer torque assisted by the MTJ structure that drives the output magnet into a high-energy neutral state prior to the logic operation. The tunnel barriers ensure an optimal spin injection efficiency only from one side of the ferromagnets, eliminating unwanted feedback. **b**, Example of cascading all-spin majority logic gates. Such gate can be used as an AND or OR gate by fixing one of the inputs, and the logic inversion functionality can be achieved by using positive and negative bias voltages. Adapted from [78].

Several proposals to realize spin logic devices have been put forward [78–84]. Figure 3.5a shows a proposed all-spin switch [78], where the information is encoded in the magnetization states of nanomagnets, which are connected by spin-coherent transport channels. The device design relies on the possibility to switch the magnetization state of the output magnet via spin torque exerted onto it by the spin current that was injected at the input and propagated through the channel. Such a device was shown to satisfy the five essential criteria for logic applications namely concatenability, nonlinearity, feedback elimination, gain, and the realization of a complete set of Boolean logic gates. Concatenability is achieved through

representing both the input and the output in the same form of magnetization direction. Nonlinearity is ensured through the magnetic anisotropy, which provides only two stable states for the input/output magnetization. The back-influence of the output magnet onto the input is eliminated by asymmetric coupling of the magnets to the channel, with a tunnel barrier on the injecting side and an Ohmic contact on the detecting side, which allows to remove the unwanted feedback. To achieve gain, the device architecture suggests to use the spin channel only for transferring the information, whereas the energy for output switching is provided by a separate voltage source. It is known that NAND gates are sufficient to realize any logical operation, i.e. they form a universal gate set [85]. The proposed ASL devices can realize the NAND operation in a majority gate geometry with one output fixed as "1" and others inverted through the application of a negative bias (positive/negative input bias results in a COPY/NOT of the input). However, instead of such brute-force approach, developing optimized device designs can allow to use the analog nature of these ASL devices to produce functional gates such as a full-adder in a more compact way compared to their charge-based counterparts.

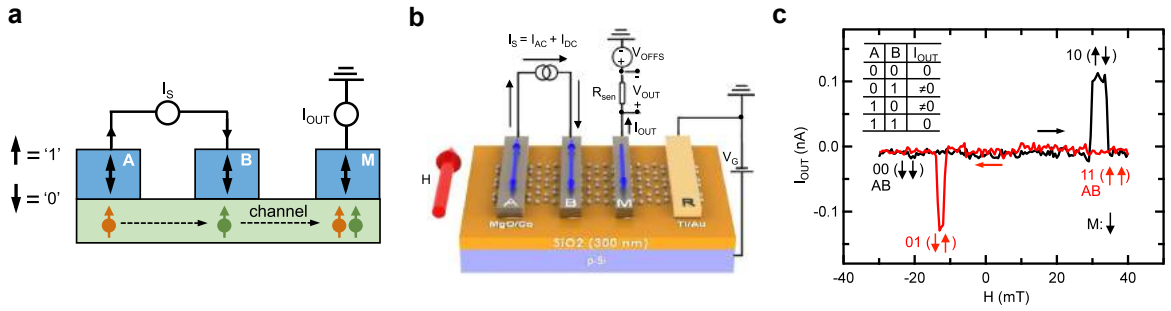


**Figure 3.6:** A spin XOR gate in graphene. **a**, A diagram of the proposed XOR device with input states decoded in the magnetization of the FMs A and B, and the output state is the current defined by the tunneling magnetoresistance. **b**, An illustration of the experimental device structure and the measurement setup. The ferromagnetic tunnel electrodes are used to inject spin polarization in the channel, which diffuses towards the detector and determines its magnetoresistance. The detected nonlocal spin voltage can be converted into current and amplified to serve as the input of concatenated gates. **c**, The output current signal as a function of the magnetic field, showing the different states corresponding to the combinations of the up or down magnetization states of injectors A and B, whereas the output FM magnetization is kept constant. Adapted from [86].

Because the graphene can preserve spin polarization for a long time and transport spin currents over large distances, it is considered an attractive material to be utilized as a spin channel in the proposed spin logic concepts. However, so far only a few experimental works have been performed towards the realization of such spin logic devices [86, 87]. A spin "exclusive or" (XOR) logic operation was realized using ferromagnetic electrodes connected by graphene that serves as

a spin channel (Figures 3.6a,b). The magnetization directions of the first two FMs represent the logic inputs, and the injected spin density from these inputs propagates through the channel and determines the current through the output electrode, representing the logic output. Figure 3.6c shows the output voltage for all four combinations of the input states which are controlled through the application of external magnetic field that switches the magnetization of the input FM electrodes, realizing the states corresponding to the XOR truth table. However, several issues regarding the device performance need to be addressed before practical applications. To achieve cascading of these gates, the output current has to be amplified to drive subsequent inputs, which requires additional circuitry and transitions between spin and charge domains [88]. To achieve all-spin operation, it is required to represent both the inputs and the output in the spin domain, i.e. the result of the logic operation should be able to switch the magnetization of the output magnet. This can be achieved through the spin transfer torque, however, such functionality in nonlocal graphene devices so far was demonstrated only for very short channels ( $L \leq 400$  nm) [89, 90]. Alternatively, more complicated switching mechanisms may be employed based on the spin Hall effect or spin-orbit torque.

## 3.2 Topological insulators

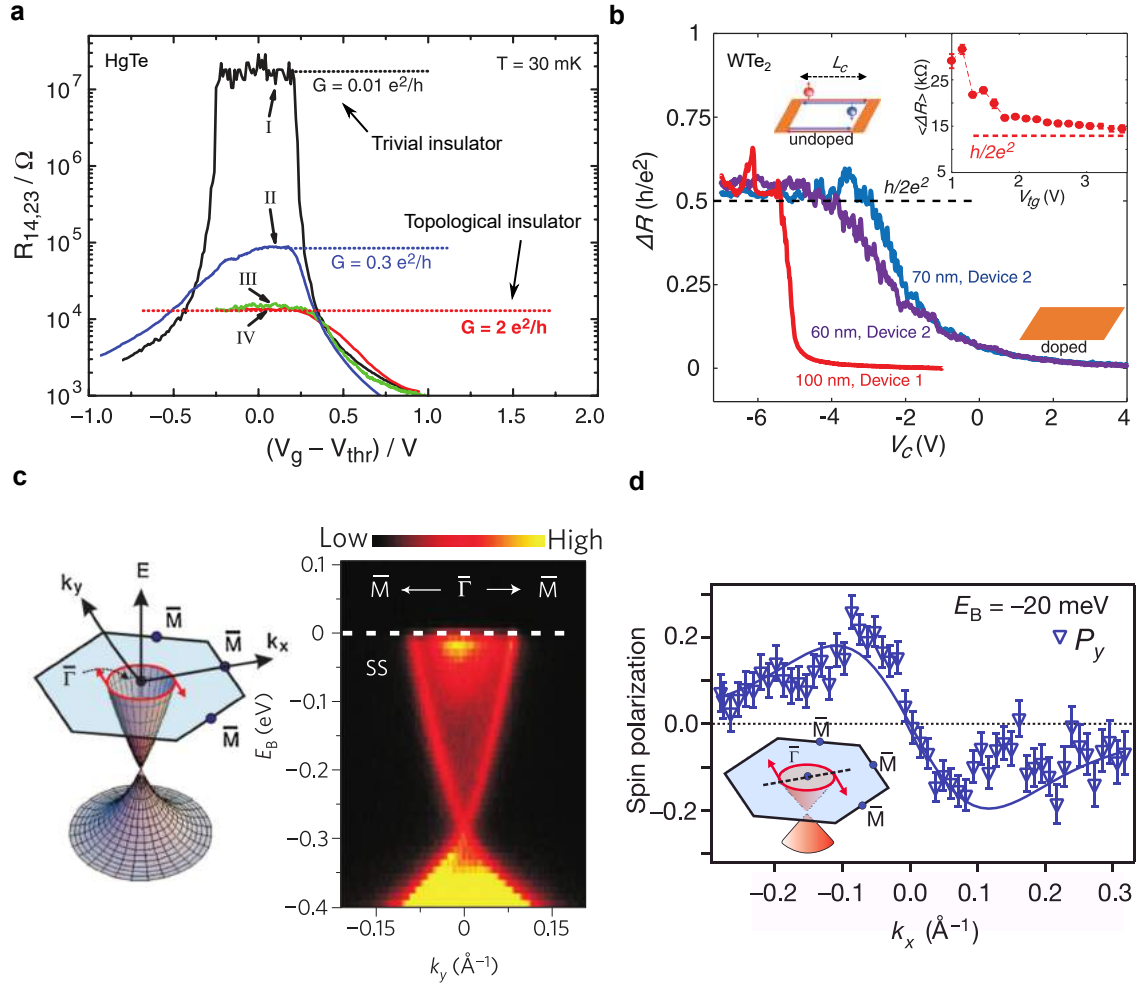


**Figure 3.7:** Studies of topological insulators. **a**, First 2D topological insulator state detected in the longitudinal resistance of HgTe quantum wells in the inverted band ordering regime at  $B = 0$ . **b**, Quantum spin Hall effect observed in monolayer WTe<sub>2</sub> as a resistance plateau due to the conduction along the edges. **c**, Angle resolved photoemission spectroscopy (ARPES) of a 3D TI Bi<sub>2</sub>Se<sub>3</sub> reveals the presence of a Dirac cone in its surface electronic band dispersion. **d**, Spin-resolved ARPES of Bi<sub>2</sub>Te<sub>3</sub> along the  $\Gamma - M$  direction shows the presence of the spin polarization perpendicular to the momentum. Adapted from [91–95].

With the first experimental realization of the 2D topological insulator phase in HgTe quantum wells [91], topological properties of materials have become an important concept for novel device designs. In this material system, the high SOC of HgTe leads to the band inversion when the layer thickness exceeds a critical value  $d_c \simeq 6.5$  nm. This invokes the formation of time reversal symmetry (TRS) protected topological conducting edge states at the boundary between the nontrivial state of HgTe and a trivial insulating state of the vacuum. In the

measurements, tuning the Fermi level into the band gap of a thin HgTe sample leads to a vanishing conductance, a behavior typical for trivial semiconductors, however, thicker samples with edge states in the same regime show finite resistance that approaches the quantized value of  $h/2e^2$ , e.g. one quantum of resistance per each of the two conducting channels (Fig. 3.7a) [96]. Further experiments have also found the 2D topological insulator state in a monolayer of WTe<sub>2</sub>, where the gapless conducting states were observed at the physical edges of the exfoliated material optically [97] and electrically (Figure 3.7b) [92]. In addition, a quantum anomalous Hall effect (QAHE) was demonstrated in a magnetically doped few-layer TI Cr<sub>0.15</sub>(Bi<sub>0.1</sub>Sb<sub>0.9</sub>)<sub>1.85</sub>Te<sub>3</sub>, where the introduction of a magnetic dopant breaks TRS and induces the energy gap in the density of states, allowing to achieve quantized edge states in the absence of the magnetic field [98]. However, these unique quantum phenomena in 2D TIs so far could only be observed at low temperatures due to relatively small band gaps in these materials.

Next, a generalization of a topological insulator state for a 3D case has been proposed, where the material is insulating in the bulk but having conducting states on the surface [99]. Bi-based alloys with Sb, Se and Te have been predicted to be such 3D TIs [44, 100], which was confirmed by ARPES measurements that detected the presence of surface states in Bi<sub>2</sub>Se<sub>3</sub>, Bi<sub>2</sub>Te<sub>3</sub>, Sb<sub>2</sub>Te<sub>3</sub> (Figure 3.7c) [93, 94, 101]. However, these simple TI compounds were found to be weak insulators in the bulk due to their intrinsic doping arising from Se vacancies and defects, which hindered electrical studies of their surface states. To alleviate this issue, quaternary TI compounds Bi<sub>2-*x*</sub>Sb<sub>*x*</sub>Te<sub>3-*y*</sub>Se<sub>*y*</sub> were developed to achieve compensated doping and increase the surface contribution in the transport [102].

The surface states of 3D TIs host massless Dirac fermions with a helical spin texture that leads to the spin-momentum locking (SML), making these states spin-polarized even at room temperature. This effect makes TIs promising for spin-charge conversion, as well as for the spin-orbit torque switching of magnetization for magnetic memory applications [106–112]. To access and investigate the spin-momentum locking in surface states of TIs, optical and electrical methods were used. Spin-resolved ARPES detected the splitting in spin-resolved spectra of Bi<sub>2</sub>Te<sub>3</sub> and confirmed the presence of the spin polarization on its surface (Figure 3.7d) [95]. Electrically, SML was detected using the spin potentiometric measurements [103–105, 113–115]. Figure 3.8a shows a schematic of the TI-based device for SML measurements with two alternative detection geometries. In both cases, electrical current is applied through a surface state of the TI, which induces spin polarization in the channel, and the magnetoresistance between a ferromagnetic contact and the channel is measured using a nonmagnetic contact as a reference. An application of the external magnetic field can switch the magnetization of the FM electrode, which results in step-like changes in the detected signal due to the parallel and antiparallel configurations between the channel spin polarization and FM magnetization (Figure 3.8b) [103]. Reversing the direction

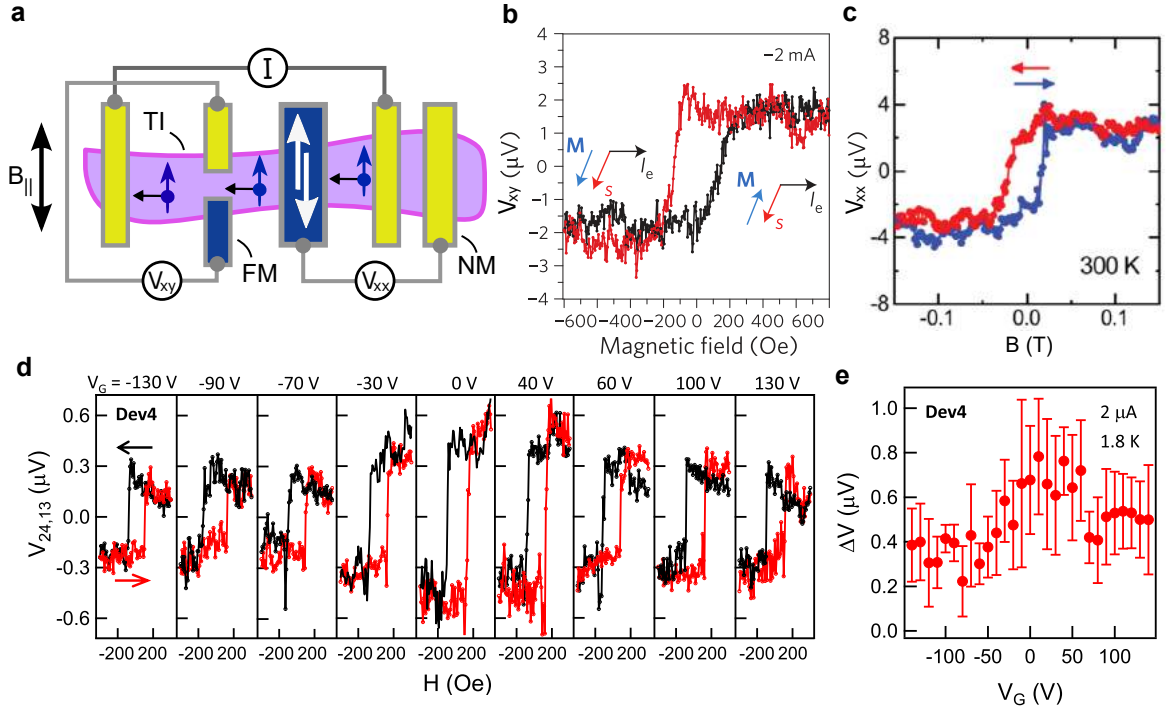


**Figure 3.8:** Electrical detection of spin-momentum locking in TIs. **a**, A schematic of a TI device for potentiometric detection of SML via a transverse  $V_{xy}$  and longitudinal  $V_{xx}$  voltage. **b**, SML signal detected in a transverse configuration in  $\text{Bi}_2\text{Se}_3$ . **c**, SML signal measured in longitudinal resistance up to room temperature. **d**, SML signals measured at various gate voltages corresponding to the hole and electron doping of the surface states. **e**, The magnitude of the SML signal as a function of the gate voltage does not show a change of sign across the Dirac point. Adapted from [103–105].

of the electrical current leads to the opposite spin polarization in the channel, which results in an inverted signal. With the development of the material quality and the fabrication and measurement techniques, the signal was observed up to room temperature (Figure 3.8c) [104].

To prove the spin origin of the observed signals in the electrical measurements of SML, possible contributions from the ordinary Hall effect induced by the out-of-plane component of the stray magnetic fields of FM contacts should be ruled out [117]. For this, measuring the SML signal in the electron- and hole-doped regimes of a TI surface Dirac cone can be used, as shown in Figure 3.8d [105]. Since the spin texture of the TI bands changes sign for electrons and holes (Figure 2.5d), the resulting SML signal is not expected to change its sign across the Dirac point, whereas the stray Hall contributions change sign depending on the carrier type. The absence of a sign change in the measured data (Figure 3.8e) indicates the surface state origin of the signal. Alternatively, the observation of spin precession can serve as a unique signature of the spin transport, however, in high-SOC materials such as TIs the spin is locked to the carrier momentum and



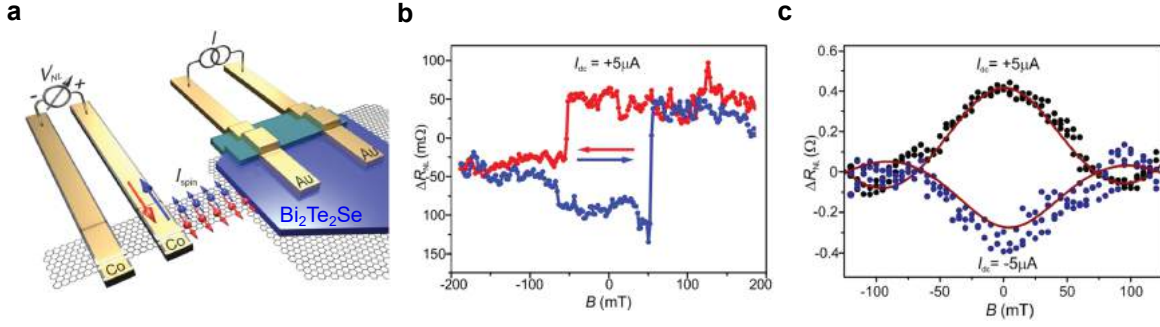


**Figure 3.9:** Spin injection from the surface states of TIs into graphene. **a**, A schematic of the Gr-TI heterostructure utilized for spin injection in the nonlocal geometry. **b**, A nonlocal spin valve signal detected in graphene due to spin injection from the TI. **c**, The presence of the Hanle spin precession signal rules out spurious charge-based effects such as the stray Hall contribution. Adapted from [116].

the spin precession cannot be induced by the magnetic field. To circumvent this issue, graphene can be employed in the sensing circuit to take advantage of its excellent spin transport and precession capabilities, if the spin polarization created by SML in TIs could be injected and probed in the graphene. Such functionality was realized in heterostructures of Bi<sub>2</sub>Te<sub>2</sub>Se epitaxially grown on graphene (Figure 3.9a) [116]. Passing electrical current through two nonmagnetic contacts on top of the TI creates spin accumulation in its surface states, from where spins can diffuse into the adjacent graphene channel. Further transport of the injected spin polarization in the graphene can be detected as a spin voltage via a ferromagnetic electrode in the nonlocal measurement geometry. Applying an external magnetic field along the easy magnetization switching direction of the FM electrode allows to change its polarization and results in a characteristic step-like switching in the detected voltage (Figure 3.9b). The signal could be detected at temperatures up to  $T = 15$  K, above which the conduction through the bulk TI states reduces spin polarization. The observed reduction of the signal with increased TI thickness supports its surface origin and rules out a contribution from the spin Hall effect in the bulk of TI, since the latter is expected to increase in thicker samples [103]. The spin-based nature of the signal was confirmed with the observation of Hanle spin precession, allowing to further characterize the spin transport parameters of the graphene channel (Figure 3.9c). A subsequent study realized spin injection into graphene from a bulk-insulating TI BiSbTeSe<sub>2</sub>, where the spin signal was shown to be tunable by shifting the Fermi level in the TI by the gate voltage, whereas the absence of a sign change across the Dirac point supported the surface origin of the signal [118]. However, no spin precession experiments were presented.



### 3.3 Proximity effects in Gr-TMD heterostructures

Graphene has long spin lifetime and large spin diffusion length due to its low spin-orbit coupling, which makes it an attractive material for the realization of spin interconnects. However, for the development of spin manipulation and active spintronic functionalities, it is necessary to introduce large SOC into the system. First attempts to achieve sizable SOC in graphene employed chemically-adsorbed adatoms on graphene, where the enhancement of SOC was confirmed via spin transport and the observation of spin Hall effect (SHE) [119–125]. However, the introduction of such defects scattered onto graphene can compromise its electrical properties. Alternatively, the heterostructures (HSs) of graphene with other 2D materials, such as transition metal dichalcogenides and topological insulators, have emerged as a promising platform for studying spin-orbit effects in graphene, where the proximity effect allows to introduce an increased SOC into the graphene while preserving its electron transport properties.

#### 3.3.1 Quantum transport and magnetotransport

Motivated by the exotic modifications to the quantum transport phenomena observed in Gr-hBN heterostructures [126–128], the proximity-induced SOC phenomena in heterostructures of Gr and TMDs were extensively studied both theoretically and experimentally [129–142]. A typical Gr-TMD heterostructure is shown in Figure 3.10a. It also presents a sketch showing that the proximity effect in such structures modifies the normal gapless Dirac dispersion of graphene by introducing an orbital gap due to the effective staggered potential on A and B sublattices, and further lifts spin degeneracy of the graphene bands when the SOC is introduced, potentially even inverting the bands (for e.g. Gr-WSe<sub>2</sub>). A clear experimental signature of such an increased SOC in graphene is the observation of a weak antilocalization (WAL) effect, which contrasts with the weak localization (WL) usually present in pristine graphene that lacks SOC. WAL (WL) is a quantum interference effect that provides a positive (negative) correction to the low-temperature magnetoconductivity. Accordingly, WAL was observed in graphene proximitized by WS<sub>2</sub>, MoS<sub>2</sub>, and WSe<sub>2</sub>, proving the emergence of proximity-induced SOC (Figures 3.10b-d) [130, 133, 134, 136, 137, 142]. These measurements revealed the values of proximity-induced SOC strength of  $\lambda = 1 - 15$  meV, significantly larger than the pristine graphene value  $\lambda_i \approx 10$   $\mu$ eV [143]. Furthermore, the strength of proximity-induced SOC was shown to be tunable by the application of hydrostatic pressure, which increases the proximity effect by reducing the physical distance separating the different layers in a heterostructure (Figure 3.10d) [142]. In addition to WAL, the increased SOC and its tunability by the displacement field were confirmed in bilayer graphene-WSe<sub>2</sub> heterostructures via the measurements of the penetration field capacitance. These measurements

are shown in Figure 3.10e, where the arrows point at the features in the measured data that correspond to the SOC-induced spin splitting in either the valence or the conduction band, as the SOC can be freely transferred between them by changing the displacement electric field. This behavior arises due to the fact that the valence and conduction bands of the bilayer graphene are formed primarily from the upper or lower graphene layer depending on the value of the perpendicular electric field, whereas the SOC from the TMD is induced mainly in the bottom graphene layer. This behavior demonstrates a spin-orbit valve functionality [135, 144].

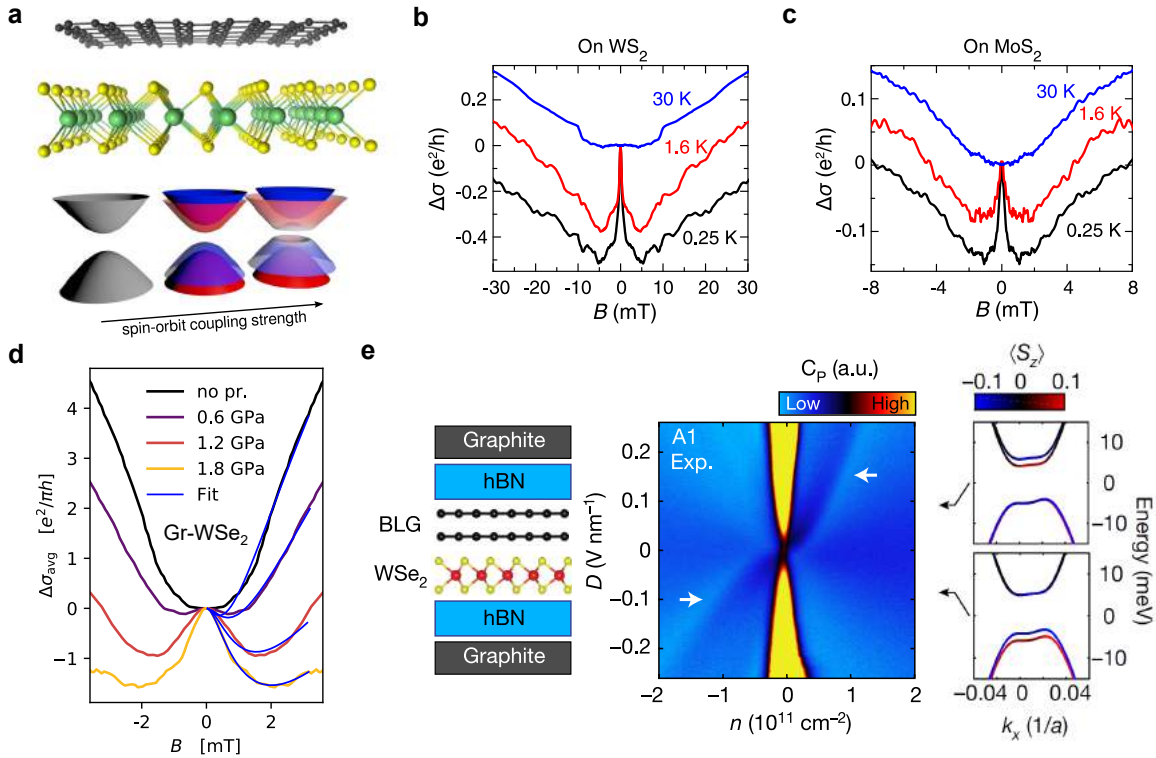


**Figure 3.10:** SOC in Gr-TMD heterostructures. **a**, An atomic structure schematic of a Gr-TMD heterostructure and a sketch of the effect of proximity SOC on the graphene band structure. **b,c**, Weak antilocalization measured in heterostructures of graphene with  $WS_2$  and  $MoS_2$ . **d**, A transition from WL to WAL in a Gr- $WSe_2$  HS as the applied hydrostatic pressure reduces the distance between the materials and consequently increases the strength of proximity SOC. **e**, A schematic of the double-gated BLG- $WSe_2$  device and the measured penetration field capacitance, revealing the features corresponding to the SOC-induced band splitting tunable by both the carrier concentration and the displacement field. The SOC can be tuned to split either the conduction or valence band depending on the applied perpendicular electric field. Adapted from [132, 133, 139, 142].

### 3.3.2 Spin transport

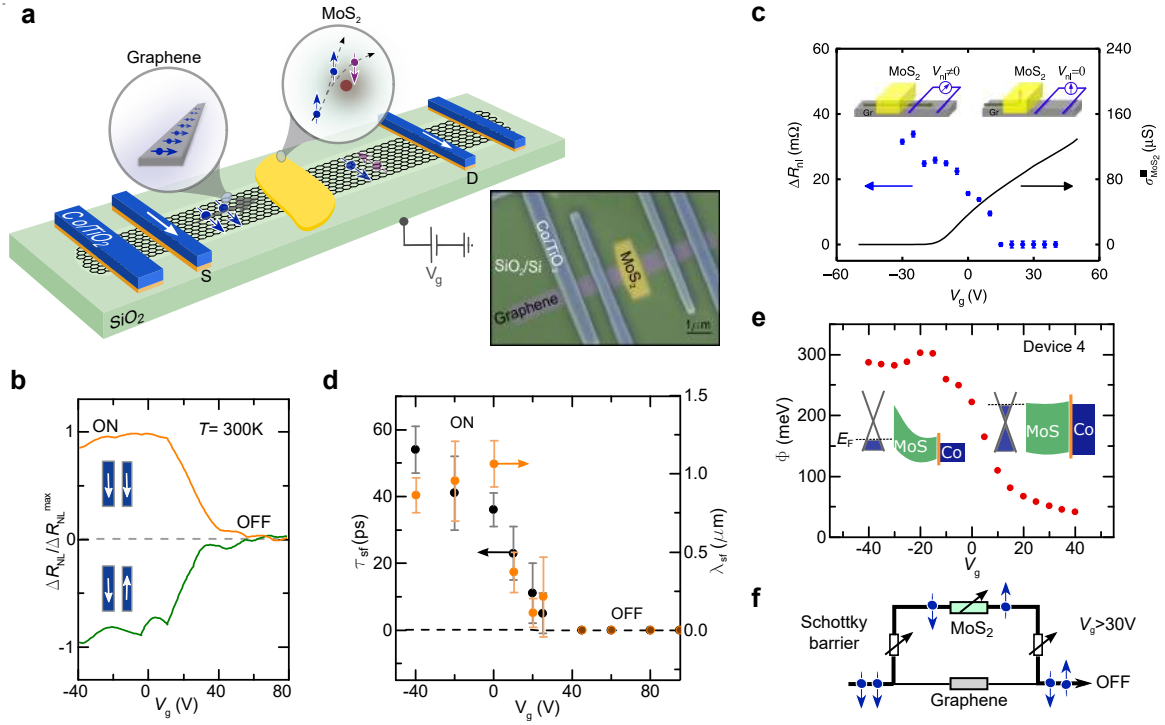


**Figure 3.11:** Field effect control of spin current in Gr-MoS<sub>2</sub> heterostructures. **a**, A schematic and a colored SEM picture of the spintronic device with a Gr-MoS<sub>2</sub> heterostructure. **b,c**, Nonlocal spin voltage controlled by the gate electric field, showing the ON state of devices at negative gate voltage and OFF state at positive gate voltage where the spin signal in graphene is suppressed. **d**, The spin lifetime and spin diffusion length also diminish when the gate voltage is increased. **e**, The gate tunability of the Schottky barrier at the interface between graphene and MoS<sub>2</sub>. **f**, A schematic showing the spin absorption from graphene into the TMD at positive gate voltages that reduce the transport barrier between the two materials and increase the conductivity of the TMD. Adapted from [145, 146].

The experimental signatures of the increased SOC demonstrated the potential of Gr-TMD heterostructures for applications in spintronics. Motivated by these findings, the pioneering spin transport studies in Gr-MoS<sub>2</sub> heterostructures discovered their spin field effect switch functionality, where the spin signal in the channel could be controlled by an application of the gate electric field (Figures 3.11a-c) [145, 146]. In particular, the spin signal was shown to persist at negative gate voltages, but diminish and disappear completely when the gate voltage was tuned above a threshold value  $V_g \sim 30$  V (Figures 3.11b,c). Such behavior was first observed in heterostructures implemented with the exfoliated graphene spin valves at low temperatures, and further confirmed at room temperature with CVD graphene devices by spin precession experiments (Figure 3.11d), where also a reduction of spin lifetime  $\tau_s$  and spin diffusion length  $\lambda_s$  with the

gate voltage was demonstrated. The functionality of these devices was attributed to the variable degree of spin absorption from graphene into the TMD, governed by the gate-dependent Schottky barrier strength at the Gr-MoS<sub>2</sub> interface and by the strong modulation of MoS<sub>2</sub> conductivity (Figures 3.11e,f). At negative gate voltages, the high Schottky barrier and low conductivity of MoS<sub>2</sub> prevent spins from entering the TMD, and hence the spins are transported normally in graphene. At positive gate voltages, the Schottky barrier strongly reduces while the conductivity of MoS<sub>2</sub> increases, allowing the spins to jump from graphene to MoS<sub>2</sub> where they rapidly dephase due to its high SOC, which leads to the suppression of the output spin signal. Although this description is based primarily on the individual properties of graphene and TMDs and does not involve proximity interactions, subsequent studies found that spin-orbit effects in similar heterostructures lead to spin lifetime anisotropy, which can also play a role in the observed gate-dependent spin functionality.

### 3.3.3 Spin lifetime anisotropy

A common feature of materials with high and directional SOC is the spin lifetime anisotropy, which denotes different relaxation times for spins polarized in different directions. As the intrinsic SOC in pristine graphene is small, the SOC effective fields are not strong enough to make any given direction of the spin more favorable than others, yielding isotropic spin scattering at room temperature [147–151]. However, the situation changes in proximity-modified graphene, where the emergence of strong SOC fields leads to unequal relaxation times for the in-plane and out-of-plane spins. This gives rise to spin lifetime anisotropy that is commonly quantified by the ratio of spin lifetimes for differently polarized spins  $\xi = \frac{\tau_{\perp}}{\tau_{\parallel}}$ .

The intricate interplay of different contributions to the SOC from the intrinsic (also known as Kane-Mele SOC), Rashba, valley-Zeeman (also known as Ising SOC), and pseudospin inversion asymmetry (PIA) terms determines the details of spin dynamics and the orientation of spin textures in heterostructures of 2D materials [41, 131, 132, 152, 153]. The intrinsic SOC in graphene is negligibly small due to the small atomic number of carbon. Rashba SOC, which arises from the perpendicular electric field at the Gr-TMD interface due to broken inversion symmetry, acts as an effective magnetic field oriented in the graphene plane, promoting the formation of in-plane spin texture and suppressing the out-of-plane spin component. PIA SOC arises in similar conditions due to the breaking of mirror symmetry with respect to the  $xy$  crystal plane, and also promotes in-plane spin polarization. In their theoretical description, both Rashba and intrinsic SOC are denoted by coupling terms that have the same sign for  $K$  and  $K'$  valleys. On the other hand, valley-Zeeman SOC has opposite signs for  $K$  and  $K'$ , arising from the in-plane mirror symmetry breaking. This symmetry between carbon atoms in graphene sublattices A and B breaks when the graphene is placed in heterostruc-

tures with materials that themselves lack such symmetry (hBN, TMDs), since the atoms from different graphene sublattices experience different potentials from the neighboring layers. Valley-Zeeman effective SOC fields are directed out of the graphene plane and lead to the suppression of in-plane spin polarization, resulting in the tilting of the spin texture out of the plane.

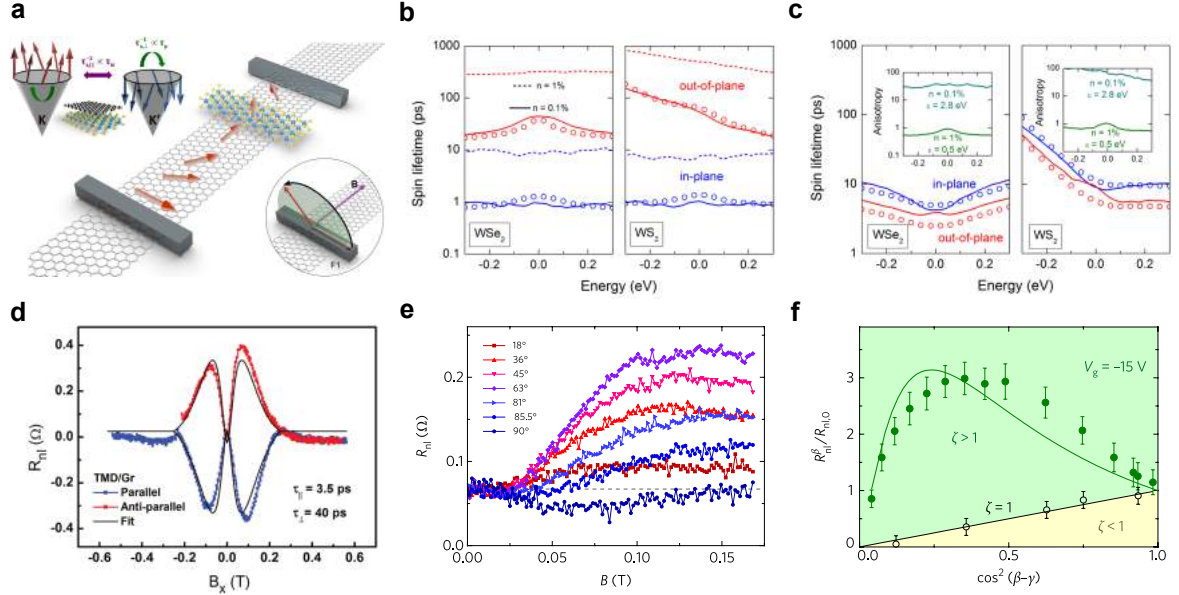


**Figure 3.12:** Spin lifetime anisotropy in proximitized graphene. **a**, A schematic of a Gr-TMD device for estimation of spin lifetime anisotropy. **b,c**, Theoretical calculations of the energy-dependent spin lifetime anisotropy in heterostructures of graphene with WSe<sub>2</sub> and WS<sub>2</sub> for the cases with high (valley-Zeeman system) and low (Rashba system) strengths of the intervalley scattering respectively. The insets show the giant anisotropy in both heterostructures when the VZ SOC dominates. **d**, Spin precession data in a Gr-TMD heterostructure with the in-plane field  $B_x$ , showing a stronger signal for the out-of-plane spins compared to the in-plane ones. **e**, Spin precession curves obtained in a Gr-TMD heterostructure with oblique magnetic fields  $B_\beta$ . **f**, Normalized amplitude of the spin signal in a fully dephased regime. The solid line represents a modeled response for a Gr-TMD structure with large anisotropy  $\xi = 10$ . Adapted from [154–156].

Theoretical studies have predicted large spin lifetime anisotropy in heterostructures where proximity-induced valley-Zeeman SOC dominates over other terms, which suppresses the in-plane spin components and results in  $\tau_\perp > \tau_\parallel$  and  $\xi > 1$  (Figure 3.12b). On the other hand, in the heterostructures with dominating Rashba SOC the out-of-plane spin components are suppressed, resulting in  $\tau_\perp < \tau_\parallel$  and  $\xi < 1$  (Figure 3.12c) [155].

To access and quantify the spin lifetime anisotropy experimentally, several methods have been developed, including the spin transport with direct injection of in-plane and out-of-plane polarized spins, spin precession in the in-plane

field  $B_x$ , and spin precession in oblique magnetic fields  $B_\beta$ . Early studies of spin transport in graphene have revealed mostly isotropic spin lifetime behavior by comparing the steady-state spin signal amplitudes corresponding to the injection of in-plane and out-of-plane spins [147]. While this method allows an easy visual assessment of spin lifetime anisotropy, it requires large magnetic fields ( $B_z > 1.5$  T) to polarize the injector and detector FMs along their hard out-of-plane magnetization direction, and thus it is prone to adverse effects related to the graphene magnetoresistance.

An alternative method of extracting spin lifetime anisotropy was utilized in Gr-TMD heterostructures, where spin precession was induced by applying an external magnetic field  $B_x$  along the channel perpendicularly to the magnetization of injector and detector FMs (Figure 3.12a) [156]. Such field induces spin precession in the  $yz$ -plane, leading to the spin signal being dependent on both  $\tau_\parallel$  and  $\tau_\perp$ . The measured curves, shown in Figure 3.12d, demonstrate a significantly larger spin signal at intermediate values of the applied field  $B_x$  compared to the signal at  $B_x = 0$ . This signifies that spins polarized out of the plane can pass through the heterostructure region more easily compared to the in-plane spins, which is underlined in the estimated value of the spin anisotropy ratio  $\xi = 11$ .

A third method involves the spin precession in oblique magnetic fields applied at various angles  $\beta$  with respect to the easy magnetization switching direction of the electrodes in the  $yz$ -plane [148]. Such measurement geometry leads to dephasing of all spin components that are non-collinear with the field, making the output signal amplitude defined by the lifetime of spins parallel to the field. In Gr-TMD heterostructures such measurements show a strong increase in spin signal magnitude as soon as an out-of-plane spin component appears, indicating large spin lifetime anisotropy (Figure 3.12e) [154, 157]. It can be further visualized by plotting the normalized spin signal amplitude vs.  $\cos^2(\beta)$  (Figure 3.12f). In such representation, the isotropic spin relaxation yields a straight line, whereas  $\xi > 1$  ( $\xi < 1$ ) renders data above (below) that line. Accordingly, the experimental data in a Gr-TMD HS falls close to the predicted trend for  $\xi = 10$ . Applying the gate voltage allows to control the carrier density in both the graphene and TMD, changes their conductivity and interface transparency, and it can also tune the strength of their proximity interaction. However, its effect on the spin lifetime anisotropy ratio so far is largely unexplored, which marks an interesting direction for the future research. These observations of large spin lifetime anisotropy via oblique spin precession prove it a valuable method for investigating spin and valley dynamics arising due to proximity effects in graphene-based heterostructures. The large and electric-field tunable spin anisotropy can be useful for the realization of active spin devices such as spin filters or polarizers that can select and filter out certain spin polarization modes from spin currents.

### 3.3.4 Spin-charge conversion

The spin-orbit coupling induced in graphene via proximity effects from adjacent 2D materials can be utilized to realize spin-charge interconversion in such heterostructures. The advantage of this method over the other means to perform such a conversion is that both spin transport and spin generation/detection can be performed within graphene itself, alleviating the challenges related to spin current transfer through interfaces between different materials. The spin-charge conversion (SCC) can be realized via the spin Hall effect and/or the spin-galvanic effect [158].

#### Proximity-induced spin Hall effect

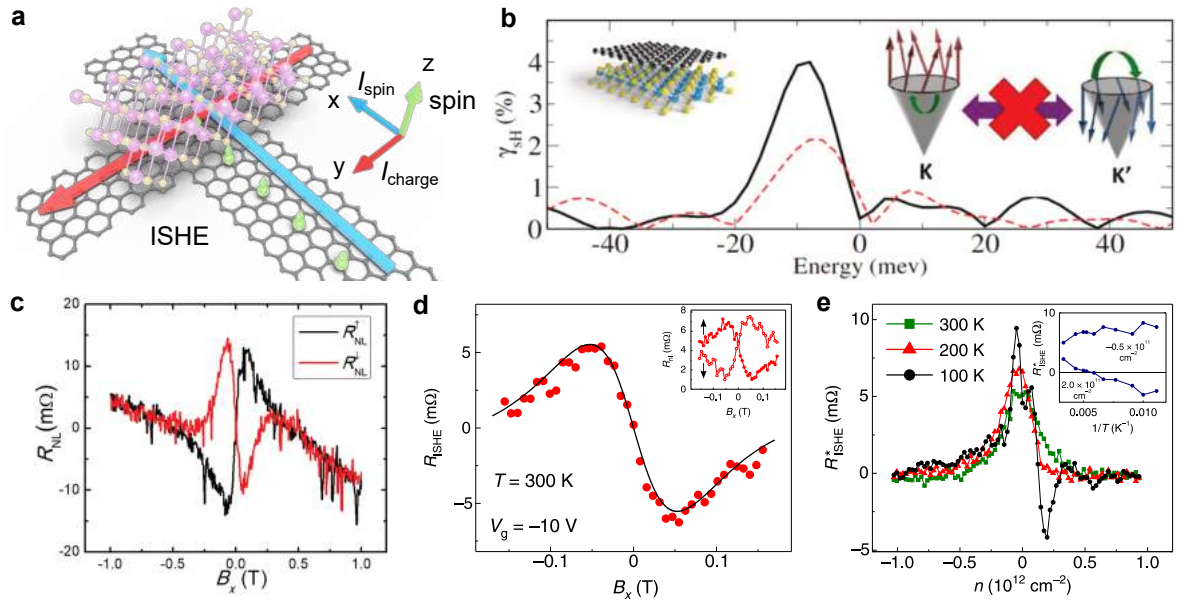


**Figure 3.13:** Proximity-induced spin Hall effect in graphene. **a**, A schematic showing the inverse spin Hall effect (ISHE), where the spin current with an out-of-plane polarization induces a transverse charge current. **b**, Theoretical calculations predict spin Hall angles on the order of 1% with a nontrivial dependence on the Fermi energy in proximitized graphene. **c,d**, Experimentally detected ISHE spin precession signals in Gr-TMD heterostructures with the in-plane field  $B_x$ . **e**, Carrier density dependence of the ISHE signal magnitude at different temperatures shows a pronounced tunability of the proximity-induced spin-charge conversion in the graphene. Adapted from [153, 159, 160].

Spin Hall effect is a 3D phenomenon present in materials with high SOC, where the application of a charge current leads to a creation of spin current, with the constraint of orthogonality between the spin polarization, spin current direction and charge current direction [158]. Note that in 3D systems with decreasing crystal symmetry, such as strained TMDs or their low-symmetry phases (e.g. 1T'



or  $1\text{T}_d\text{ MoTe}_2$ ), this orthogonality requirement is gradually lifted [161]. Adhering to Onsager reciprocity, the inverse spin Hall effect (ISHE) denotes a conversion of spin current into charge current with the same orthogonality constraints. As graphene is an atomically thin 2D material, it can support the (I)SHE only for spins polarized out-of-plane with spin current and charge current being in plane and perpendicular to each other (Figure 3.13a).

Theoretical studies have predicted sizable spin Hall conductivity in graphene proximitized by  $\text{WS}_2$ ,  $\text{WSe}_2$ ,  $\text{MoS}_2$ , and  $\text{MoSe}_2$ , with largest spin Hall angles seen in graphene/ $\text{WS}_2$  where they reach few percent depending on the Fermi energy (Figure 3.13b) [41, 153]. In these heterostructures, the *intrinsic* SHE mechanism was considered, in which the proximity effect imprints into graphene the out-of-plane sublattice-dependent valley-Zeeman SOC, originating from the broken sublattice symmetry in a TMD.

Shortly after, the experimental evidence of proximity-induced (I)SHE was obtained in heterostructures of graphene with  $\text{MoS}_2$  [159],  $\text{WS}_2$  [160, 162], and  $\text{WSe}_2$  [163]. The ISHE measurements were performed by injecting the spin-polarized current in graphene from a ferromagnetic electrode, which diffuses into a Gr-TMD heterostructure and creates a transverse charge current. To create the out-of-plane spin polarization, an in-plane field  $B_x$  was applied, which induces spin precession in the  $yz$ -plane and results in an antisymmetric SHE spin precession signal of opposite signs for different initial states of the injector FM magnetization (Figure 3.13c,d).

Interestingly, it was found that sizable SHE can be observed in heterostructures that also exhibit large spin lifetime anisotropy [163], whereas the theoretical investigations predicted these phenomena to be incompatible because the intervalley scattering and valley mixing, required for the anisotropy, are detrimental for the *intrinsic* SHE mechanism since they effectively reduce the mass of the carriers [153]. In addition, an observation of SHE is reported in graphene proximitized by a high-SOC amorphous insulator  $\text{Bi}_2\text{O}_3$ , which lacks an ordered crystal lattice that could break the in-plane mirror symmetry of the graphene layer [164]. These observations hint at the presence of additional *extrinsic* mechanisms for SHE, for which it was suggested that the inhomogeneities at the graphene interface induce long-range potentials that can cause SHE without a global alteration of the band structure of graphene [164]. However, further work is required to establish the exact origin and role of the *intrinsic* and *extrinsic* SHE mechanisms.

The efficiency of spin to charge conversion by SHE is often quantified by the spin Hall angle  $\theta$ , which denotes the ratio of spin current density and charge current density that are involved in the conversion. The experiments report room-temperature values of  $\theta = -0.33\%$  in Gr- $\text{MoS}_2$ ,  $\theta = 0.3\%$  in Gr- $\text{WS}_2$ , and  $\theta = 1.7\%$  in Gr- $\text{WSe}_2$ , in line with the theoretically predicted values for Gr-TMD heterostructures (Figure 3.13b). However, larger spin Hall angles can be obtained since the device properties can be strongly tuned by temperature and gate voltage.



The theoretical studies predict energy-dependent spin-charge conversion efficiency due to the asymmetric SHE magnitude for holes and electrons, with stronger signals expected upon increasing hole doping, and a sign change across the Dirac point is anticipated [153]. This was confirmed experimentally in Gr-WS<sub>2</sub>, however, due to the signal smearing by charge puddles at room temperature, the sign change could only be resolved upon device cooling below  $T = 200$  K (Figure 3.13e) [160]. By optimizing the experimental conditions and parameters, the values of spin Hall angle were boosted up to  $\theta = 8.4\%$  in Gr-WSe<sub>2</sub> [163], exceeding theoretical predictions which again hints at the presence of *extrinsic* mechanisms.

Although the spin Hall angle in Gr-TMD heterostructures is smaller than the values seen in heavy metals like Pt, the spin-charge conversion efficiency can still be higher. This is because both the spin transport and spin-charge conversion happen in the same material (graphene), whereas in the case of Pt its high  $\theta$  is negated by the lossy transfer of spins through the interface between the spin transport channel and the heavy metal. With these considerations, an effective spin Hall resistance  $R_{\text{eff}}$  has been proposed as an alternative figure of merit of SHE efficiency, denoting the ratio of the output spin Hall voltage and input spin current that reaches the spin-charge conversion region [159]. The obtained values in Gr-WSe<sub>2</sub> heterostructures at room temperature  $R_{\text{eff}} = 21 \Omega$  demonstrate the high potential of proximity-induced SHE for spin-charge conversion applications compared to conventional devices with heavy metals ( $R_{\text{eff}}$  of Gr/Pt  $< 1 \Omega$ ) [163, 165].

### Proximity-induced spin-galvanic effect

Spin-galvanic effect (SGE), also known as the inverse Rashba-Edelstein effect, denotes the conversion of spin density into a charge current in samples with strong SOC and a spin texture (Figure 3.14a) [158, 167]. This phenomenon is attributed to the in-plane Rashba SOC, which arises from the perpendicular electric field due to broken inversion symmetry at the heterostructure interface. Theoretical investigations have predicted that high-SOC 2D materials in heterostructures with graphene can induce spin winding (spin textures) in its low-energy states, which leads to asymmetric spin-dependent scattering and enables current-driven spin polarization via SGE (Figure 3.14b) [41, 131, 132, 135, 152]. Unlike SHE, which is a 3D phenomenon, SGE is 2D and does not depend on the spin current direction, only on the direction of spin polarization. In addition, in Rashba systems with in-plane spin textures, only in-plane spins can participate in the spin-charge conversion by SGE, unlike the proximity-induced SHE in graphene which can only induce out-of-plane spins. Thus, by probing the spin-charge conversion for differently polarized spins, SGE and SHE can be differentiated and their contributions to the total spin-charge conversion signal in proximitized graphene can be untangled.

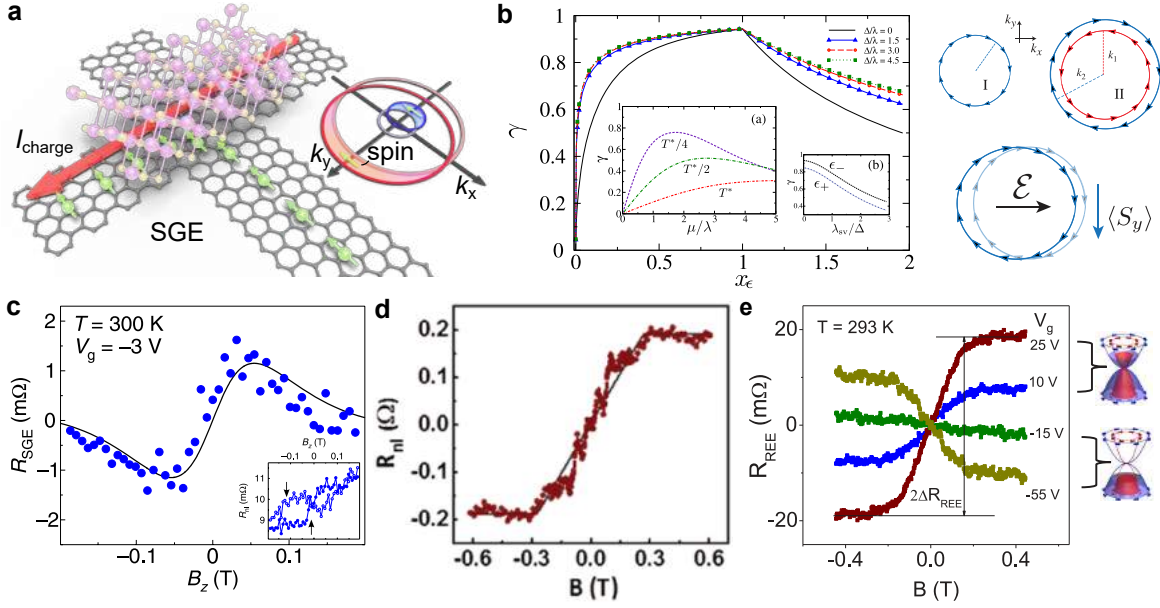


**Figure 3.14:** Proximity-induced spin-galvanic effect in graphene. **a**, A schematic showing the SGE, where the spin-polarized carriers entering the proximitized graphene region acquire transverse momentum and create a charge current. **b**, Theoretical calculations of the SGE efficiency show its strong dependence on the position of Fermi energy. The compensation of the spin-charge conversion signal due to the opposite spin windings of the inner and outer Rashba-split bands is shown. **c**, Spin-galvanic signal obtained in a Gr-WS<sub>2</sub> heterostructure using spin precession in  $B_z$ . **d**, SGE in Gr-WS<sub>2</sub> measured with an applied magnetic field  $B_x$  to rotate the magnetization of FM contacts along the graphene channel. **e**, An application of the gate voltage shows electric-field tunability of the magnitude and sign of SGE observed in a heterostructure of graphene and 2H-TaS<sub>2</sub>. Adapted from [152, 160, 162, 166].

Experimentally, the proximity-induced SGE was observed in heterostructures of graphene with MoS<sub>2</sub> [159], WS<sub>2</sub> [160, 162], and 2H-TaS<sub>2</sub> [166]. Similarly to SHE, the measurement protocol includes the injection of spin polarization into a heterostructure region from a FM contact and a detection of the converted charge current (or open-circuit voltage) perpendicularly to the spin channel (Figure 3.14a). Alternatively, inverse SGE can be observed by applying a bias current across the heterostructure and detecting the created spin density using a spin-sensitive FM contact in a nonlocal configuration. In common Hall bar devices, where the graphene in one of the crosses is proximitized by a TMD, SGE can be invoked only by the spins polarized along the channel ( $x$ -direction in Fig. 3.14a), whereas the easy axis of FM electrodes, and therefore the initial orientation of the injected spins, is along the  $y$ -direction. To observe SGE, the required spin polarization along  $x$  can be created by spin precession in  $B_z$  (Figure 3.14c) [160], or by applying larger field  $B_x$  to align the FM polarization along its hard axis  $x$  (Figure 3.14d) [159, 160, 162, 166]. In the latter case, great care should be taken

to rule out spurious effects arising from the ordinary Hall effect induced by the stray fields of FM electrodes, which can mimic the spin-charge conversion signal.

To quantify SGE, a conversion efficiency parameter  $\gamma$  can be used, defined as the ratio of charge current density and spin accumulation participating in the spin-charge conversion. However, as this parameter has nontrivial units ( $\text{A J}^{-1} \text{m}^{-1}$ ), an alternative unitless merit of SGE efficiency  $\alpha$  was proposed [159], obtained as a ratio between 2D charge current and 2D spin current (assuming the spin polarization to be converted to spin current by diffusion) and related to  $\gamma$  via  $\alpha = e\gamma R_{\text{sq}} \lambda_{\text{eff}}$ . This SGE efficiency can be straightforwardly compared with spin Hall angles and spin polarization values of conventional FM contacts (5 – 10%). So far, the reported values of room-temperature SGE efficiency  $\alpha$  reach 3% in Gr-MoS<sub>2</sub> [159], 0.1% in Gr-WS<sub>2</sub> [160], and 4.3% in Gr-TaS<sub>2</sub> [166]. Moreover, the spin-galvanic signal in graphene heterostructures was shown to be strongly gate-tunable in magnitude (Gr-WS<sub>2</sub> [162]) and also its sign (Gr-WS<sub>2</sub> [160], Gr-TaS<sub>2</sub> [166]) at room temperature, demonstrating it as a versatile alternative to conventional spin creation/detection means.

## 3.4 Heterostructures of graphene and TIs

The unique electronic and spintronic properties of TIs stemming from their large internal spin-orbit coupling make these materials promising for applications in active spin-based devices and spin-charge conversion systems. Unlike conventional TMDs, the SOC in TIs is strong enough to cause band inversion, leading to the formation of topologically-protected spin-polarized metallic surface states [25]. Interestingly, the energy dispersion of these surface states is linear in momentum, so the carriers are described as massless Dirac fermions similarly to graphene [168]. However, the two materials possess strikingly differing strengths of spin-orbit coupling, which makes the heterostructures between these materials an attractive playground for investigating spin manipulation possibilities, exotic topological states, and emerging proximity-induced SOC effects.

### 3.4.1 Band hybridization and proximity-induced spin textures

Several reports have theoretically investigated the heterostructures of graphene and topological insulators to study the hybridization between these two Dirac materials and characterize the proximity-induced spin-orbit coupling effects arising in these systems [169–181]. It was shown that the control over the the alignment of crystal lattices in Gr-TI heterostructures is crucial as it defines the symmetries present in a unit cell and drastically affects the presence and contributions of various spin-orbit terms that govern the details of proximity interactions [169]. In contrast to TMDs, which have relatively large mismatch of their lattice constants with graphene, the lattice parameters of Gr and TIs allow to achieve highly commensurate structures and small unit cells with only a few percent of mismatch ( $a_{TI}/\sqrt{3}a_{Gr} \approx 1$ ). Figure 3.15a shows two examples of possible unit cells in a Gr-Bi<sub>2</sub>Se<sub>3</sub> heterostructure. If the lattices are rotated by precisely 30°, a highly commensurate structure emerges with a small  $\sqrt{3} \times \sqrt{3}$  supercell [169, 170]. In case of other rotation angles between the two crystals, for example 0°, the structure is incommensurate and can be described by a large  $5 \times 5$  supercell in a similar manner as Gr-TMD HSs.

In a small unit cell, the Kekulé distortion, which arises from spatially periodic perturbations, is present, the sublattice symmetry is preserved and thus the valley-Zeeman (VZ) SOC and pseudospin inversion asymmetry (PIA) SOC are absent, and the Rashba SOC terms originating from the perpendicular electric field and radial in-plane field are present. The formation of a  $\sqrt{3} \times \sqrt{3}$  supercell leads to the folding of graphene Dirac cones from K and K' points onto the  $\Gamma$  point of the first Brillouin zone. Figure 3.15b shows the band structure of graphene placed in a heterostructure with one quintuple layer (QL) of Bi<sub>2</sub>Se<sub>3</sub> calculated using the density functional theory (DFT). The red lines represent the graphene Dirac bands and the black ones are the bulk states of the TI. The surface states

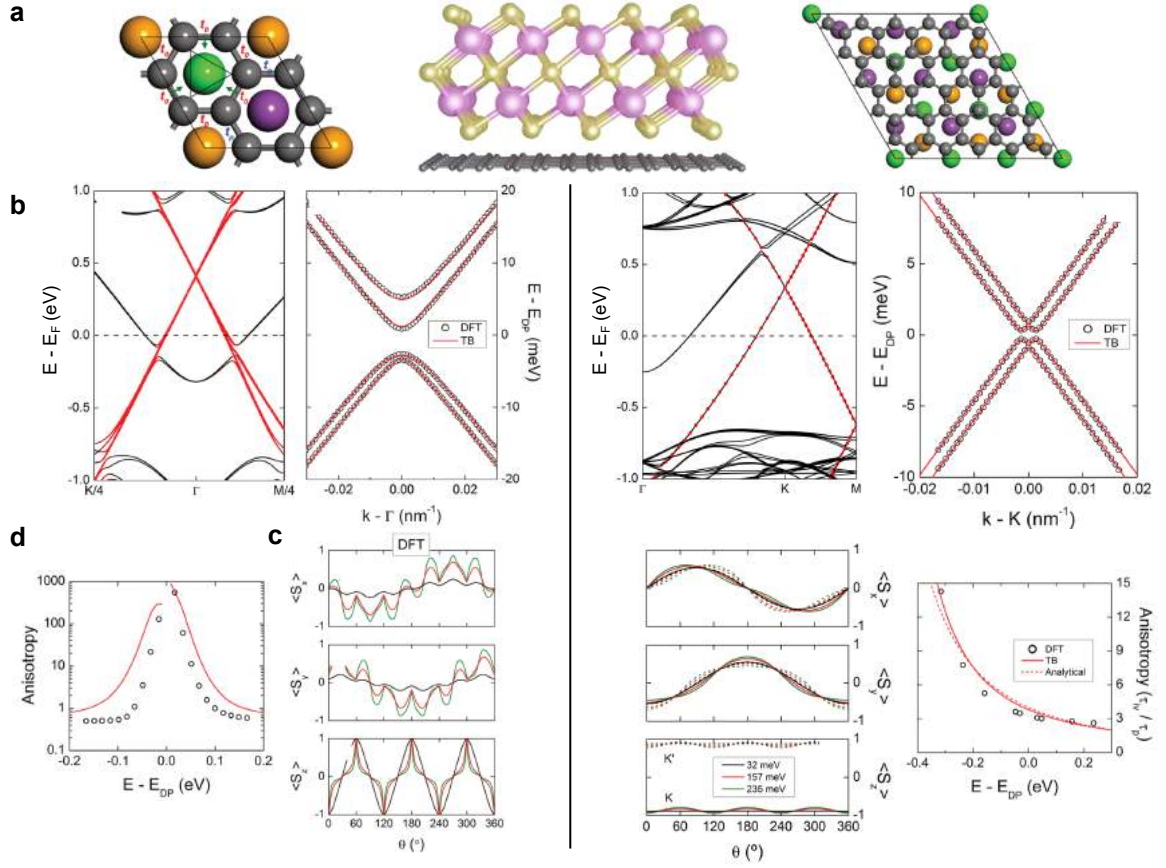


**Figure 3.15:** Theoretical descriptions of graphene-TI heterostructures. **a**, A schematic of the graphene-TI heterostructure and the considered unit cells for calculations. The graphs on the left side of the figure show the results obtained with the commensurate stacking and a small  $\sqrt{3} \times \sqrt{3}$  supercell, whereas the graphs on the right side correspond to the incommensurate stacking and a large  $5 \times 5$  supercell. **b**, Band structure of a graphene-Bi<sub>2</sub>Se<sub>3</sub> hybrid system. **c**, Spin texture induced in the graphene proximitized by a TI. **d**, Spin lifetime anisotropy in Gr-TI HSs. Adapted from [169].

are absent since they form only when the TI thickness is  $\geq 6$  QLs. However, the proximity-induced SOC effects in graphene do not have a strong dependence on the TI thickness or the presence of the surface states. A zoom-in onto the Dirac point of proximitized graphene reveals the emergence of a band gap and the spin splitting of the bands on the order of a few meV. Figure 3.15c shows the calculated spin texture in the graphene bands, which overall exhibits a Rashba-like behavior with winding in-plane spin components  $s_x$  and  $s_y$ , but the Rashba SOC term due to the in-plane radial electric fields decorates it with sharp minima every  $60^\circ$  around the Fermi circle. Importantly, the out-of-plane spin component  $s_z$  is generally nonzero and exhibits maxima at the same points. Notably, the spin texture exhibits a strong energy dependence, with the in-plane components reducing and the out-of-plane component increasing at energies closer to the Dirac

point. With the obtained in-plane and out-of-plane spin lifetimes, a spin lifetime anisotropy ratio can be estimated as shown in Figure 3.15d. In this commensurate structure, the anisotropy at energies far from the Dirac point is close to the typical value for a Rashba system  $\xi \sim 1/2$ , but, due to the suppression of the in-plane spin components near the DP, it can reach giant values  $\xi > 100$  close to the charge neutrality point.

In a large unit cell, the Kekulé distortion is absent, the sublattice symmetry is broken so the valley-Zeeman SOC and PIA SOC terms appear, and the Rashba SOC term originating from the perpendicular electric field is present whereas the term from radial in-plane field is absent due to the lack of the radial symmetry. In this configuration, the graphene Dirac cones do not fold onto the  $\Gamma$  point but remain at K and K', and they still experience the spin splitting and develop a band gap (Figure 3.15b). The spin texture of the graphene bands for the large unit cell in Figure 3.15c does not exhibit sharp features with  $60^\circ$  periodicity due to absence of hybridization between valleys in this configuration, and resembles a conventional winding Rashba spin texture. However, the out-of-plane spin component becomes momentum-independent, always large in magnitude, and has opposite signs for the K and K' valleys. This behavior is driven by the presence of the VZ SOC and resembles the results seen in Gr-TMD heterostructures [132, 155]. In this case, the spin lifetime anisotropy has only a modest energy dependence but exhibits a large electron-hole asymmetry and can reach values  $\xi \sim 10$ .

These investigations underline the importance of the relative alignment of crystal lattices between the heterostructure materials as the twist angle strongly affects the resulting strength of the proximity effect, the size of the induced SOC, the induced spin texture, and the expected degree of spin lifetime anisotropy. Thus, it is important to consider the crystal alignment to interpret the experimental results. However, the commonly utilized fabrication techniques based on random exfoliation and mechanical stacking of the crystals usually result in heterostructures with random twist angles, which are likely to follow the large supercell description of proximity interactions. In this case, measurements of spin relaxation anisotropy may be used to elucidate the crystal alignment. Alternatively, highly commensurate structures exhibiting small unit cell physics can be obtained by carefully aligning the layers during the mechanical stacking using a micromanipulator, or via the bottom-up approach with the epitaxial growth of heterostructure materials [182].

### 3.4.2 Electrical characterization of Gr-TI HSs

Experimental studies of Gr-TI heterostructures so far have been mainly focused on the characterization of their electrical and quantum transport properties, with only a few works addressing the proximity-induced SOC effects arising in graphene. The studies of the electrical transport through the interfaces between graphene

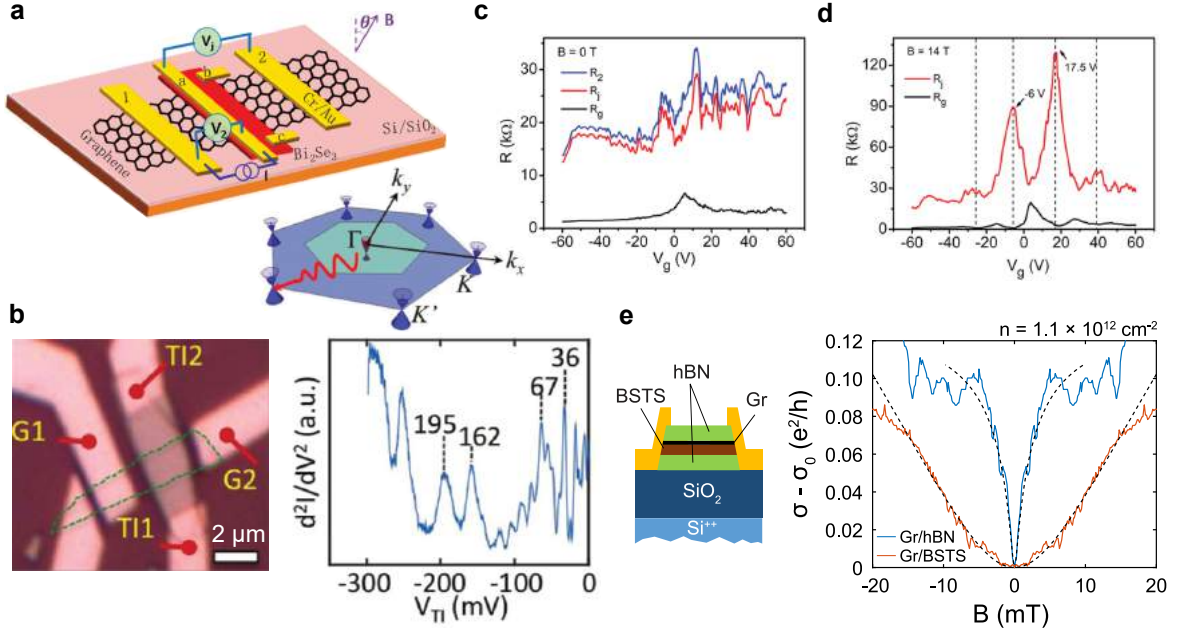


**Figure 3.16:** Experimental studies of graphene-topological insulator heterostructures. **a**, A drawing of the Gr-TI heterostructure utilized for measuring the junction resistance. A schematic shows phonon-assisted tunneling in momentum mismatched materials, where the graphene Dirac cones are situated at the corners of the Brillouin zone in  $K$  and  $K'$  points, whereas the TI Dirac cone is placed in the center of the Brillouin zone in the  $\Gamma$  point. **b**, Left panel: An optical microscope picture of the bilayer graphene- $\text{Bi}_2\text{Se}_3$  junction utilized for the differential conductance characterization. Right panel: A spectrum of inelastic tunneling features observed in the second derivative of the conductivity, indicating the phonon modes mediating the tunneling process. **c**, The gate-dependent resistance of Gr-TI junction shows electron-hole asymmetry, which indicates varying tunneling barrier strength for the valence and conduction bands of graphene. **d**, A comparison of the junction resistance and graphene resistance in the quantum Hall regime indicates that the Gr-TI resistance is inversely proportional to graphene DOS. **e**, Left: A schematic of the Gr- $\text{Bi}_{1.5}\text{Sb}_{0.5}\text{Te}_{1.7}\text{Se}_{1.3}$  (BSTS) heterostructure encapsulated in hBN. Right: Weak localization measurements in pristine and proximitized graphene show significant differences in the highly doped regime due to the effects of proximity-induced SOC. Adapted from [183–185].

and topological insulators revealed the presence of a junction tunneling barrier (Figure 3.16a,b) [183, 184]. Possible reasons for the observed effective tunnel junction behavior of the Gr-TI interface include the oxidation of  $\text{Bi}_2\text{Se}_3$  due to its exposure to air during the device fabrication, differences in the effective contact area, or the lack of direct chemical bonding between the layers. The differential conductance measurements indicated the presence of an inelastic phonon-assisted tunneling process. Since the graphene Dirac cones are placed in  $K$  and  $K'$  points at the edges of the Brillouin zone, whereas the TI Dirac cone is at the  $\Gamma$  point



at the center of the Brillouin zone, there is a large momentum mismatch between graphene and  $\text{Bi}_2\text{Se}_3$  Fermi surfaces (Figure 3.16a). To compensate for this momentum mismatch, the inelastic tunneling conduction through the Gr-TI interface is assisted by the  $\text{Bi}_2\text{Se}_3$  surface optical phonon as well as the out-of-plane, longitudinal, and transverse acoustic/optical phonon modes in graphene (Figure 3.16b). The gate dependence of the tunneling interface resistance at  $T = 2\text{ K}$  displayed a significant electron-hole asymmetry, which indicated varying tunneling barrier properties for conduction and valence bands of graphene (Figure 3.16c). With an application of the large perpendicular magnetic field  $B = 14\text{ T}$  the graphene was tuned into the quantum Hall insulator state, where the Gr-TI junction resistance was shown to exhibit maxima at points where the graphene longitudinal resistance exhibits minima (Figure 3.16d). As these minima occur when the Fermi level falls between the Landau levels in graphene, the tunneling resistance was shown to be inversely proportional to the density of states in graphene.

To investigate the proximity-induced SOC effects in graphene, low-temperature magnetoresistance effects in Gr-TI heterostructures were studied. An evidence for the proximity-induced SOC in graphene in heterostructures with a topological insulator  $\text{Bi}_{1.5}\text{Sb}_{0.5}\text{Te}_{1.7}\text{Se}_{1.3}$  (BSTS) was obtained through the phase-coherent magnetotransport measurements in the weak localization regime [185]. When the graphene was doped near its Dirac point, weak localization was observed with similar linewidths in both proximitized and pristine graphene samples, however, a significantly narrower signal was obtained in the Gr-BSTS heterostructure at increased carrier density (Figure 3.16e). The carrier density dependence of the extracted phase coherence length  $\ell_\phi$  in Gr-TI HSs was shown to exhibit a maximum at the Dirac point, in contrast to the pristine graphene trend which showed a minimum at low carrier density. These results indicate that the proximity-induced SOC in Gr-TI HSs increases the role of D'yakonov-Perel' type of spin relaxation, and is predominantly symmetric upon  $z/-z$  inversion, which explains the absence of weak antilocalization. The observed behavior was found to be consistent with the proximity SOC of either Rashba (induced by the in-plane fields) or valley-Zeeman type, with the strength of  $\lambda_{\text{sym}} = 2.5\text{ meV}$ . Another study has investigated the quantum Hall effect in graphene proximitized by a TI, and found that the coupling between the two materials can be affected by the perpendicular magnetic field [186]. It was shown that the forward- and backward-propagating quantum Hall edge states in graphene can interact with each other via the coupled  $\text{Bi}_2\text{Se}_3$  nanoribbon, which causes the Hall conductivity to deviate from the perfectly quantized values in the electron-doped regime due to momentum relaxation via the  $\text{Bi}_2\text{Se}_3$  bulk states.

These theoretical studies and initial experiments demonstrated Gr-TI systems as an intriguing material platform for investigations of the spin-orbit proximity effects with possible applications in gate-tunable active spintronic devices for spin manipulation and spin-charge conversion. However, the spin transport phe-



nomena and the nature of proximity-induced SOC in these systems have not been previously explored experimentally, which motivated the investigations performed in this thesis.



## 4 Graphene-based spintronic devices

The pioneering studies of spin transport in graphene revealed its great potential for applications in spintronics because it exhibits long spin lifetimes and spin diffusion lengths. Most of the initial works have been done with high-quality exfoliated graphene samples that exhibit high carrier mobility and good spin transport. However, mechanical exfoliation is not a scalable fabrication technique, and for perspectives of industrialization it is important to investigate graphene produced using a scalable method. In this chapter, we study the spintronic properties of chemical vapor deposited (CVD) graphene (paper I) and move towards more complicated channel geometries (paper II) for the realization of prototype spin logic gates.

### 4.1 Graphene for robust spin interconnects

CVD graphene allows for scalable fabrication of spintronic devices. However, compared to exfoliated samples that are single-crystalline and of high quality, CVD growth can naturally lead to the formation of grain boundaries, multilayer graphene patches, and folds. Therefore, it is important to investigate how such inhomogeneities affect the spin transport properties of graphene. We address these questions in paper I, where we describe the fabrication and characterization of charge and spin transport properties of devices containing single-layer, bilayer, and trilayer graphene patches, as well as layer boundaries and folds.

#### 4.1.1 Spin transport across CVD graphene layer boundaries

Electron beam lithography was used to pattern a multilayer CVD graphene patch into a stripe with a nonuniform number of layers (Figure 4.1a). Ferromagnetic tunnel contacts ( $\text{Co}/\text{TiO}_2$ ) were evaporated onto the stripe to access individual continuous spin transport channels comprised of one, two, or three layers of graphene, as well as channels containing boundaries between those areas (Figure 4.1b). Nonmagnetic contacts made of  $\text{Au}/\text{Ti}$  were deposited close to the edges of the stripe to be used as reference electrodes for spin voltage measurements. The measurements were performed at room temperature  $T = 300$  K.

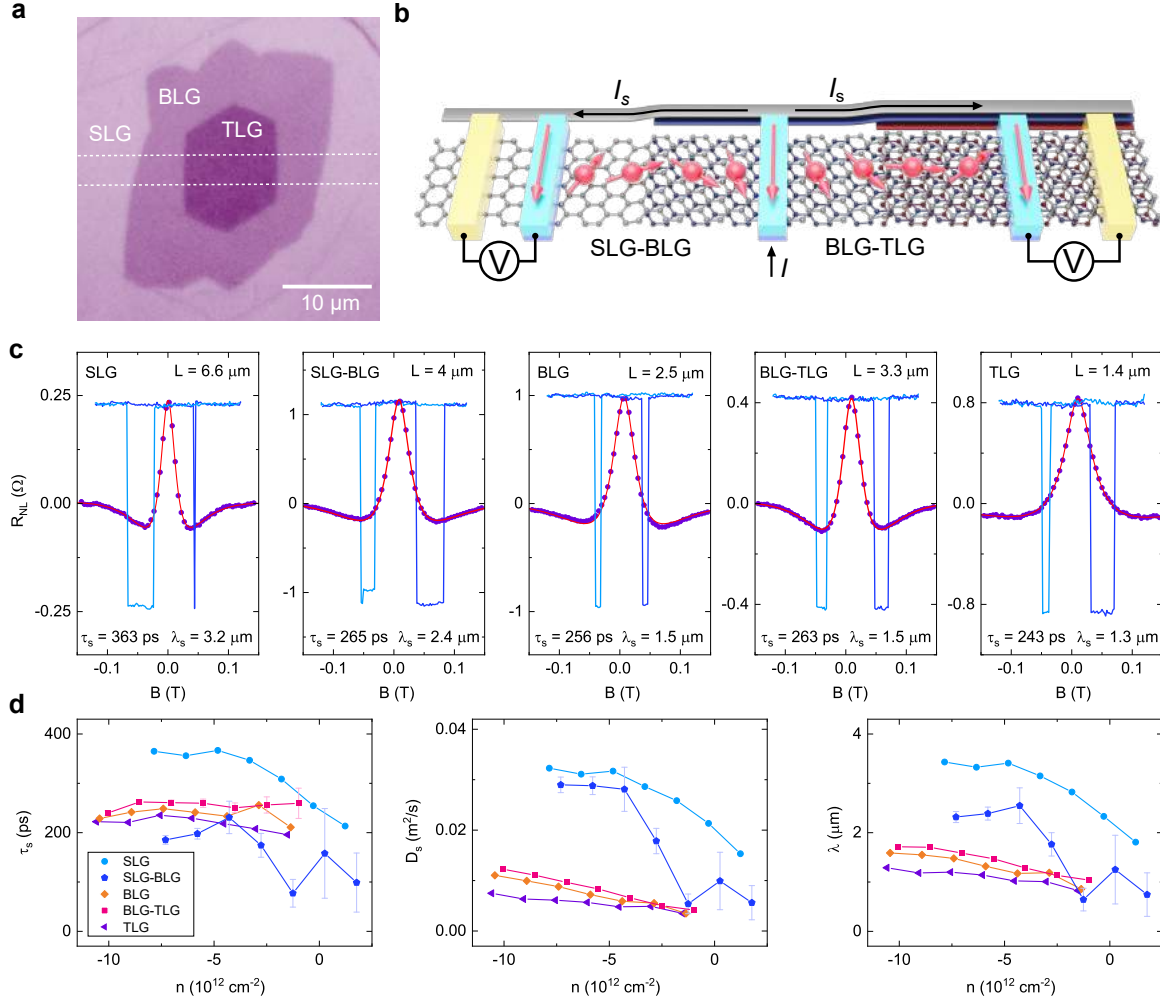


**Figure 4.1:** Spin transport in multilayer graphene channels and across layer boundaries. **a**, An optical microscope picture of a multilayer CVD graphene patch. The area used for the device fabrication is outlined in white. **b**, A schematic of the device with spin transport across layer boundaries. **c**, Spin valve and Hanle spin precession measurements obtained in single-layer (SLG), bilayer (BLG), and trilayer (TLG) channels, as well as single-bilayer (SLG-BLG) and bilayer-trilayer (BLG-TLG) boundaries. Channel length  $L$  is denoted for each panel. **d**, Carrier density dependence of the extracted spin spin lifetime  $\tau_s$ , spin diffusion coefficient  $D_s$ , and spin diffusion length  $\lambda_s$ .

The spin transport in all channels was characterized using the spin valve and Hanle spin precession experiments as shown in Figure 4.1c. The SV data was obtained with the in-plane magnetic field sweep, and the Hanle curves were measured with the out-of-plane field. Red lines show fits of the spin precession data to the Hanle equation (2.11), and the extracted spin transport parameters are shown. The obtained results show robust spin signals in all channels, proving that the defects under study do not compromise the spin transport capability of large-area

CVD graphene. The extracted spin lifetimes  $\tau_s$ , except for the SLG, show little variation between different channels, indicating the uniformity of the devices and weak dependence on layer configuration. The SLG channel shows larger spin parameters, but, unlike all other channels which are placed in close vicinity, this data belongs to another graphene area on the same chip, which hinders a direct comparison.

Performing the spin transport measurements at gate voltages ranging from  $-80$  V to  $80$  V allowed to investigate the dependence of spin transport parameters on charge carrier density. The large initial hole doping, common for our graphene samples on  $\text{SiO}_2$ , restricted the accessible range of carrier concentration to mostly hole conduction. We observed a strong decrease of  $\tau_s$ ,  $D_s$ , and  $\lambda_s$  as the Fermi level in graphene is tuned towards the charge neutrality point in all channels (Figure 4.1d). This behavior is commonly seen for  $D_s$ , which also influences the spin lifetime due to the proportionality between  $\tau_s$  and  $D_s$  characteristic of the Elliot-Yafet spin relaxation mechanism that dominates spin lifetime near the charge neutrality point. In addition, effects of conductivity mismatch should be considered, which in our devices leads to the reduction of spin signal amplitude close to the Dirac point. The negative effects of the conductivity mismatch can be mediated by choosing the appropriate resistance of the electrical contacts. We use contact resistances in the range of  $2 \text{ k}\Omega$  to  $12 \text{ k}\Omega$ , which exceeds the channel spin resistance given by  $R_s^{\text{gr}} = \frac{R_{\text{sq}}\lambda_s}{W_{\text{gr}}} \leq 1 \text{ k}\Omega$ , and suppresses the back-scattering of the injected spins into the FM. Our data also show evidence for the screening of the gate electric field in multilayer channels, as the spintronic parameters in them become less tunable with increasing thickness [187].

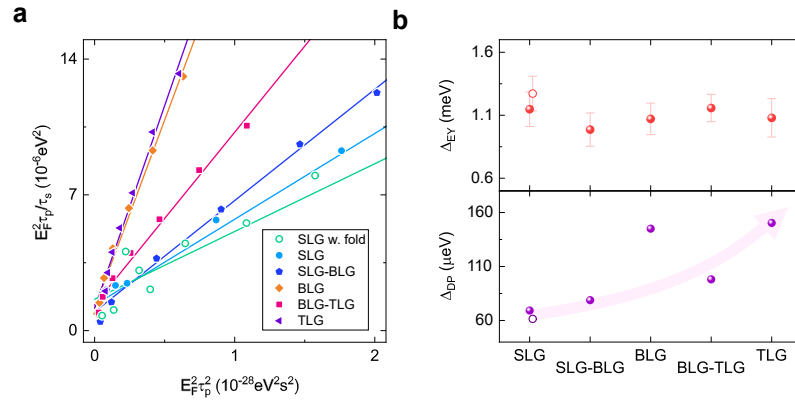


**Figure 4.2:** Spin relaxation mechanisms in inhomogeneous CVD graphene channels. **a**, Estimation of the contributions of spin scattering mechanisms in multilayer CVD graphene channels and their boundaries. **b**, The extracted SOC energy scale for the EY and DP mechanisms in different channels.

Spin relaxation in graphene is governed by the Elliott-Yafet (EY) and D'yakonov-Perel' (DP) spin scattering mechanisms. The EY mechanism assumes spin-flip

events during electron scattering, leading to the direct proportionality between spin lifetime  $\tau_s$  and momentum scattering time  $\tau_p$ ,  $\tau_{s,EY} = \left(\frac{E_F}{\Delta_{EY}}\right)^2 \tau_p$ , where  $E_F$  is the Fermi energy relative to the graphene Dirac point, and  $\Delta_{EY}$  is the EY SOC. The DP mechanism describes spin-flip scattering due to spin precession in effective magnetic fields between the scattering events, resulting in the spin lifetime being inversely proportional to the momentum scattering time  $\tau_{s,DP}^{-1} = 4 \left(\frac{\Delta_{DP}}{\hbar}\right)^2 \tau_p$ , where  $\Delta_{DP}$  is the effective SOC for the DP mechanism. To determine the dominant mode of spin relaxation, we assume that both mechanisms are present simultaneously, which leads to the total spin relaxation rate  $\tau_s^{-1} = (\tau_{s,EY}^{-1} + \tau_{s,DP}^{-1})^{-1}$ , which can be expressed as

$$E_F^2 \frac{\tau_p}{\tau_s} = \Delta_{EY}^2 + 4 \left(\frac{\Delta_{DP}}{\hbar}\right)^2 (E_F)^2 \tau_p^2. \quad (4.1)$$

By fitting the experimental data with eq. 4.1, we extracted the energy scale parameters  $\Delta_{EY}$  and  $\Delta_{DP}$  for different channels, as shown in Figures 4.2a,b. We observe that  $\Delta_{DP}$  increases for thicker channels whereas  $\Delta_{EY}$  does not show a strong trend with channel thickness. These results indicate an increased role of the DP mechanism in multilayer graphene, which may explain the observed reduction of  $\tau_s$  at large carrier densities in those channels.

### 4.1.2 Isotropic spin dynamics in inhomogeneous graphene channels

Spin lifetime anisotropy is an important characteristic of spin transport channels, characterizing their ability to transfer spins polarized in different directions. It is expressed as the ratio of relaxation times for spins polarized in and out of the graphene plane  $\xi = \frac{\tau_{\perp}}{\tau_{\parallel}}$ . To estimate the spin relaxation anisotropy ratio in our nonuniform graphene channels, we employ spin precession in oblique magnetic fields (Figure 4.3a) [148]. Applying the external magnetic field at different angles  $\beta$  between the contact magnetization and the out-of-plane direction leads to the dephasing of all spin components that are not parallel to the magnetic field, leaving the magnitude of the output signal to be defined solely by the remaining spin component (Figures 4.3b,c). For  $0 < \beta < 90$ , the remaining spin signal is influenced by both  $\tau_{\perp}$  and  $\tau_{\parallel}$ , allowing to calculate the anisotropy ratio. Such angle-dependent spin precession experiments were performed in SLG, BLG, and TLG channels and through their boundaries at several chosen carrier densities. The extracted anisotropy values  $\xi = 0.9 - 1.1$  show that room-temperature spin transport is mainly isotropic in all studied channels at varying carrier densities.

Similar values of  $\xi$  were also extracted from the spin precession measurements in the magnetic field aligned with the graphene channel  $B_x$ . In such geometry,

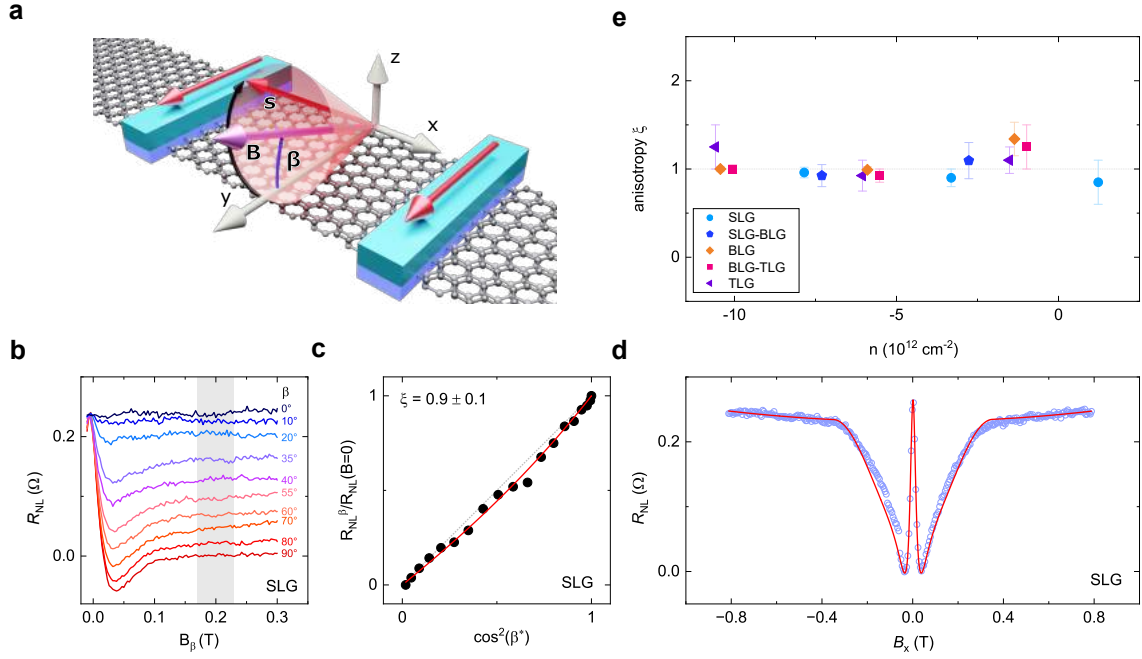


**Figure 4.3:** Measurements of spin lifetime anisotropy in graphene. **a**, A drawing of the spin precession in graphene with an oblique magnetic field applied at an angle  $\beta$  to the FM contact easy axis (along  $y$ ) in the  $yz$ -plane. **b**, Hanle spin precession curves obtained for different angles  $\beta$ . **c**, Normalized magnitude of the spin signal as a function of  $\cos^2(\beta)$  allows to visualize the anisotropy ratio. **d**, Spin signal obtained with the in-plane field  $B_x$ , showing the spin precession component at small fields and the rotation and saturation of the magnetization of FM electrodes at higher fields. **e**, The extracted anisotropy values in different channels for various levels of carrier doping.

spin precession is induced in the plane perpendicular to the field ( $yz$ -plane) and the resulting spin signal contains information about  $\tau_\perp$  and  $\tau_\parallel$ . A representative measurement obtained in the SLG channel is shown in Figure 4.3d. Such curves in different channels could be adequately fitted with anisotropy values in the range of  $0.9 - 1.1$ , in agreement with the oblique spin precession method. Figure 4.3e summarizes the values of  $\xi$  in different multilayer and nonuniform channels and at varying gate voltages. All values are close to unity, indicating that CVD graphene does not develop noticeable directional spin-orbit fields in the studied carrier density regimes. Such isotropic spin relaxation allows the large-area CVD graphene to be used as an efficient spin interconnect for arbitrarily polarized spins, proving its high potential for applications in the emerging spin-logic devices.

## 4.2 Spintronic circuit architectures for spin logic applications

Information processing using electron spin degree of freedom can become a cornerstone for next-generation fast and energy-efficient electronics. To realize such spin-based logic and memory technologies, spintronic circuits composed of multiple nanomagnetic elements interconnected with spin-coherent channels supporting efficient spin injection, detection, and long-distance spin transport must be developed. The studies of spin transport in graphene have identified it as a prime candidate to realize such robust spin interconnects for spin communication, however, so far they have been mostly restricted to a simple stripe channel geometry. Here, as presented in paper II, we make use of the excellent spin transport capabilities of large-area CVD graphene to fabricate more complex spin circuit geometries and study their spin transport and precession properties.

### 4.2.1 Spin transport in large-area multiterminal devices

Large-area CVD graphene was patterned into branched channels in the Y-junction and hexa-arm geometries to study spin transport and precession in multiterminal devices with non-collinear ferromagnetic electrodes. The devices were defined by electron beam lithography and oxygen plasma etching, and the ferromagnetic and non-magnetic contacts were deposited. Figures 4.4a,b show the Y-junction device and the utilized measurement configurations, where multiple arrangements of the injectors/detectors were used to perform spin valve and Hanle spin precession measurements in channels with  $L = 6.6, 20, 26.6 \mu\text{m}$  (Figure 4.4c). These measurements allowed us to extract the average spin polarization of the FM electrodes  $P \approx 7\%$  and the dependence of spin signal amplitude on the channel length at room temperature. By fitting the data with the expected exponential decay trend  $R_{\text{NL}} \propto e^{-L/\lambda_s}$ , we obtain the spin diffusion length of  $\lambda_s = 3.4 \mu\text{m}$ , which corresponds well with the values extracted from Hanle curves. By extrapolating the fit towards the noise level of our measurements, we could estimate the maximum channel length where the spin signal could be detected, which exceeded  $L = 34 \mu\text{m}$  (Figure 4.4d). This length depends not only on the intrinsic graphene properties but also on the extrinsic factors such as the amount of spins that can be injected from a FM and the noise level of the measurements, and conveys the maximum size of spintronic devices that can be achieved at the current stage of graphene technology development. This result proves the possibility to maintain the spin polarization in branched graphene channels over large distances, which is crucial for the design of logic circuits.

An inherent property of the electron spin is its directionality, and since the FM electrodes can inject/detect only the spins that are collinear with their magnetization, it can be used to realize weighted spin summation operations depending



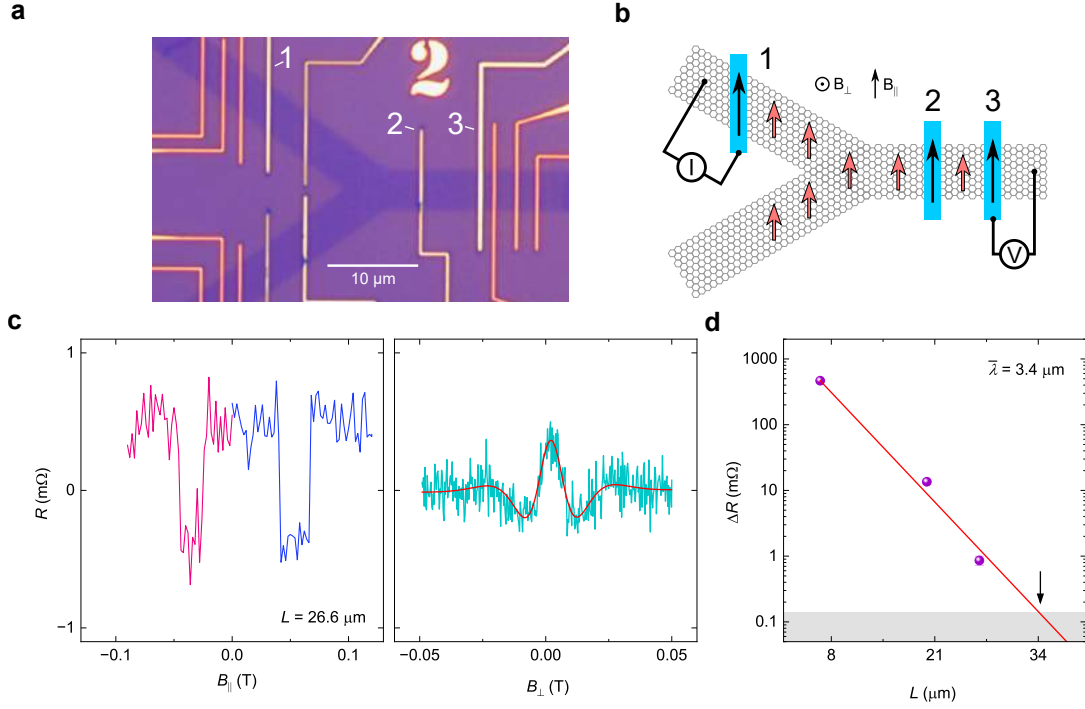


**Figure 4.4:** Long-distance spin transport in CVD graphene. **a**, An optical microscope picture of the Y-junction device. **b**, A schematic of the device with the nonlocal measurement geometry. **c**, Spin valve and Hanle spin precession signals obtained in a channel with length  $L = 26.6 \mu\text{m}$ . **d**, The dependence of the spin valve amplitude on the channel length. The fit shows the expected exponential decay with the relevant length scale parameter  $\lambda_s$ . Its intersection with the gray area, which depicts the noise level of the measurements, defines the maximum channel length for spin communication exceeding  $34 \mu\text{m}$ .

on the orientation of spin and magnetization. We explore these effects in the graphene channel of the hexa-arm device where spin injector and detector are placed at an angle of  $60^\circ$  (Figures 4.5a,b). Figure 4.5c shows the obtained Hanle spin precession signals for the "parallel" and "antiparallel" configurations of the electrode magnetization (since the electrodes are noncollinear, these terms refer to the components of their magnetizations along a common axis). As expected, contact non-collinearity makes the Hanle signals asymmetric, and they were deconvoluted into symmetric and antisymmetric components using

$$R_{\text{sym}} = \frac{R(B) + R(-B)}{2}, R_{\text{asym}} = \frac{R(B) - R(-B)}{2}, \quad (4.2)$$

as shown in Figure 4.5d. These components were fitted with general Hanle equations for the symmetric and antisymmetric parts:

$$R_{\text{sym}} = \frac{P_i P_d R_{\text{sq}} \tilde{\lambda}_s}{2W} \text{Re} \left( e^{-L/\tilde{\lambda}_s} \right), R_{\text{asym}} = \frac{P_i P_d R_{\text{sq}} \tilde{\lambda}_s}{2W} \text{Im} \left( e^{-L/\tilde{\lambda}_s} \right), \quad (4.3)$$

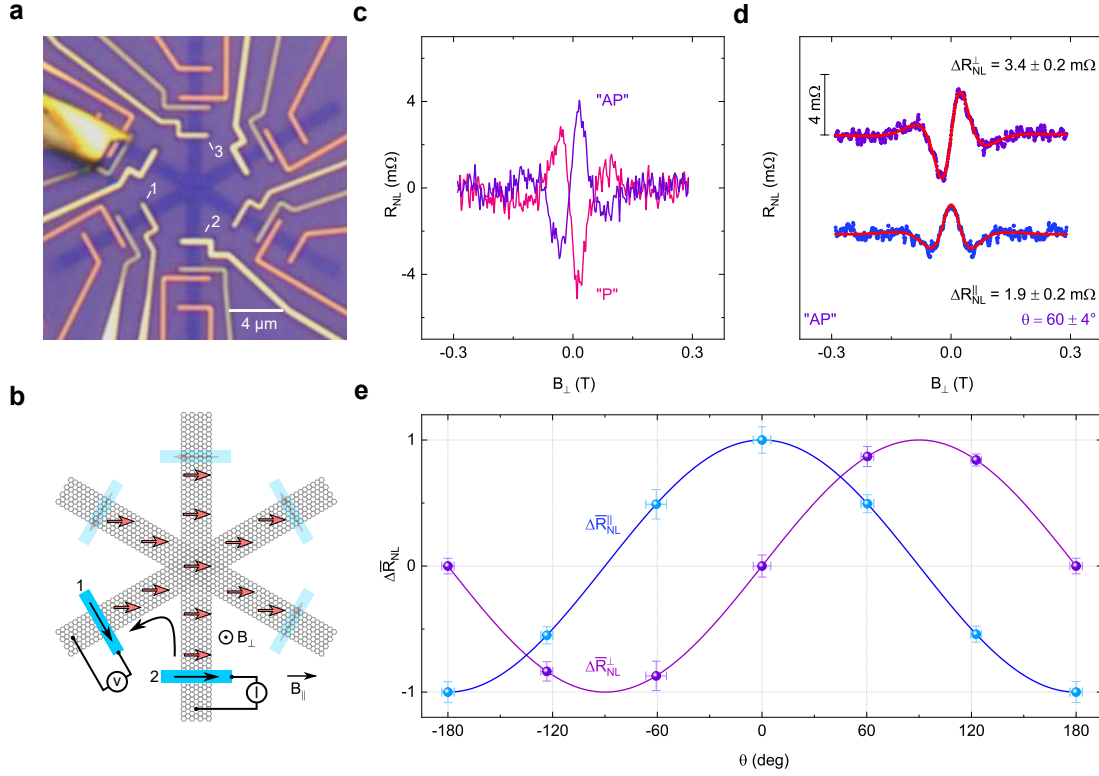


**Figure 4.5:** Spin transport and precession in multiterminal branched graphene channels. **a**, An optical microscope picture of the hexa-arm device. **b**, A schematic of the device with the measurement geometry. **c**, Asymmetric spin precession signals obtained in the hexa-arm device with the noncollinear arrangement of the injector and detector FM contacts. **d**, The Hanle signal for the "AP" configuration deconvoluted into its antisymmetric and symmetric components. **e**, Amplitudes of the symmetric and antisymmetric Hanle components as a function of the angle between injector/detector contacts. The points show the normalized experimental data.

where  $P_i$  and  $P_d$  are spin polarization values for the injector and detector contacts,  $R_{sq}$  is the graphene sheet resistance,  $L$  and  $W$  are the channel length and width, and  $\tilde{\lambda}_s$  is a complex renormalization of the spin relaxation length due to the effect of the magnetic field:

$$\tilde{\lambda}_s = \frac{\lambda_s}{\sqrt{1 + i\omega_B \tau_s}}, \quad (4.4)$$

where  $\tau_s$  and  $\lambda_s$  are the spin lifetime and spin diffusion length, and  $\omega_B = g\mu_B B/\hbar$  is the Larmor spin precession frequency with  $g$  being the gyromagnetic ratio,  $\mu_B$  being the Bohr magneton, and  $\hbar$  being the reduced Planck's constant. The extracted amplitudes of these components can be used to calculate the relative angle between the injector and detector contacts as  $\theta = \tan^{-1}(\Delta R^\perp/\Delta R^\parallel)$ . The extracted angle of  $\theta = 60 \pm 4^\circ$  corresponds very well with the geometrical design of the device. Figure 4.5e shows the normalized amplitudes of symmetric

and antisymmetric components of spin precession signals obtained in various injector/detector configurations, where the excellent correspondence between the geometrical device contact angles and values calculated from the measurements proves the applicability of this method for reconstructing the spin orientation, which can be applied to study the spin texture orientation of 2D materials placed in heterostructures with graphene. Finally, the isotropic spin diffusion in the branched channels was confirmed by measuring the spin polarization, injected at one contact, using several other FM contacts as detectors simultaneously. This demonstrates the possibility to split the signal into different device branches, and in the next chapter the inverse procedure was also confirmed, allowing to add up spin signals arriving from different branches. These results demonstrate the large-area CVD graphene as an attractive platform for large-scale integration and development of spin-logic and memory technologies.

### 4.2.2 Spin majority logic gate

Utilizing electron spin as a state variable for logic operations is a core tenet in spintronics, allowing to design beyond CMOS architectures and realize low-power, compact, and fast computing devices. In addition, it offers a possibility to combine the non-volatile memory with spin logic to achieve highly efficient integrated components for the information technology. Here, we explore prototype realizations of the spin addition operation and a spin majority logic gate in devices utilizing graphene as a spin interconnect and ferromagnetic electrodes as input and output elements.

Figure 4.6a shows an SEM picture of a spin majority gate fabricated using large-area CVD graphene contacted with tunnel ferromagnetic electrodes and nonmagnetic reference contacts. First, spin transport was investigated in each individual branch of the device, showing its robust operation via the spin valve and Hanle measurements (Figure 4.6b). These measurements were performed with a constant bias  $I = -200 \mu\text{A}$ , and the produced spin voltage is different for different channels because the length of the channel between injector B and the detector (output contact O) is shorter than that for injectors A and C, different branches have slight variations in their spin transport parameters, and the natural variations in the tunnel barrier uniformity affect the spin injection efficiency of each electrode. The uniform doping across the device was confirmed with the back-gate dependent channel resistance measurements (Figure 4.6d). Notably, due to the effect of domain pinning, the switching fields of the ferromagnetic electrodes are not the same for the up- and down- field sweeps, which is likely the reason for SV signals being non-symmetric about zero field.

Spin summation was probed using a simultaneous injection of spin currents from different ferromagnetic terminals. This leads to the mixing of the spin densities in the channel, and the resulting total spin polarization can be detected as a

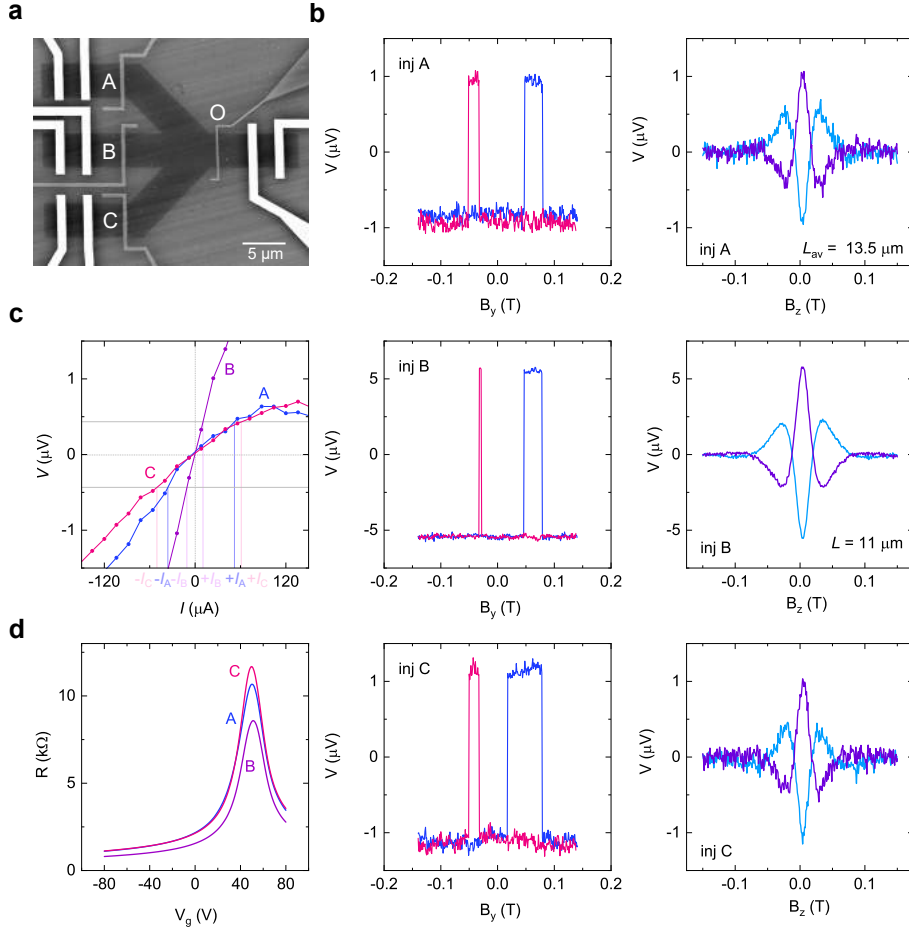


**Figure 4.6:** Spin majority gate device. **a**, An SEM picture of a spin majority gate with the CVD graphene channel and magnetic tunnel (Co/TiO<sub>2</sub>) and non-magnetic reference (Au/Ti) contacts. **b**, Spin valve and Hanle spin precession measurements for each injector contact. **c**, Bias dependence of the spin signal magnitude extracted from SV measurements for each injector. **d**, Gate dependence of the graphene resistance in each channel shows uniform device doping.

spin voltage. Figure 4.7 shows the spin valve signals obtained separately in two different branches of the device, and a resulting spin valve signal with both inputs working at the same time. The magnitude of the output spin valve in this case represents the sum of the spin signals from both inputs, demonstrating a linear spin mixing regime.

Besides switching the injector states by the magnetic field, the polarity of injected spins can be alternatively controlled by the application of positive or negative bias currents to the injectors. In this method, the magnetization of all contacts remains fixed, whereas the sign of the bias current determines whether the contacts work in the spin injection or spin extraction regimes. However, it must be taken into account that the tunnel ferromagnetic electrodes can have nonlinear dependence of spin injection/extraction efficiency on the bias current,

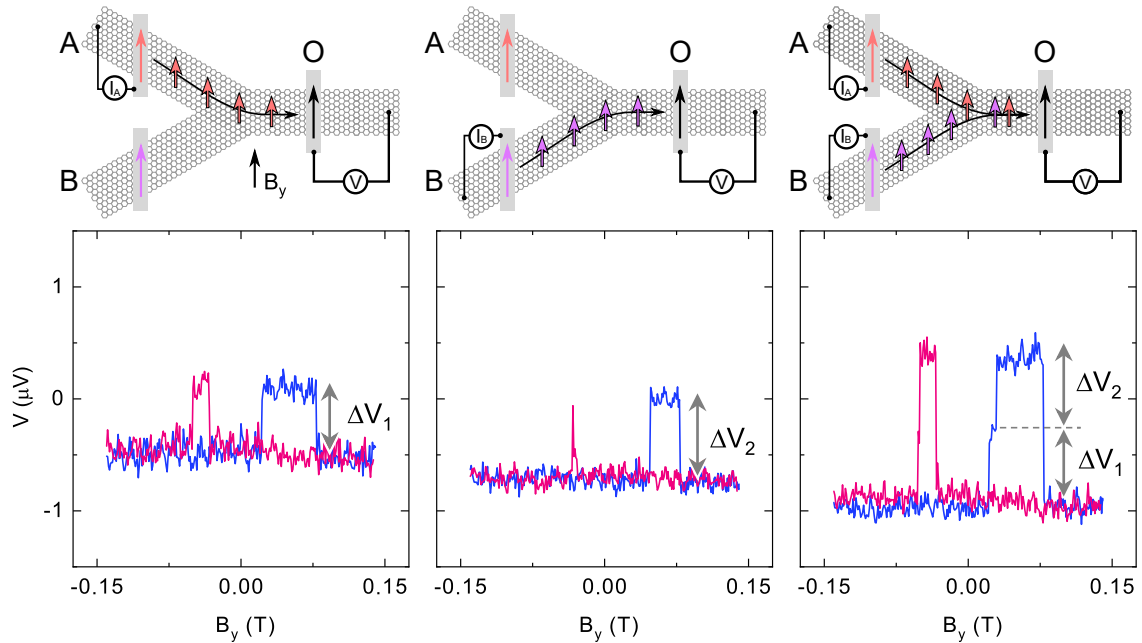


**Figure 4.7:** Spin addition operation. The spin valve signal obtained with two active injectors shows a magnitude representing the sum of the spin voltages produced by each injector, demonstrating linear spin addition operation due to the mixing of injected spin densities in the graphene channel.

which is often observed in  $\text{TiO}_2/\text{Co}$  contacts and is commonly attributed to magnetic proximity effects and energy-dependent spin-resolved density of states at the Gr/FM interface [188]. The presence of such nonlinearity in our devices (Figure 4.6c) results in different values for the bias currents required to achieve the same value of the spin voltage at negative and positive sides, and it also limits the accessible spin voltage range since the bias dependence has a maximum at a certain positive  $I$  value. This necessitates the calibration of the bias values, which is performed by measuring the dependence of the spin signal magnitude on the bias current for each injector, and determining the values of positive and negative bias currents that produce the same magnitude of the spin voltage output (Figure 4.6c).

When using the bias current to control the state of each injector, we define the input state of "1" as the application of positive bias current leading to spin-up injection and the state of "0" as the application of the negative bias current leading to the spin-down injection (practically achieved by spin-up extraction). In this regime of the operation of the spin summation device, the different input states defined by bias currents (Figure 4.8c) result in the spin mixing and the output spin voltage as shown in Figure 4.8b. The output shows three stable states corresponding to the regimes where the two inputs inject both spin-up density, both spin-down density, or opposite spins. The lower panel in Figure 4.8b shows a corresponding measurement with the magnetization states of both injectors pre-

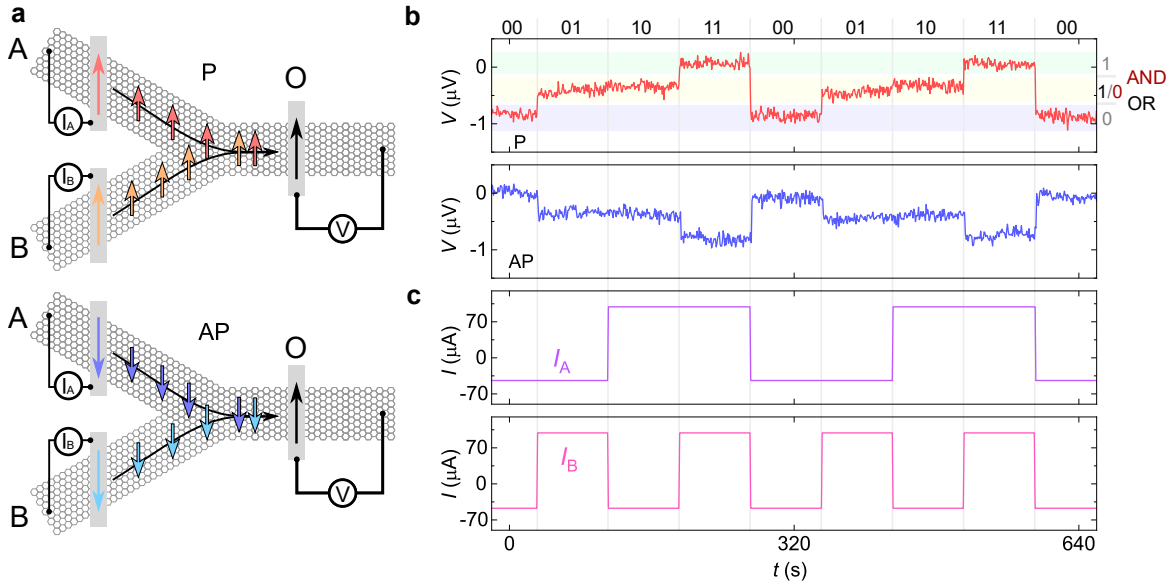


**Figure 4.8:** Spin summation with the bias current control. **a**, Schematics of spin addition with the parallel (P) and antiparallel (AP) alignment of magnetization of the injectors with respect to the detector. **b**, The output spin voltage at the detector as a function of time for the P and AP arrangements. **c**, The sequence of the applied bias currents to the two input contacts A and B.

liminarily set antiparallel (AP, see Figure 4.8a) to the detector, resulting in an inverted curve compared to the one shown in the upper panel. This inversion occurs because such magnetization change effectively inverts the polarity of injected spins for a given bias current sign for both injectors, which can be viewed alternatively as the logically negated output of the parallel configuration. With an addition of a comparator, such operation can represent an AND gate (if the output is considered "1" when the signal falls in the range of voltages marked by the light green area in Fig. 4.8b) or an OR gate (if the output is considered "1" whenever the signal leaves the range of voltages marked by the light blue area in Fig. 4.8b).

After establishing the spin summation operation, we investigated the spin majority gate operation using all three inputs of the device (Figure 4.9a). According to the truth table of the majority gate (Figure 4.9b), its output should be "1" if at least two of the three inputs are in the "1" state, and "0" otherwise. Interestingly, by fixing any input as "0", the output would be identical to the AND gate for the other inputs, and by fixing any input as "1", the output represents the OR gate, showing its re-programmable operation capability. Using the bias calibration as in the spin summation case, we inject a sequence of currents to the three inputs as shown in Figure 4.9d, and obtain an output signal depicted in Figure 4.9c. The output shows a stable switching between four levels corresponding to the cases where all three inputs inject spin-up or spin-down electrons, and where any two

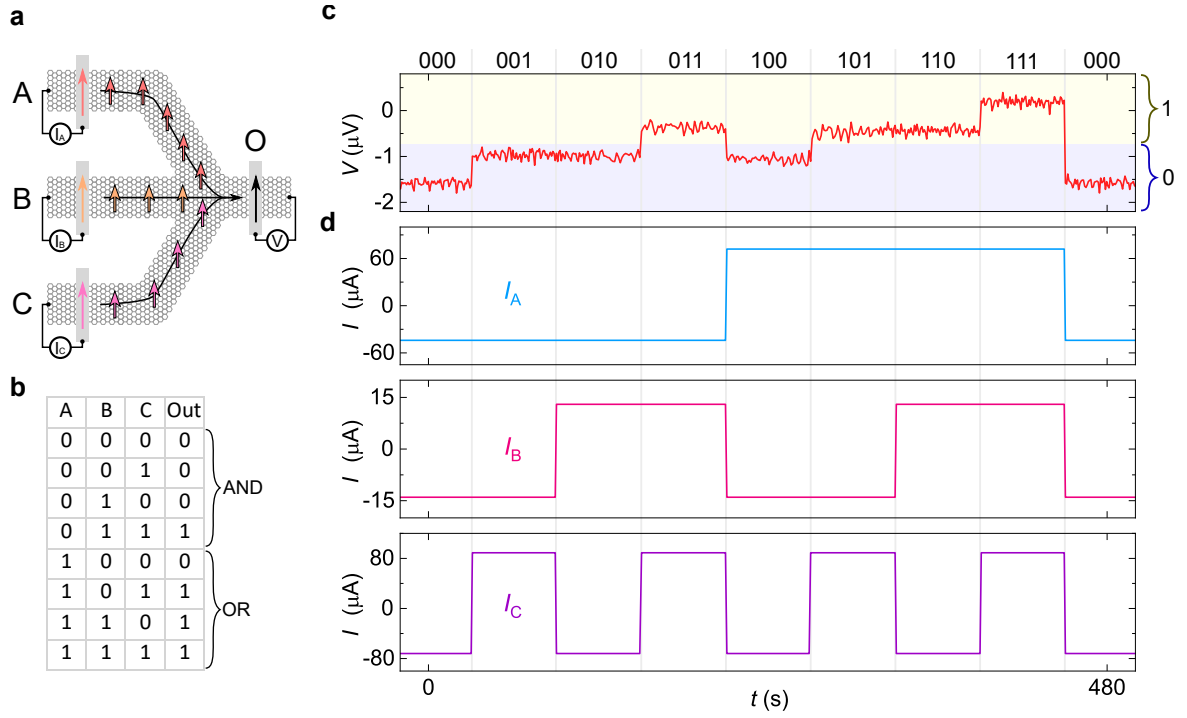


**Figure 4.9:** Spin majority gate operation. **a**, A schematic of the spin majority gate device with the measurement geometry. **b**, The truth table of the majority gate. **c**, The output spin voltage at the detector as a function of time. **d**, The sequence of the applied bias currents to the three input contacts A, B, and C.

injectors produce spin-up or spin-down density. The output can be labeled as logical "1" when the signal exceeds a threshold voltage value shown as a boundary between light yellow and light blue areas in Figure 4.9c, and logical "0" otherwise. We note that this threshold value should be, in principle, zero, but deviates from that due to the presence of the constant nonlocal spin-independent background that may appear due to the effects of charge current spreading in the channel [189–191]. This background voltage can be suppressed by optimizing the device design, or it can be offset to zero using an auxiliary voltage source [86].

Finally, we investigated the spin distribution in the graphene channel by modeling the Bloch spin diffusion equation (eq. 2.9) in the precise geometry of our device using the spin lifetime and spin diffusion length extracted from the Hanle spin precession measurements. Figure 4.10 shows the calculated steady-state solutions for different arrangements of the inputs: spin summation with only top and bottom injectors in the state "01", and spin majority gate in the states "011" and "010". The colors depict a logarithm of the spin density in arbitrary units, red for spin-up and blue for spin-down. The principle of operation is clearly visible as the spin density of the majority of the input states prevails at the output.

Our experiments prove the feasibility of spin addition in a multiterminal graphene device and allow us to demonstrate a prototype spin majority logic gate in graphene

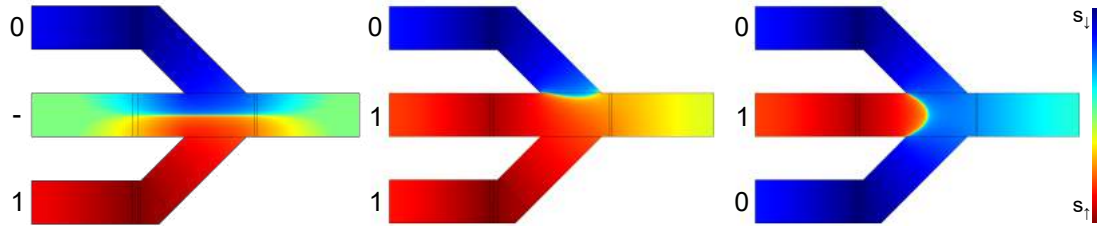


**Figure 4.10:** Numerical modeling of the spin majority gate. The Bloch spin diffusion equation was solved in COMSOL to obtain the spin density distribution for different combinations of the input states: spin summation state "01" (the middle input is unused), and spin majority gate with inputs "011" and "010". The colors represent the spin density in logarithmic scale in arbitrary units, red for spin-up and blue for spin-down.

where the output nonlocal spin voltage is shown to comply with the majority gate truth table.



# 5 Graphene-topological insulator heterostructures

Low intrinsic spin-orbit coupling in graphene gives rise to its excellent spin transport properties with long spin lifetimes and long spin diffusion lengths. However, this property also means that the active control over spin by means of the electric field cannot be achieved in pristine graphene, because a high SOC is needed to entangle an electron's spin with its motion. Several ways to artificially increase SOC in graphene have been suggested and studied over recent years [122–124, 129, 133]. These studies have demonstrated that the use of the spin-orbit proximity effect in van der Waals heterostructures is the most promising approach since it allows to preserve good charge transport quality of graphene while introducing novel spin functionalities into the hybrid system. These findings motivated further studies of heterostructures between graphene and transition metal dichalcogenides, two-dimensional ferromagnetic and antiferromagnetic materials, and novel topological phases of matter such as Dirac and Weyl semimetals, and topological insulators. In this chapter, we study the properties of TIs and emerging spin-orbit phenomena in their heterostructures with graphene. In paper III we experimentally detect the spin-momentum locking in surfaces of topological insulators and study how this phenomenon depends on the presence of multiple conducting channels through TI surface and bulk. Paper IV describes the formation of heterostructures between TIs and CVD graphene and presents experiments on spin transport through these hybrid systems, providing evidence for the increased SOC in graphene induced by the proximity effect. In paper V we make use of this increased SOC and the associated Rashba spin-splitting of the graphene bands to demonstrate the induced capability of spin-charge conversion due to the spin-galvanic effect in graphene.

## 5.1 Spin-momentum locking in topological insulators

Three-dimensional topological insulators represent a new class of materials that develop negative band gaps in the bulk due to their high intrinsic SOC. This leads to the formation of conductive surface states with massless Dirac fermions that exhibit peculiar spin-momentum locking (SML). Due to SML, the electron spins in TI surfaces are locked perpendicularly to their momentum, which makes any

charge current flowing in these states spin-polarized and thus allows to perform spin-charge interconversion via the Edelstein effect [47]. This phenomenon was experimentally observed by spin potentiometric measurements in prototypical TIs such as  $\text{Bi}_2\text{Se}_3$  [103, 104] and  $\text{Sb}_2\text{Te}_3$  [192]. However, these TI compounds are usually highly doped due to Se and Te vacancies so that their Fermi level crosses not only the surface states but also one of the bulk bands, which provides an additional spin-unpolarized conductive channel and obscures the physics of the surface states. To mitigate this issue and achieve compensated doping, quaternary TI compounds such as  $\text{Bi}_{1.5}\text{Sb}_{0.5}\text{Te}_{1.7}\text{Se}_{1.3}$  (BSTS) have been developed [102]. As detailed in paper III, we performed potentiometric measurements of SML in BSTS and observed strong dependence of the spin signal magnitude on temperature, which could be related to the varying contributions of the conduction through the TI bulk and surface states.

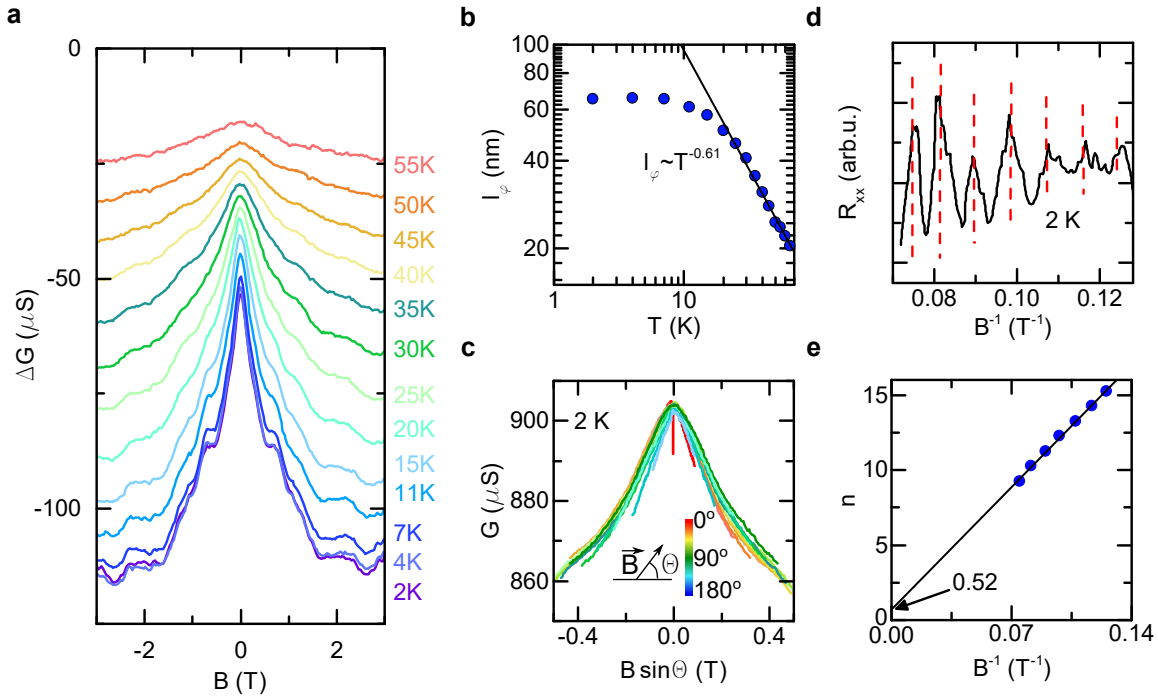


**Figure 5.1:** Magnetotransport in BSTS. **a**, Temperature dependence of the weak antilocalization (WAL) signal in a BSTS flake. **b**, Temperature dependence of the extracted phase coherence length. **c**, Angle dependence of the WAL signal plotted against the out-of-plane magnetic field component at 2 K. **d**, Shubnikov-de Haas oscillations in the longitudinal resistance of BSTS plotted against the inverse of magnetic field. **e**, The position of the oscillation's maxima extrapolates to  $\beta = 0.52$  when  $B \rightarrow \infty$ .

The flakes of BSTS were mechanically exfoliated onto a Si/SiO<sub>2</sub> substrate and the ferromagnetic tunnel contacts of TiO<sub>2</sub>/Co were defined by electron beam lithography and thin film deposition. Devices were initially characterized by elec-

trical transport and magnetotransport. Weak antilocalization was detected in BSTS at temperatures below 55 K, reflecting the strong SOC in the TI (Figure 5.1a). The data were fitted with the Hikami-Larkin-Nagaoka model [193]:

$$\Delta\sigma(B_{\perp}) = \alpha \frac{e^2}{\pi h} \left[ \ln \frac{\hbar}{4e\ell_{\phi}^2 B_{\perp}} - \psi \left( \frac{1}{2} + \frac{\hbar}{4e\ell_{\phi}^2 B_{\perp}} \right) \right] \quad (5.1)$$

, where  $\psi$  represents the digamma function,  $\ell_{\phi}$  is the phase coherence length, and  $\alpha$  represents the dimensionality factor of the system. The temperature dependence of the extracted values of the phase coherence length  $\ell_{\phi} \propto T^{-0.61}$  above 10 K indicates the 2D system behavior with dominant phonon scattering ( $\ell_{\phi} \propto T^{-0.5}$ ). Performing WAL measurements for different angles of the applied magnetic field shows that the signal is produced only by the out-of-plane component of the magnetic field since, when plotted against that component, all data collapse onto a universal curve (Figure 5.1c). This indicates that the signal originates from a 2D system (surface) rather than a 3D one (bulk). In high magnetic fields, Shubnikov-de Haas oscillations were observed in the longitudinal resistance, providing evidence for the Berry phase of  $\varphi_B \approx \pi$ , as expected for the Dirac electrons in the topological surface states (Figures 5.1d,e). Furthermore, the 2D carrier concentration  $n_{2D} = 5.9 \times 10^{12} \text{ cm}^{-2}$  extracted from the frequency of the oscillations matches well with the total carrier density obtained from the Hall effect measurements. These observations provide clear evidence for surface-dominated transport at low temperatures.

Further evidence of the surface conduction at low temperatures is obtained from the temperature dependence of the sample resistance as shown in Figure 5.2a. With decreasing temperature the sample exhibits semiconducting behavior as its 4-terminal channel resistance increases, but at  $T \sim 90$  K resistance starts to drop, indicating a transition to a metallic state. This measurement shows that the bulk conduction is frozen out and the surface states dominate conductance in the temperature range  $T < 90$  K, whereas at  $T > 90$  K thermally excited carriers in the bulk bands of the TI create an additional spin-unpolarized conducting channel.

BSTS with dominant surface conduction is ideal to study the spin-momentum locking. Spin potentiometric measurements were performed by applying a bias current that locks the spin direction in the channel, and measuring the magnetoresistance between the magnetization of the ferromagnetic electrode and the spin polarization of the channel with a reference to another electrode outside of the current flow loop. Figure 5.2b shows the obtained SML signals, where the detected voltage changes between the two stable states corresponding to the parallel or antiparallel configuration of the electrode magnetization and the spin polarization in the channel. Correspondingly, inverting the sign of the applied bias current induces opposite polarization in the channel, which results in a reversed hysteresis loop of the SML signal (Figure 5.2b). The magnitude of the hysteresis loops was found to scale linearly with the bias current, conforming to the expected linear

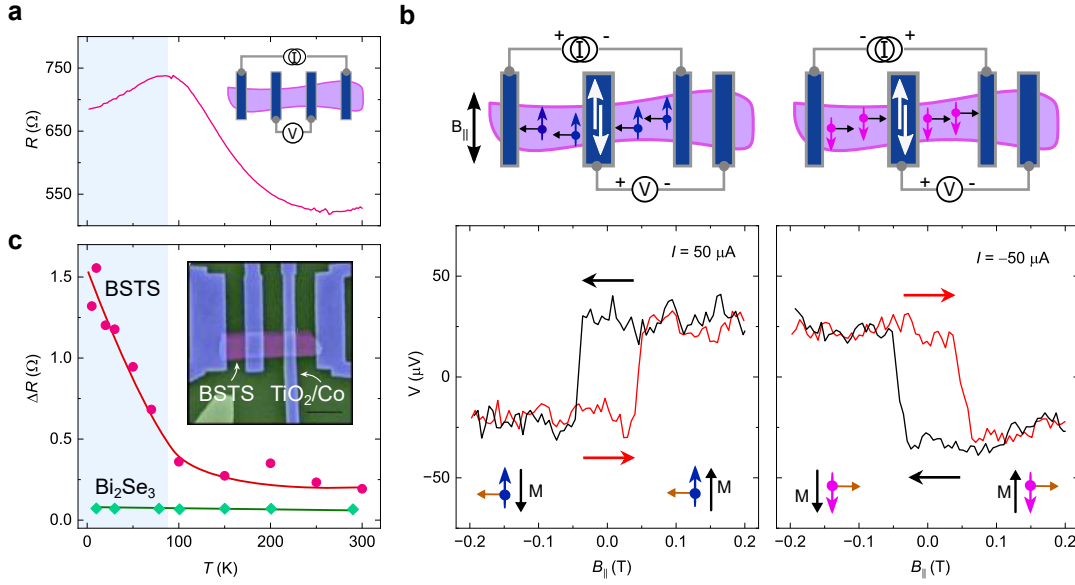


**Figure 5.2:** Spin-momentum locking in BSTS. **a**, Temperature dependence of BSTS resistance, showing a transition from semiconducting to metallic behavior as  $T$  is lowered below  $\sim 90$  K. **b**, Electrical measurements of SML in BSTS change sign for opposite bias polarities due to reversing the carrier momentum and thus the channel spin polarization. **c**, Temperature dependence of the SML signal magnitude in BSTS correlated with the channel's metal-semiconductor transition. For comparison, SML measurements in metallic  $\text{Bi}_2\text{Se}_3$  show weak temperature dependence [104]. The inset shows a colored SEM picture of the device. Scale bar 1 μm.

scaling behavior between the spin density and the current density.

The SML signal was measured as a function of temperature, and the switching amplitude was found to be approximately constant for  $100 \text{ K} < T < 300 \text{ K}$ , but strongly increasing upon further cooling  $2 \text{ K} < T < 100 \text{ K}$  (Figure 5.2c). This behavior is in stark contrast with the trend observed in highly-doped TIs such as  $\text{Bi}_2\text{Se}_3$ , which show only weak temperature dependence, and smaller signal magnitudes [104]. A clear correlation in the temperature dependence of the channel resistance and the spin signal magnitude is evident from Figures 5.2a,c, showing that SML magnitude is large when the conductance is dominated by surface states ( $T < 100 \text{ K}$ ), whereas it drops to a lower level when surface and bulk conduction channels coexist ( $T > 100 \text{ K}$ ). To further characterize the system we employ a two-channel conduction model that considers thermally activated bulk carriers and surface-to-bulk scattering. The fraction of the current that flows through the surface states was found to change from nearly 100% at low temperature to about 30% at 100 K, above which it stays approximately constant up to 300 K. In addition, we extracted the current-induced surface spin polarization  $P_S \approx 0.4 - 0.6$ , which is almost constant over the full studied temperature range. These observations elucidate how the bulk conduction and surface-bulk scattering

affect the measured SML signal, which is nevertheless still observable up to room temperature, having promising applications for spintronic science and technology.

To correctly interpret the electrical measurements of SML, careful consideration of the alternative contributions to the signal must be performed. In particular, the stray Hall effect from the FM contacts, and the Rashba-Edelstein effect in the bulk of TI can mimic the SML signal. The stray magnetic fields along the vertical direction can induce an ordinary Hall effect, creating a transverse voltage that changes sign with the change in magnetization. This may affect the SML measurements performed in the transverse resistance geometry, where the edge of the FM contact is placed directly on top of the channel [103, 117]. In our experiments, we minimize this effect by designing the FM contacts to completely overlap with the channel, and thus the stray fields from their edges are not interfering with the measurements. In addition, such stray Hall effect is strongly dependent on carrier doping and changes sign for opposite carrier types, which is not the case for the spin signal originating from the TI surface states. Our measurements in a metallic p-type TI  $\text{Sb}_2\text{Te}_3$  yield the same polarity of the SML signal as in n-type BSTS and  $\text{Bi}_2\text{Se}_3$ , allowing to rule out the stray field contribution, in accordance with previous reports that also found the same sign of the SML signal in electron- and hole-doped regimes [103, 105, 192]. Due to band bending at the surface of TIs, they can develop two-dimensional electron gas (2DEG) that forms another conducting channel in addition to the surface states and bulk bands. Due to the strong SOC in the TI, this 2DEG is Rashba spin-split and can exhibit the Rashba-Edelstein effect. However, the sign of its spin polarization was predicted to be opposite of that for the surface states, and its contribution to the magnetoresistance signal was estimated to be smaller than that from the surface states due to the compensation between the two Fermi surfaces with opposite spin directions [103].

### 5.1.1 Detection of spin-momentum locking via spin precession

Spin precession is a unique fingerprint of a true spin-based signal, allowing to rule out spurious charge-based contributions and providing additional information regarding the orientation of spin polarization. However, spin-momentum locking in TIs does not allow to observe spin precession in its surface states, since the spin is fixed by the momentum of carriers. To resolve this issue, graphene can be introduced in a heterostructure with a TI to be used as a tool to observe spin precession, if the spin polarization induced by SML in surface states can be injected through their interface. The injected spin current can be subsequently detected in a nonlocal spin transport geometry, where the spins can also be subjected to spin precession.

To investigate this phenomenon, CVD graphene was patterned into stripes using electron beam lithography, and flakes of the topological insulator  $\text{Bi}_{1.5}\text{Sb}_{0.5}\text{Te}_{1.7}\text{Se}_{1.3}$

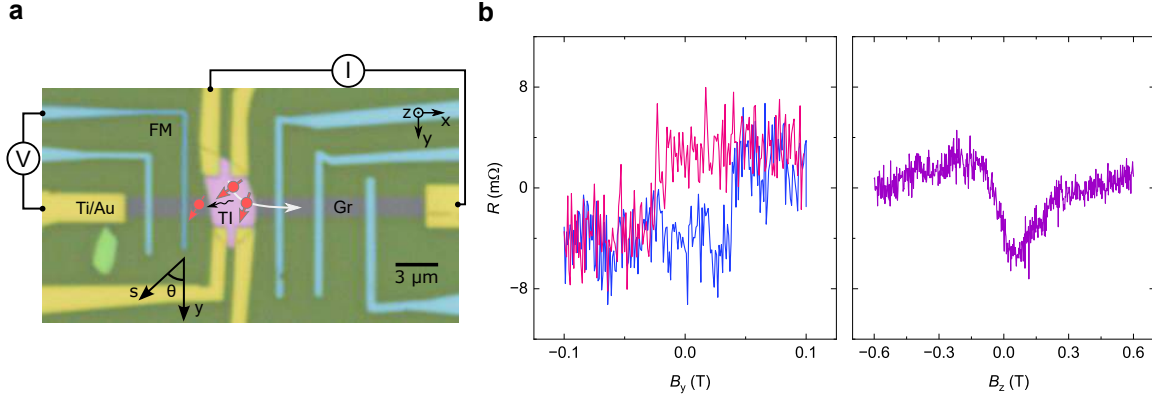


**Figure 5.3:** SML detection via spin precession. **a**, A colored optical microscopy picture of the Gr-BSTS heterostructure with a sketch of the nonlocal measurement geometry. **b**, SML detected in a switching experiment as well as in the Hanle spin precession measurement. The experiments were performed at room temperature.

(BSTS) were mechanically exfoliated on top of the stripes. The devices were contacted by ferromagnetic tunnel electrodes ( $\text{TiO}_2/\text{Co}$ ) and nonmagnetic reference contacts ( $\text{Ti}/\text{Au}$ ). Figure 5.3a shows a colored optical microscopy photograph of the device with a sketch of the measurement geometry. We apply the bias current between BSTS and graphene, which induces the charge flow through the TI bulk and surface states into the graphene and leads to the creation of spin accumulation in the channel. This spin accumulation is nonlocally detected by a FM electrode as spin voltage. Figure 5.3b shows the detected signal with the application of magnetic field along the  $y$ -direction  $B_y$ , which leads to switching of the detector magnetization, and with the magnetic field along the out-of-plane direction  $B_z$ , which induces spin precession. The observation of both the switching signal and Hanle spin precession indicates the presence of spin accumulation in the channel, proving the spin injection from the TI and ruling out spurious charge-based contributions. Note that the obtained Hanle signal is asymmetric, which indicates misalignment of the injected spin polarization from the magnetization direction of the detector (along  $y$ -axis). This misalignment can appear depending on the details of the current flow through the TI and its interface with graphene. Since in our measurement geometry we apply the electric current between the TI and graphene, electrons along the current path can have nonzero momentum components along  $z$ -axis in the TI bulk and along both  $x$ - and  $y$ -axes in the surface states, and thus the injected spin can be polarized at an arbitrary angle in the  $xy$ -plane. By splitting the spin precession data into symmetric and antisymmetric components following the approach described in section 4.2.1, we extract the angle of spin polarization of  $\theta = 52^\circ$  away from the  $y$ -axis, as shown in Figure 5.3a.

This study shows that the intimate coupling between a 3D TI and graphene

allows for exploiting the SOC-induced spin-momentum locking for injecting spin-polarized currents into the adjacent graphene layer, providing intriguing prospects for the development of all-electric spintronics. The use of nonmagnetic materials for spin injection and detection can be advantageous since it allows to circumvent the problems arising due to the roughness of scaled ferromagnetic interfaces and the associated parasitic effects from their stray fields [194].

## 5.2 Proximity-induced spin-orbit coupling in graphene-topological insulator heterostructures

Both graphene and topological insulators exhibit linear energy band spectra hosting massless two-dimensional chiral Dirac fermions, however, these materials possess strikingly different strengths of spin-orbit coupling. Thus, combining Gr and TIs in van der Waals heterostructures provides an attractive platform for investigating spin manipulation possibilities, exotic topological states, and emerging proximity-induced SOC effects that have no equivalent in the individual materials. Theoretical studies have predicted that the graphene in such heterostructures inherits an increased SOC from the TI, develops a band gap, and acquires a unique spin texture [170, 177]. Here, we investigate the nature of the proximity effect in graphene-TI heterostructures via spin transport measurements and obtain the value of the SOC strength in proximitized graphene nearly an order of magnitude higher than that in the pristine material (paper IV).

To fabricate the heterostructures, commercially available CVD graphene was patterned into stripes by photolithography and oxygen plasma etching, and the flakes of topological insulators  $\text{Bi}_2\text{Se}_3$  (BS) and  $\text{Bi}_{1.5}\text{Sb}_{0.5}\text{Te}_{1.7}\text{Se}_{1.3}$  (BSTS) were mechanically exfoliated on top of the stripes (Figure 5.4a). These different TIs were chosen in order to investigate the influence of the doping level since BS is metallic and highly n-doped with the Fermi level crossing the bulk conduction band, whereas BSTS is semiconducting n-type with the Fermi level lying in the bulk band gap. Initial characterization of the layer coupling in the heterostructures was performed by measuring the interface resistance through the Gr-TI vertical junctions. We obtain zero-bias interface resistance values in the range of  $R_{\text{Gr-TI}} = 15 - 30 \text{ k}\Omega$ , with a tunneling behavior in current-voltage characteristics. A higher degree of proximity interaction is expected for low interface resistance conditions, indicating the critical role of the fabrication steps needed to achieve high-quality interfaces. This can be ensured by cleaning the graphene from polymer residues via prolonged soaking in solvents and high-temperature annealing, whereas the formation of an oxide layer on the surface of TIs can be reduced by performing the exfoliation and heterostructure assembly in a glovebox with an inert atmosphere.

The spin transport experiments were performed in Gr-BS and Gr-BSTS heterostructures in the nonlocal measurement geometry (Figure 5.4b). In both systems, spin valve and Hanle spin precession signals were detected, with amplitudes  $\Delta R = 0.3 - 2.2 \text{ m}\Omega$  and the extracted spin lifetimes  $\tau_s = 7 - 22 \text{ ps}$  and spin diffusion lengths  $\lambda_s = 0.2 - 0.5 \mu\text{m}$  (Figure 5.4c). The obtained parameter values are strongly reduced compared to typical pristine Gr devices, which can exhibit  $\Delta R \sim 1 \Omega$ ,  $\tau_s \sim 300 \text{ ps}$ , and  $\lambda_s \sim 3 \mu\text{m}$ . Such a reduction in spin transport parameters can be an indication of the increased SOC induced in graphene via the proximity effect from TIs.



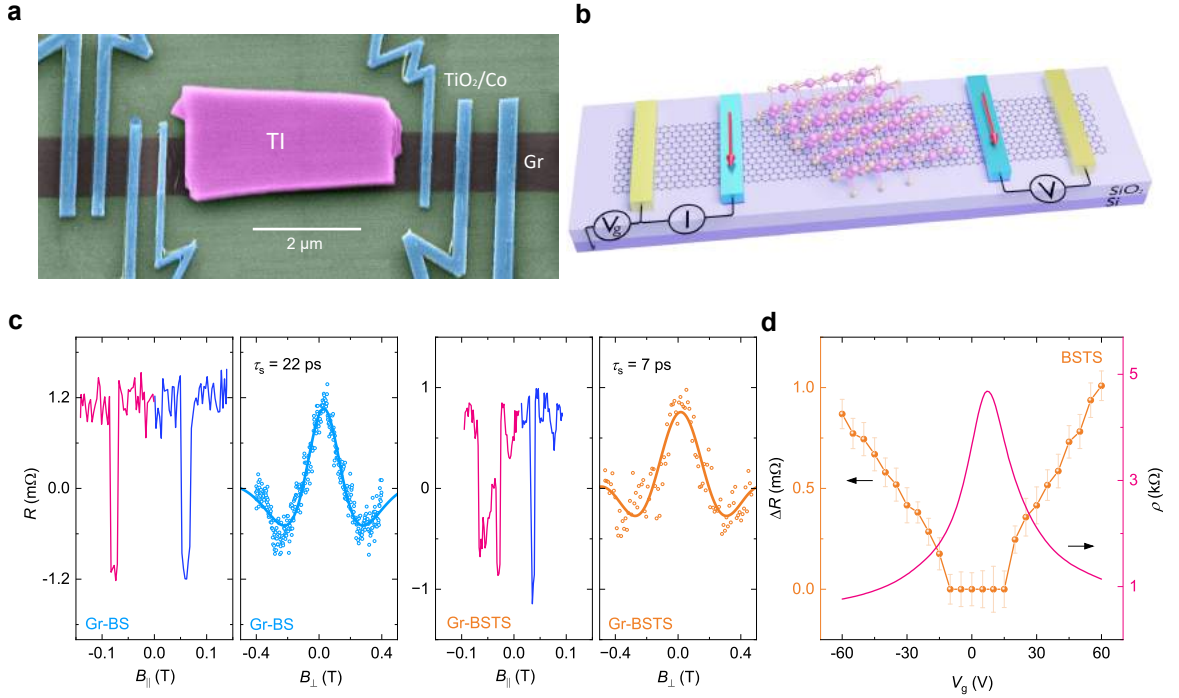


**Figure 5.4:** Spin transport in Gr-TI heterostructures. **a,b**, A colored SEM picture and a schematic of the heterostructure spintronic device with the nonlocal measurement configuration. **c**, Spin valve and Hanle spin precession data obtained in heterostructures of graphene with BS and BSTS. **d**, Gr-TI channel resistance (pink) and the spin signal magnitude (orange) as a function of the gate voltage. The channel resistance reaches a maximum at the charge neutrality point  $V_g \sim 7$  V, which correlates with the range of gate voltages where the spin signal vanishes.

The effect of the perpendicular electric field and carrier doping was investigated by performing the spin transport experiments at different values of the applied gate voltage. Due to the high carrier density in TIs and the screening of the electric field by the graphene, we expect that the gate mainly tunes the Fermi level in graphene, whereas its effect on TIs can be much smaller. Strong modulation of the spin signal magnitude by the gate voltage was observed in heterostructures of graphene with both BS and BSTS, where the signal was found to vanish in the range of gate voltages around the charge neutrality point of graphene (Figure 5.4d). Several mechanisms can contribute to this behavior, including the spin absorption by the TI, conductivity mismatch, and induced spin texture in graphene. It was shown that in heterostructures of graphene and semiconducting TMDs a Schottky barrier forms, leading to the tunability of the interface resistance by several orders of magnitude and enabling a gate control over the spin absorption [145, 146, 154]. However, the interface resistance in our Gr-TI heterostructures ( $R_{\text{Gr-TI}} \sim 15 \text{ k}\Omega$ ) does not exhibit large tunability by the electric field, and exceeds the graphene channel sheet resistivity ( $R_{\text{sq}} < 8 \text{ k}\Omega$ ) in the

whole range of the studied gate voltages. Thus, since the interface resistance may suppress spin absorption from graphene into the TI, and its weak gate tunability does not correspond with the large change in spin signal, this scenario is deemed unlikely. The conductivity mismatch due to the higher resistance of graphene compared to ferromagnetic metals can lead to the back-scattering of the injected spins into the FM contact, which is usually mediated by the addition of a tunneling barrier between the FM and graphene [61]. If the FM contact resistance  $R_I$  is larger than the spin resistance of graphene  $R_{\text{Gr}}^s = R_{\text{sq}} W / \lambda_s$ , the conductivity mismatch is suppressed. However, in the devices used for Figure 5.4,  $R_I < 1 \text{ k}\Omega$  is smaller than  $R_{\text{Gr}}^s \sim 5 \text{ k}\Omega$  and the conductivity mismatch can contribute to the observed gate dependence of the spin signal.

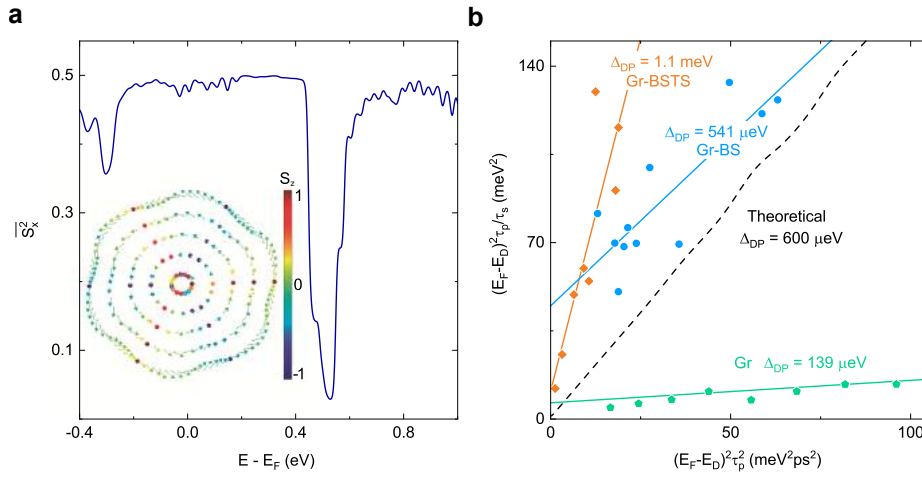


**Figure 5.5:** Spin-orbit coupling in Gr-TI heterostructures. **a**, Calculated average in-plane spin polarization in graphene as a function of energy. Inset: Helical spin texture induced in the graphene bands in heterostructures with TIs. Away from the Dirac point, the spin polarization remains primarily in-plane, whereas a large out-of-plane component appears close to the DP. **b**, Estimation of SOC strength in Gr (green), Gr-BS (blue), and Gr-BSTS (orange) devices using eq. 5.2.

In addition to the previously discussed mechanisms, the spin transport in Gr-TI heterostructures can also be affected by the unique spin texture introduced onto the graphene bands by the proximity effect. As predicted by theoretical calculations, the combination of various SOC terms present in commensurate Gr-TI HSs can produce a winding energy-dependent spin texture with varying out-of-plane spin component (inset of Figure 5.5a, see also Figure 3.15c). Figure 5.5a shows the calculated in-plane component of spin polarization of the graphene bands over the broad energy range, where a noticeable dip is observed near the graphene Dirac point as at these energies the spins are mostly directed out of the plane. Since our experiments are only sensitive to the in-plane spin component collinear to the FM contact magnetization, the behavior shown in Figure 5.5a

may be reflected in the gate-dependent spin signal trend (Figure 5.4d). To clarify the plausibility of this mechanism, measurements of the associated spin lifetime anisotropy can be performed in future studies.

Spin relaxation in proximitized graphene is mainly described by the Elliott-Yafet (EY) and D'yakonov-Perel' (DP) spin scattering mechanisms. Taking into account the expected helical spin texture induced in the graphene, the DP mechanism is described by  $\tau_{s,DP}^{-1} = 2 \left( \frac{\Delta_{DP}}{\hbar} \right)^2 \tau_p$ , where  $\tau_s$  is the spin lifetime,  $\tau_p$  is the momentum relaxation time, and  $\Delta_{DP}$  is the effective SOC for the DP mechanism. The EY mechanism leads to  $\tau_{s,EY} = \left( \frac{E_F - E_D}{\Delta_{EY}} \right)^2 \tau_p$ , where  $E_F - E_D$  is the Fermi energy relative to the graphene Dirac point, and  $\Delta_{EY}$  is the EY SOC[195]. The total spin relaxation rate  $\tau_s^{-1} = (\tau_{s,EY}^{-1} + \tau_{s,DP}^{-1})^{-1}$  can be written as

$$(E_F - E_D)^2 \frac{\tau_p}{\tau_s} = \Delta_{EY}^2 + 2 \left( \frac{\Delta_{DP}}{\hbar} \right)^2 (E_F - E_D)^2 \tau_p^2. \quad (5.2)$$

We extract  $\tau_s$  from the Hanle analysis and  $\tau_p$  from the gate dependence of the Gr-TI channel resistance, and fit the experimental data with eq. 5.2 as shown in Figure 5.5b. The extracted values of the effective SOC for EY and DP mechanisms are  $\Delta_{EY} = 6.7 \pm 0.8$  meV and  $\Delta_{DP} = 541 \pm 56$   $\mu$ eV for Gr-BS,  $\Delta_{EY} = 3.3 \pm 2$  meV and  $\Delta_{DP} = 1.1 \pm 0.1$  meV for Gr-BSTS,  $\Delta_{EY} = 2.5 \pm 0.4$  meV and  $\Delta_{DP} = 139 \pm 6$   $\mu$ eV for pristine graphene. The values of  $\Delta_{EY}$  are rather large in comparison with the intrinsic SOC strength of graphene ( $\sim 10$   $\mu$ eV), but are similar between the proximitized and pristine channels (see also Figure 4.2), and consistent with previous reports [51]. Thus, the origin of these  $\Delta_{EY}$  values is not related to the proximity effect, but is rather due to the spin scattering based on structural defects (e.g. ripples or folds) and contact-induced spin relaxation [196]. On the other hand, the values of  $\Delta_{DP}$  extracted from the Gr-TI heterostructures are significantly higher than those observed for the pristine graphene, indicating the presence of the increased proximity-induced SOC  $\sim 1$  meV of the D'yakonov-Perel' type.

### 5.3 Spin-galvanic effect in graphene-topological insulator heterostructures

Strong proximity-induced spin-orbit coupling achieved in graphene in van der Waals heterostructures with topological insulators leads to the formation of a helical spin texture. This allows the proximitized graphene to perform spin-charge conversion via the spin-galvanic effect, also known as the inverse Rashba-Edelstein effect, which describes the conversion of non-equilibrium spin density into a transverse charge current. Here, as presented in paper V, we investigate spin-charge conversion in Gr-TI heterostructures at room temperature, and obtain strong evidence of gate-tunable SGE in various device geometries through magnetization rotation, spin switch, and spin precession experiments.

#### 5.3.1 SGE detection by magnetization rotation

Spin-charge conversion through the spin-galvanic effect depends on the relation between spin and momentum in the material's spin texture. In graphene proximitized by topological insulators, theoretical studies predict the formation of a complex spin texture with in-plane and out-of-plane spin components (see [180], [169], and paper IV). Here we consider the calculations for the case when the crystal lattices of graphene and TIs are misaligned, yielding the incommensurate stacking and the large unit cell condition which is deemed the most likely scenario to occur in our experiments since no intentional alignment was done during the fabrication process. In this case, the in-plane spins are winding akin to the Rashba spin texture, and, interestingly, they have the same orientation in the conduction and valence bands of graphene, unlike the winding spin texture in surface states of TIs which changes direction for opposite carrier types. The out-of-plane spin texture component in proximitized graphene is predicted to be large, but changes in sign for opposite carrier types as well as  $K$  and  $K'$  valleys. Thus, considering the in-plane spin component, the spin-galvanic effect is expected to yield charge current flowing perpendicularly to the spin orientation.

First experiments to detect SGE were performed in a conventional Hall bar device geometry where a flake of TI is placed on top of one of the crosses (Figure 5.6a). For these experiments we utilized a metallic p-type TI  $(\text{Bi}_{0.15}\text{Sb}_{0.85})_2\text{Te}_3$  because of the higher conversion efficiency predicted for hole-doped TIs [110]. The TI was exfoliated on large-area CVD graphene, which was subsequently patterned by electron beam lithography and oxygen plasma etching, and contacted with magnetic and nonmagnetic contacts. The spin-charge conversion is detected as the transverse charge voltage across the heterostructure (Figure 5.6b), which, according to the spin texture, can only be produced by the spins oriented along the  $x$ -direction. As the easy axis of FM electrodes coincides with their longest dimension, which in this case is along the  $y$ -axis, no signal is present at zero magnetic

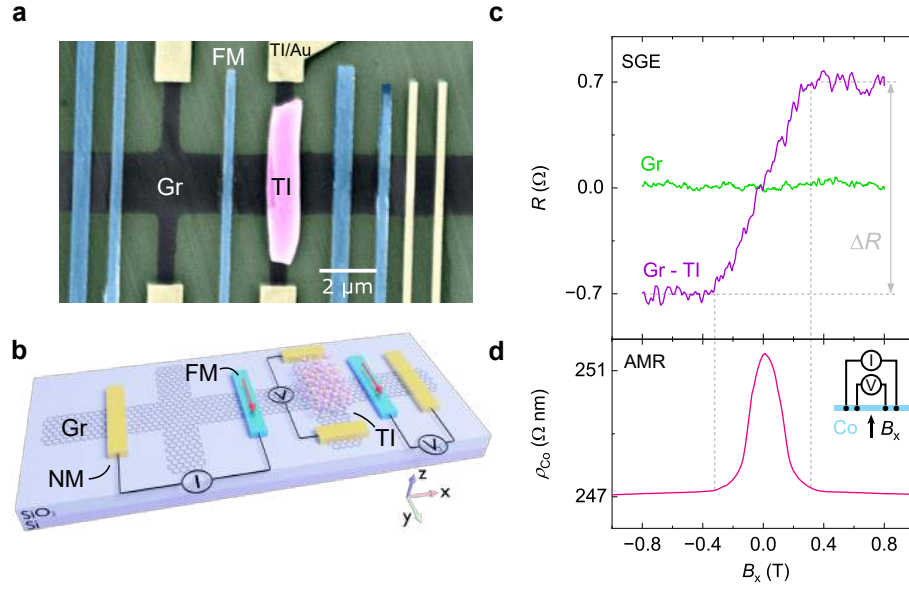


**Figure 5.6:** Spin-galvanic effect detected in magnetization rotation experiments. **a**, A colored SEM picture of the Gr-TI device. **b**, A schematic of the device and the measurement geometry. **c**, Spin-galvanic signal detected with the in-plane magnetic field  $B_x$  (purple) and the corresponding null signal obtained in the pristine graphene cross (green). **d**, Anisotropic magnetoresistance of a ferromagnetic contact. The saturation of SGE signal coincides with the saturation of the FM AMR since both signals follow the magnetization rotation of the injector electrode in the  $xy$ -plane.

field since no spins polarized along  $x$  are injected. An application of the external magnetic field along the  $x$ -axis causes the magnetization of the injector contact to rotate in the  $xy$ -plane towards the direction of the field, and fully aligns it in the  $x$ -direction when the field exceeds the saturation value  $B_{\text{sat}} \approx 0.35$  T. This results in a characteristic spin-galvanic signal shape with two stable voltage levels for the cases where spins along  $x$  and  $-x$  are injected at fields  $|B| > B_{\text{sat}}$ , and a linear trend at smaller fields (Figure 5.6c). The value of the saturation field  $B_{\text{sat}}$  corresponds well with the saturation point of the anisotropic magnetoresistance measurements performed on a similar cobalt FM electrode (Figure 5.6d).

The detected signal complies with the expected behavior of SGE, however, a similar lineshape can be obtained due to the ordinary Hall effect induced by the stray magnetic field of the injector FM contact, as it produces a sizable out-of-plane component of the magnetic field through the graphene channel when its magnetization is aligned in the  $x$ -direction. To rule out the contribution of this effect, we performed reference measurements in the pristine graphene cross of the Hall bar, where no signal was present in the device used for Figure 5.6c. However, in some other devices, an occurrence of non-zero signals in pristine graphene areas was detected, showing that the stray Hall effect can contribute to the observed signal, with a strong dependence on the particularities of the device

structure, current spreading, and stray field magnitude. To avoid such unwanted contributions to the signal, a detection mechanism that can be unambiguously linked to spin transport is desirable. For this, the unique features of the Hanle spin precession signal can serve as a fingerprint of spin-based operation, ruling out the spurious charge-based contributions. Spin precession signal was expected with the application of an out-of-plane magnetic field  $B_z$ , however, in devices similar to the one shown in Figure 5.6a, the transverse signals with  $B_z$  have a very large background, most likely originating due to the nonlocal ordinary Hall effect, which did not allow to clearly distinguish Hanle signals.

### 5.3.2 SGE detection by spin-switch and spin precession

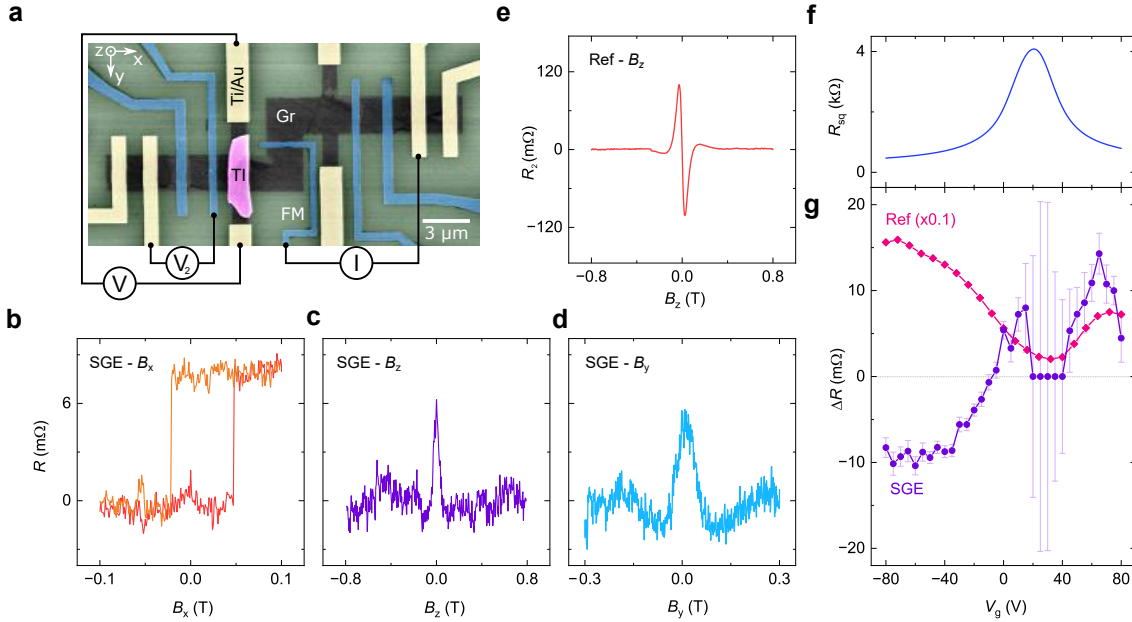


**Figure 5.7:** Spin-galvanic effect detected in spin-switch and spin precession experiments. **a**, A colored SEM picture of the device and the measurement geometry. **b**, SGE detected in a spin-switch experiment with  $B_x$ . **c,d**, SGE detected in Hanle spin precession experiments with  $B_z$  and  $B_y$  respectively. **e**, Reference Hanle signal detected by a second FM. **f**, Gate dependence of the channel resistance shows the average charge neutrality point (CNP) at  $V_g = 20$  V. **g**, The amplitudes of the SGE signal and scaled reference Hanle signal as a function of the gate voltage. All the measurements were performed at room temperature.

To alleviate the need for high in-plane magnetic fields for the measurement of SGE, we designed a new device with a modified Hall bar geometry where the easy axis of the injector contact is placed along the  $x$ -direction (Figure 5.7a). This allows the detection of SGE in a more conclusive spin-switch measurement configuration, as the magnetic field in  $x$ -direction can switch the magnetization

of the injector FM contact sharply as opposed to the slow rotation when the easy axis is placed along the  $y$ -direction. Accordingly, the detected charge voltage across the Gr-TI heterostructure exhibits sharp switching between two stable levels corresponding to the injection of spins polarized along  $x$  and  $-x$  (Figure 5.7b). Importantly, we could confirm the spin nature of the signal with the observation of spin precession in  $B_z$  and  $B_y$ , as shown in Figures 5.7c,d. A reference signal was detected simultaneously using a separate ferromagnetic electrode, where an antisymmetric Hanle curve was observed due to the  $90^\circ$  angle between the magnetization directions of the injector and detector (Figure 5.7e). Both the SGE and reference spin precession data were fitted with the Hanle equation, yielding similar values of the spin lifetime  $\tau_s = 150 - 190$  ps and spin diffusion length  $\lambda_s = 2.5 - 3.5$   $\mu\text{m}$ , showing the high potential of Gr-TI heterostructure devices for non-magnetic creation/detection of spin polarization, as well as the characterization of spintronic properties in devices free from ferromagnets.

To investigate the tunability of the spin-galvanic signal by the perpendicular electric field, the measurements of SGE were performed as a function of the gate voltage. The average charge neutrality point in the graphene channel was found at  $V_{\text{CNP}} = 20$  V, as shown in Figure 5.7f. Figure 5.7g shows the magnitudes of the SGE spin precession signal and reference Hanle signal as a function of the back gate voltage. Whereas the reference signal does not exhibit a sign change, the SGE signal is found to be tunable not only in magnitude but also in sign, demonstrating a unique feature of the induced spin-charge conversion mechanism. Interestingly, the gate voltage at which the sign change occurs  $V_0 \approx -7$  V deviates from  $V_{\text{CNP}}$ , whereas the theory predicts that such sign change should occur at  $V_{\text{CNP}}$  due to the change in type of carriers. This discrepancy may originate from the inhomogeneous doping in the channel, where the spatial variations in the carrier density and electron-hole puddles may result in a different local doping in the Gr-TI region where the spin-charge conversion takes place. However, similar shifts between  $V_0$  and  $V_{\text{CNP}}$  were observed in all other measured devices, which can indicate the presence of additional spin-charge conversion contributions e.g. from the surface states of the TI and Rashba-split 2DEG at its interface. Still, due to the helicity of spin textures of the TI surface states and its high p-doping that reduces the field effect, none of these contributions is expected to exhibit a sign change, which rules SGE as the only mechanism that can yield such behavior in our devices.

In addition to the spin-charge conversion by SGE, reciprocal charge-spin conversion by the inverse spin-galvanic effect (ISGE) was also detected in the Gr-TI heterostructures. To perform these measurements, the current injection and voltage detection circuits were swapped, as shown in Figure 5.8a. Here, the bias is applied across the gr-TI heterostructure using two nonmagnetic electrodes, which leads to the creation of spin density according to ISGE (also known as the Rashba-Edelstein effect). The produced spin density diffuses through the graphene chan-



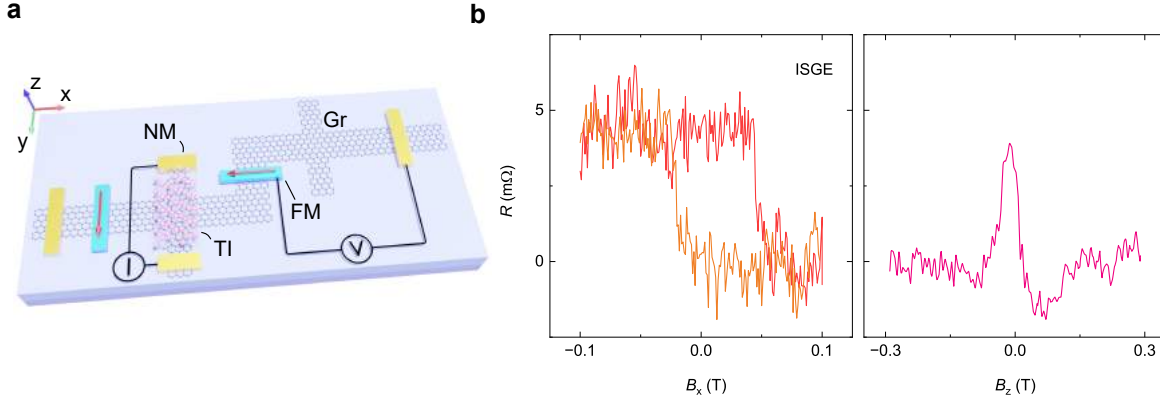


**Figure 5.8:** Charge-spin conversion via the inverse spin-galvanic effect. **a**, A schematic of the device and the measurement geometry for the inverse SGE (ISGE). **b**, ISGE detected via spin-switch and Hanle spin precession measurements with  $B_x$  and  $B_z$  field sweeps respectively.

nel as a spin current and creates the spin voltage detected by the FM electrode. Similarly to SHE, the signal produces clear signatures in both the spin-switch experiments with  $B_x$  and Hanle spin precession measurements in  $B_z$ , as shown in Figure 5.8b.

So far we discussed the proximity-induced spin-charge conversion for spins polarized in the graphene plane, since neither spin-switch measurements with  $B_x$  nor spin precession experiments with  $B_z$  can create out-of-plane spin polarization. On the other hand, an application of  $B_y$  can induce spin precession in the  $xz$ -plane, which allows to investigate the spin-charge conversion effects with the out-of-plane spins. Those can induce charge current through the proximity-induced inverse spin Hall effect in graphene, as well as through the spin-galvanic effect in case the spin texture has an out-of-plane component. Due to spin precession, the maximal out-of-plane spin component is expected at intermediate values of the field where an average rotation of spins by  $90^\circ$  is achieved, which implies that signals of this origin should be antisymmetric. However, no clear antisymmetric component was detected in spin-charge conversion measurements with  $B_y$  at any value of the gate voltage (Figure 5.7d). We note that this behavior is different from the reports on Gr-TMD systems, where amplitudes of proximity-induced SHE and SGE were found to be comparable in Gr-MoS<sub>2</sub> [159] and Gr-WS<sub>2</sub> [160], and from the Gr-WSe<sub>2</sub> [163] and Gr-BiO<sub>2</sub> [164] structures where only SHE without SGE was observed. This indicates that the in-plane Rashba SOC dominates over the out-of-plane valley-Zeeman SOC in Gr-TI heterostructures, reducing the efficiency of ISHE compared to SGE, and illustrates that the specifics of spin-orbit interaction terms present in graphene heterostructures with various materials lead to different accessible spin-charge conversion mechanisms. Besides ruling out the proximity-induced ISHE, the absence of the out-of-plane signal from SGE points



at the negligible net contribution from the  $s_z$  component of the induced spin texture in graphene. This may be due to the compensation of contributions of the K and K' valleys, which exhibit opposite signs of  $s_z$  [169].

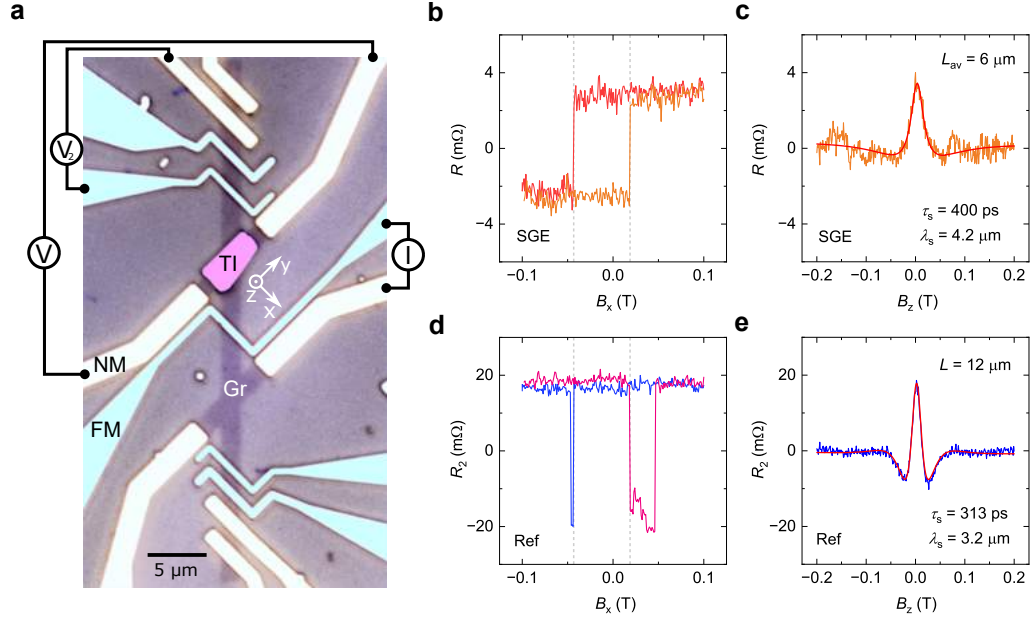


**Figure 5.9:** SGE detection by spin-switch and Hanle spin precession in an alternative device geometry. **a**, A colored optical microscopy picture of the device and the measurement geometry. **b,c**, SGE detected in spin-switch (with  $B_x$ ) and Hanle spin precession (with  $B_z$ ) experiments. **d,e**, Reference spin valve and Hanle signals detected with a second FM. All the measurements were performed at room temperature.

The detection of SGE in Gr-TI heterostructures was also confirmed in an alternative device design, where not just one, but all FM contacts were placed along the  $x$ -direction, whereas the detection of the charge current was still performed along the  $y$ -axis (Figure 5.9a). Figures 5.9b,c show the spin-galvanic signal detected across the Gr-TI heterostructure in the spin-switch and Hanle spin precession geometry, confirming the spin-charge conversion capability induced in the graphene. In addition, the reference signals were detected with a second FM, where both spin valve and Hanle spin precession were observed (Figure 5.9d,e). Coercive fields seen in the SGE and SV switchings coincide for one of the switches, proving that the SGE signal is caused by switchings of the injector ferromagnet only. Compared to the device shown in Figure 5.7a, here the spin precession curves for both the SGE and the reference detection scheme are symmetric, facilitating their direct comparison. However, the channel length for the reference measurement is uniform, which is not the case for the SGE channel, which may contribute to the difference in the extracted spin transport parameters as shown in Figures 5.9c,e.

The efficiency of the spin-charge conversion by SGE was characterized by a unitless parameter  $\alpha$ , which denotes a ratio between 2D charge current and 2D spin

current (assuming the spin polarization is converted to spin current by diffusion) [159]. We use the spin precession data to extract the efficiency values  $\alpha = 0.17\%$  for the device in Figure 5.7a, and  $\alpha = 0.1\%$  for the device in Figure 5.9a, which are comparable to the conversion efficiency seen in Gr-TMD heterostructures. For comparison with other systems, we can define  $\lambda_{\text{IEE}} = \alpha\lambda_s$  yielding  $\lambda_{\text{IEE}} = 6$  and  $3.2\text{ nm}$  for the respective devices. The obtained values compare favorably with those seen in heavy metals ( $0.1 - 0.4\text{ nm}$ ) [197], topological insulators ( $2.1\text{ nm}$ ) [109] and oxide interfaces ( $6.4\text{ nm}$ ) [198], but we note that this calculation yields higher bound since the utilized  $\lambda_s$  values were extracted from the Hanle curves whereas the true values for the proximitized graphene areas, which should be used for the estimation of  $\lambda_{\text{IEE}}$ , can be smaller due to the presence of the increased spin-orbit coupling.

## 6 Summary and Outlook

Spintronics aims at utilizing the electron spin degree of freedom as a state variable for developing future data storage and processing devices, promising faster operation and lower power consumption. Graphene (Gr) has emerged as a useful material for spintronic applications due to its low intrinsic spin-orbit coupling (SOC) and long spin diffusion length. This thesis investigates spin transport properties of large-area chemical vapor deposited (CVD) graphene in complex device architectures for emerging spin logic applications. In addition, it studies novel proximity effects in van der Waals heterostructures between graphene and topological insulators (TIs), where active spintronic functionalities based on spin-orbit interaction are demonstrated.

To realize scalable spintronic devices, large-area CVD graphene can be utilized to develop long-distance spin interconnects. Our observations of robust spin transport signals with a uniform spin lifetime in single layer, bilayer, and trilayer CVD graphene channels and across their layer boundaries have shown that these naturally occurring inhomogeneities in large-area graphene do not have a significant detrimental impact on its spin transport properties. In addition, using spin precession in oblique magnetic fields, we demonstrated predominantly isotropic spin relaxation with the anisotropy ratio  $\xi \sim 0.9 - 1.1$  in graphene layers and their boundaries at room temperature. Our analysis of spin relaxation pointed at the importance of both Elliott-Yafet and D'yakonov-Perel' mechanisms with an increasing role of the latter in multilayer channels. These findings demonstrated the excellent performance of large-area CVD graphene as a spin interconnect material with promising applications in emerging spin-based technologies and scalable spintronic circuits.

Next, we utilized the scalability of CVD graphene and its robust spin interconnect performance to study spin transport in multiterminal branched channels and realize prototype spin logic operations. The devices were found to support the spin transport and precession with channel lengths exceeding  $34\mu\text{m}$  at room temperature. Using the non-collinear arrangement of electrodes, the appearance of the symmetric and antisymmetric components in the Hanle spin precession signals was studied in detail. Furthermore, the linear spin addition operation was realized in graphene, allowing to achieve the first experimental demonstration of a prototype three-input spin majority gate operating with pure diffusive spin currents. These results could serve as the foundation for the design of complex 2D spintronic circuits, providing an attractive platform for further development of

spin-based logic and memory applications.

The low SOC in graphene governs its robust spin transport capabilities but prevents active control over spin current. This can be mitigated by incorporating high-SOC materials such as topological insulators into hybrid devices with graphene. For this purpose, we studied the spin and quantum transport properties of the topological insulator BSTS. The creation of spin polarization in TI surface states via spin-momentum locking was detected by electrical measurements over a broad temperature range, where a strong increase in spin signal at low temperatures  $T < 100$  K was correlated with the freeze-out of bulk conduction and dominance of surface transport. In addition, the charge-spin conversion signal was shown to persist up to room temperature, where it was also confirmed via spin precession measurements as the spin current could be injected from the TI into the graphene. These observations demonstrated TIs as a promising source of spin currents for spintronic devices.

The two-dimensional structure of graphene allows to combine it with other 2D materials into van der Waals heterostructures, which offer an attractive approach to design hybrid systems with sharp interfaces and tailored properties. The hybridization between graphene and TIs was predicted to give rise to a proximity effect, which increases SOC in graphene and endows it with a spin texture. Our spin transport experiments in such heterostructures confirmed the appearance of an enhanced SOC in graphene of  $\sim 1$  meV, an order of magnitude higher than that in pristine material. This evidence of an increased SOC indicated the potential of graphene to develop tunable spintronic functionalities in heterostructures with TIs.

An increased SOC and the unique spin texture induced in the graphene bands in proximity to a TI allow it to perform spin-charge conversion via the spin-galvanic effect (SGE). We developed various device geometries and utilized them to experimentally demonstrate SGE in Gr-TI heterostructures via complementary measurements in the magnetization rotation, spin-switch, and Hanle spin precession experiments. Importantly, the introduction of graphene mitigates the lack of field effect in strongly doped topological insulators, which allowed us to achieve strong electric field tunability of both amplitude and sign of the spin-galvanic signal. These results demonstrated the potential of Gr-TI heterostructures to be utilized as gate-tunable spin injection/detection elements free from ferromagnets, providing an efficient route for realizing all-electrical and gate-tunable spin-orbit technology.

The results obtained in this thesis demonstrate the high potential of graphene to be utilized as a spin interconnect material in spin-logic devices. The presented first demonstration of spin summation and spin majority gate encourages further development of the field towards the realization of proposed all-spin logic devices. In particular, the important milestone to achieve for spin-based logic devices will be the demonstration of certain functionality where the benefits of

---

reduced power consumption or more compact device footprint, in comparison to conventional transistor technology, outweigh the issues related to the need for signal amplification or additional circuitry for spin-charge conversion. The studies of the proximity effect in Gr-TI heterostructures can be utilized in the development of efficient spin-orbit torque magnetic memory devices (SOT-MRAM), where the incorporation of graphene between the TI and a (possibly 2D) magnetic material could decrease the current density required for electrical switching of magnetization. For the fundamental science, an attractive area for future graphene spintronics research can be the investigation of spin interactions in twisted graphene systems, where the formation of a moiré superlattice leads to an emergence of unconventional and gate-tunable correlated phases of matter [199]. In addition, the incorporation of the twisted graphene systems in heterostructures with other 2D materials can provide a unique platform for studies of proximity-induced spin-orbit and magnetic exchange couplings in highly correlated condensed matter systems.



# References

- [1] G. E. Moore, “Cramming more components onto integrated circuits”, *Electronics* **38**, 114 (1965).
- [2] I. Žutić, J. Fabian, and S Das Sarma, “Spintronics: Fundamentals and applications”, *Reviews of Modern Physics* **76**, 323–410 (2004).
- [3] H. Dery, H. Wu, B. Ciftcioglu, M. Huang, Y. Song, R. K. Kawakami, J. Shi, I. N. Krivorotov, D. A. Telesca, I. Žutić, and L. J. Sham, “Reconfigurable nanoelectronics using graphene based spintronic logic gates”, in *Spintronics IV*, Vol. 8100 (2011), 81000W.
- [4] B. Dieny et al., “Opportunities and challenges for spintronics in the micro-electronics industry”, *Nature Electronics* **3**, 446–459 (2020).
- [5] X. Lin, W. Yang, K. L. Wang, and W. Zhao, “Two-dimensional spintronics for low-power electronics”, *Nature Electronics* **2**, 274–283 (2019).
- [6] N. F. Mott and H. H. Wills, “The electrical conductivity of transition metals”, *Proceedings of the Royal Society of London. Series A - Mathematical and Physical Sciences* **153**, 699–717 (1936).
- [7] M. N. Baibich, J. M. Broto, A. Fert, F. N. Van Dau, F. Petroff, P. Eitenne, G. Creuzet, A. Friederich, and J. Chazelas, “Giant magnetoresistance of (001)Fe/(001)Cr magnetic superlattices”, *Physical Review Letters* **61**, 2472–2475 (1988).
- [8] G. Binasch, P. Grünberg, F. Saurenbach, and W. Zinn, “Enhanced magnetoresistance in layered magnetic structures with antiferromagnetic inter-layer exchange”, *Physical Review B* **39**, 4828–4830 (1989).
- [9] T. Miyazaki and N. Tezuka, “Spin polarized tunneling in ferromagnet/ insulator/ ferromagnet junctions”, *Journal of Magnetism and Magnetic Materials* **151**, 403–410 (1995).
- [10] J. S. Moodera, L. R. Kinder, T. M. Wong, and R. Meservey, “Large Magnetoresistance at Room Temperature in Ferromagnetic Thin Film Tunnel Junctions”, *Physical Review Letters* **74**, 3273–3276 (1995).
- [11] S. Datta and B. Das, “Electronic analog of the electro-optic modulator”, *Applied Physics Letters* **56**, 665–667 (1990).

- [12] F. J. Jedema, H. B. Heersche, A. T. Filip, J. J. A. Baselmans, and B. J. van Wees, “Electrical detection of spin precession in a metallic mesoscopic spin valve”, *Nature* **416**, 713–716 (2002).
- [13] Y. Fukuma, L. Wang, H. Idzuchi, S. Takahashi, S. Maekawa, and Y. Otani, “Giant enhancement of spin accumulation and long-distance spin precession in metallic lateral spin valves”, *Nature Materials* **10**, 527–531 (2011).
- [14] X. Lou, C. Adelmann, S. A. Crooker, E. S. Garlid, J. Zhang, K. S. M. Reddy, S. D. Flexner, C. J. Palmstrøm, and P. A. Crowell, “Electrical detection of spin transport in lateral ferromagnet-semiconductor devices”, *Nature Physics* **3**, 197–202 (2007).
- [15] S. P. Dash, S. Sharma, R. S. Patel, M. P. de Jong, and R. Jansen, “Electrical creation of spin polarization in silicon at room temperature”, *Nature* **462**, 491–494 (2009).
- [16] K. S. Novoselov, A. K. Geim, S. V. Morozov, D. Jiang, Y. Zhang, S. V. Dubonos, I. V. Grigorieva, and A. A. Firsov, “Electric field in atomically thin carbon films”, *Science* **306**, 666–669 (2004).
- [17] A. K. Geim and K. S. Novoselov, “The rise of graphene”, *Nature Materials* **6**, 183–191 (2007).
- [18] A. H. Castro Neto, F. Guinea, N. M. R. Peres, K. S. Novoselov, and A. K. Geim, “The electronic properties of graphene”, *Reviews of Modern Physics* **81**, 109–162 (2009).
- [19] N. Tombros, C. Jozsa, M. Popinciuc, H. T. Jonkman, and B. J. van Wees, “Electronic spin transport and spin precession in single graphene layers at room temperature”, *Nature* **448**, 571–574 (2007).
- [20] M. Drögeler, C. Franzen, F. Volmer, T. Pohlmann, L. Banszerus, M. Wolter, K. Watanabe, T. Taniguchi, C. Stampfer, and B. Beschoten, “Spin Lifetimes Exceeding 12 ns in Graphene Nonlocal Spin Valve Devices”, *Nano Letters* **16**, 3533–3539 (2016).
- [21] Z. M. Gebeyehu, S. Parui, J. F. Sierra, M. Timmermans, M. J. Esplandiu, S. Brems, C. Huyghebaert, K. Garello, M. V. Costache, and S. O. Valenzuela, “Spin communication over 30  $\mu\text{m}$  long channels of chemical vapor deposited graphene on  $\text{SiO}_2$ ”, *2D Materials* **6**, 034003 (2019).
- [22] K. S. Novoselov, D. Jiang, F. Schedin, T. J. Booth, V. V. Khotkevich, S. V. Morozov, and A. K. Geim, “Two-dimensional atomic crystals”, *Proceedings of the National Academy of Sciences of the United States of America* **102**, 10451–10453 (2005).
- [23] P. Miró, M. Audiffred, and T. Heine, “An atlas of two-dimensional materials”, *Chem. Soc. Rev.* **43**, 6537–6554 (2014).



- 
- [24] Z. Y. Zhu, Y. C. Cheng, and U. Schwingenschlögl, “Giant spin-orbit-induced spin splitting in two-dimensional transition-metal dichalcogenide semiconductors”, *Physical Review B* **84**, 153402 (2011).
  - [25] M. Z. Hasan and C. L. Kane, “Colloquium: Topological insulators”, *Reviews of Modern Physics* **82**, 3045–3067 (2010).
  - [26] A. K. Geim and I. V. Grigorieva, “Van der Waals heterostructures”, *Nature* **499**, 419–425 (2013).
  - [27] K. S. Novoselov, A. Mishchenko, A. Carvalho, and A. H. Castro Neto, “2D materials and van der Waals heterostructures”, *Science* **353**, aac9439 (2016).
  - [28] Y. Liu, N. O. Weiss, X. Duan, H.-C. Cheng, Y. Huang, and X. Duan, “Van der Waals heterostructures and devices”, *Nature Reviews Materials* **1**, 16042 (2016).
  - [29] N. F. Mott, “The resistance and thermoelectric properties of the transition metals”, *Proceedings of the Royal Society of London. Series A - Mathematical and Physical Sciences* **156**, 368–382 (1936).
  - [30] R. J. Soulen Jr., “Measuring the Spin Polarization of a Metal with a Superconducting Point Contact”, *Science* **282**, 85–88 (1998).
  - [31] M. Johnson and R. H. Silsbee, “Interfacial charge-spin coupling: Injection and detection of spin magnetization in metals”, *Physical Review Letters* **55**, 1790–1793 (1985).
  - [32] M. Julliere, “Tunneling between ferromagnetic films”, *Physics Letters A* **54**, 225–226 (1975).
  - [33] S. Ikeda, J. Hayakawa, Y. Ashizawa, Y. M. Lee, K. Miura, H. Hasegawa, M. Tsunoda, F. Matsukura, and H. Ohno, “Tunnel magnetoresistance of 604% at 300K by suppression of Ta diffusion in CoFeB/MgO/CoFeB pseudo-spin-valves annealed at high temperature”, *Applied Physics Letters* **93**, 082508 (2008).
  - [34] W. Han, R. K. Kawakami, M. Gmitra, and J. Fabian, “Graphene spintronics”, *Nature Nanotechnology* **9**, 794–807 (2014).
  - [35] D. Kochan, S. Irmer, M. Gmitra, and J. Fabian, “Resonant Scattering by Magnetic Impurities as a Model for Spin Relaxation in Bilayer Graphene”, *Physical Review Letters* **115**, 196601 (2015).
  - [36] S. Datta, *Electronic Transport in Mesoscopic Systems* (Cambridge University Press, 1995).
  - [37] J. Xia, F. Chen, J. Li, and N. Tao, “Measurement of the quantum capacitance of graphene”, *Nature Nanotechnology* **4**, 505–509 (2009).

- [38] K. Nagashio, T. Nishimura, and A. Toriumi, “Estimation of residual carrier density near the Dirac point in graphene through quantum capacitance measurement”, *Applied Physics Letters* **102**, 173507 (2013).
- [39] Y. Yin, Z. Cheng, L. Wang, K. Jin, and W. Wang, “Graphene, a material for high temperature devices - intrinsic carrier density, carrier drift velocity and lattice energy”, *Scientific Reports* **4**, 5758 (2015).
- [40] C. Józsa, T. Maassen, M. Popinciuc, P. J. Zomer, A. Veligura, H. T. Jonkman, and B. J. van Wees, “Linear scaling between momentum and spin scattering in graphene”, *Physical Review B* **80**, 241403 (2009).
- [41] J. H. Garcia, M. Vila, A. W. Cummings, and S. Roche, “Spin transport in graphene/transition metal dichalcogenide heterostructures”, *Chemical Society Reviews* **47**, 3359–3379 (2018).
- [42] F. Bloch, “Nuclear Induction”, *Physical Review* **70**, 460–474 (1946).
- [43] H. C. Torrey, “Bloch Equations with Diffusion Terms”, *Physical Review* **104**, 563–565 (1956).
- [44] H. Zhang, C.-X. X. Liu, X.-L. L. Qi, X. Dai, Z. Fang, and S.-C. C. Zhang, “Topological insulators in  $\text{Bi}_2\text{Se}_3$ ,  $\text{Bi}_2\text{Te}_3$  and  $\text{Sb}_2\text{Te}_3$  with a single Dirac cone on the surface”, *Nature Physics* **5**, 438–442 (2009).
- [45] C. L. Kane and E. J. Mele, “Quantum Spin Hall Effect in Graphene”, *Physical Review Letters* **95**, 226801 (2005).
- [46] C. L. Kane and E. J. Mele, “ $\text{Z}_2$  Topological Order and the Quantum Spin Hall Effect”, *Phys. Rev. Lett.* **95**, 146802 (2005).
- [47] V. M. Edelstein, “Spin polarization of conduction electrons induced by electric current in two-dimensional asymmetric electron systems”, *Solid State Communications* **73**, 233–235 (1990).
- [48] P. Gambardella and I. M. Miron, “Current-induced spin-orbit torques”, *Philosophical Transactions of the Royal Society A: Mathematical, Physical and Engineering Sciences* **369**, 3175–3197 (2011).
- [49] A Manchon, J Železný, I. M. Miron, T Jungwirth, J Sinova, A Thiaville, K Garello, and P Gambardella, “Current-induced spin-orbit torques in ferromagnetic and antiferromagnetic systems”, *Reviews of Modern Physics* **91**, 035004 (2019).
- [50] M. J. Allen, V. C. Tung, and R. B. Kaner, “Honeycomb carbon: A review of graphene”, *Chemical Reviews* **110**, 132–145 (2010).
- [51] P. J. Zomer, M. H. D. Guimarães, N Tombros, and B. J. van Wees, “Long-distance spin transport in high-mobility graphene on hexagonal boron nitride”, *Physical Review B* **86**, 161416 (2012).

- 
- [52] S. Roche and S. O. Valenzuela, “Graphene spintronics: Puzzling controversies and challenges for spin manipulation”, *Journal of Physics D: Applied Physics* **47**, 94011 (2014).
  - [53] L. Wang, I. Meric, P. Y. Huang, Q. Gao, Y. Gao, H. Tran, T. Taniguchi, K. Watanabe, L. M. Campos, D. A. Muller, J. Guo, P. Kim, J. Hone, K. L. Shepard, and C. R. Dean, “One-dimensional electrical contact to a two-dimensional material”, *Science* **342**, 614–617 (2013).
  - [54] P. J. Zomer, M. H. Guimarães, J. C. Brant, N. Tombros, and B. J. Van Wees, “Fast pick up technique for high quality heterostructures of bilayer graphene and hexagonal boron nitride”, *Applied Physics Letters* **105**, 013101 (2014).
  - [55] T. Maassen, J. J. Van Den Berg, N. Ijbema, F. Fromm, T. Seyller, R. Yakimova, and B. J. Van Wees, “Long spin relaxation times in wafer scale epitaxial graphene on SiC(0001)”, *Nano Letters* **12**, 1498–1502 (2012).
  - [56] B. Dlubak, M.-B. B. Martin, C. Deranlot, B. Servet, S. Xavier, R. Mattana, M. Sprinkle, C. Berger, W. A. De Heer, F. Petroff, A. Anane, P. Seneor, and A. Fert, “Highly efficient spin transport in epitaxial graphene on SiC”, *Nature Physics* **8**, 557 (2012).
  - [57] J. J. Van Den Berg, R. Yakimova, and B. J. Van Wees, “Spin transport in epitaxial graphene on the C-terminated (0001)-face of silicon carbide”, *Applied Physics Letters* **109**, 012402 (2016).
  - [58] L. Banszerus, M. Schmitz, S. Engels, J. Dauber, M. Oellers, F. Haupt, K. Watanabe, T. Taniguchi, B. Beschoten, and C. Stampfer, “Ultrahigh-mobility graphene devices from chemical vapor deposition on reusable copper”, *Science Advances* **1** (2015) 10.1126/sciadv.1500222.
  - [59] A. Avsar, T.-Y. Yang, S. Bae, J. Balakrishnan, F. Volmer, M. Jaiswal, Z. Yi, S. R. Ali, G. Güntherodt, B. H. Hong, B. Beschoten, and B. Özyilmaz, “Toward Wafer Scale Fabrication of Graphene Based Spin Valve Devices”, *Nano Letters* **11**, 2363–2368 (2011).
  - [60] M. V. Kamalakar, C. Groenveld, A. Dankert, and S. P. Dash, “Long distance spin communication in chemical vapour deposited graphene”, *Nature Communications* **6**, 6766 (2015).
  - [61] W. Han, K. Pi, K. M. McCreary, Y. Li, J. J. Wong, A. G. Swartz, and R. K. Kawakami, “Tunneling spin injection into single layer graphene”, *Physical Review Letters* **105**, 167202 (2010).
  - [62] M. V. Kamalakar, A. Dankert, P. J. Kelly, and S. P. Dash, “Inversion of Spin Signal and Spin Filtering in Ferromagnet|Hexagonal Boron Nitride-Graphene van der Waals Heterostructures”, *Scientific Reports* **6**, 21168 (2016).

- [63] T. Maassen, I. J. Vera-Marun, M. H. D. Guimarães, and B. J. van Wees, “Contact-induced spin relaxation in Hanle spin precession measurements”, *Physical Review B* **86**, 235408 (2012).
- [64] M. Gurram, S. Omar, and B. J. van Wees, “Bias induced up to 100% spin-injection and detection polarizations in ferromagnet / bilayer-hBN / graphene / hBN heterostructures”, *Nature Communications* **8**, 248 (2017).
- [65] W. Han, K. Pi, W. Bao, K. M. McCreary, Y. Li, W. H. Wang, C. N. Lau, and R. K. Kawakami, “Electrical detection of spin precession in single layer graphene spin valves with transparent contacts”, *Applied Physics Letters* **94**, 222109 (2009).
- [66] M. H. Guimarães, A. Veligura, P. J. Zomer, T. Maassen, I. J. Vera-Marun, N. Tombros, and B. J. Van Wees, “Spin transport in high-quality suspended graphene devices”, *Nano Letters* **12**, 3512–3517 (2012).
- [67] K. M. McCreary, A. G. Swartz, W. Han, J. Fabian, and R. K. Kawakami, “Magnetic Moment Formation in Graphene Detected by Scattering of Pure Spin Currents”, *Physical Review Letters* **109**, 186604 (2012).
- [68] T. Yamaguchi, S. Masubuchi, K. Iguchi, R. Moriya, and T. Machida, “Tunnel spin injection into graphene using  $\text{Al}_2\text{O}_3$  barrier grown by atomic layer deposition on functionalized graphene surface”, *Journal of Magnetism and Magnetic Materials* **324**, 849–852 (2012).
- [69] T. Yamaguchi, Y. Inoue, S. Masubuchi, S. Morikawa, M. Onuki, K. Watanabe, T. Taniguchi, R. Moriya, and T. Machida, “Electrical Spin Injection into Graphene through Monolayer Hexagonal Boron Nitride”, *Applied Physics Express* **6**, 073001 (2013).
- [70] A. Dankert, M. V. Kamalakar, J. Bergsten, and S. P. Dash, “Spin transport and precession in graphene measured by nonlocal and three-terminal methods”, *Applied Physics Letters* **104**, 192403 (2014).
- [71] A. L. Friedman, O. M. J. van ’t Erve, C. H. Li, J. T. Robinson, and B. T. Jonker, “Homoepitaxial tunnel barriers with functionalized graphene-on-graphene for charge and spin transport”, *Nature Communications* **5**, 3161 (2014).
- [72] M. Drögeler, F. Volmer, M. Wolter, B. Terrés, K. Watanabe, T. Taniguchi, G. Güntherodt, C. Stampfer, and B. Beschoten, “Nanosecond Spin Lifetimes in Single- and Few-Layer Graphene-hBN Heterostructures at Room Temperature”, *Nano Letters* **14**, 6050–6055 (2014).
- [73] M. V. Kamalakar, A. Dankert, J. Bergsten, T. Ive, and S. P. Dash, “Enhanced Tunnel Spin Injection into Graphene using Chemical Vapor Deposited Hexagonal Boron Nitride”, *Scientific Reports* **4**, 6146 (2015).

- 
- [74] W. Fu, P. Makk, R. Maurand, M. Bräuninger, and C. Schönenberger, “Large-scale fabrication of BN tunnel barriers for graphene spintronics”, *Journal of Applied Physics* **116**, 074306 (2014).
  - [75] M. V. Kamalakar, A. Dankert, J. Bergsten, T. Ive, and S. P. Dash, “Spintronics with graphene-hexagonal boron nitride van der Waals heterostructures”, *Applied Physics Letters* **105**, 212405 (2014).
  - [76] S. Singh, J. Katoch, T. Zhu, R. J. Wu, A. S. Ahmed, W. Amamou, D. Wang, K. A. Mkhoyan, and R. K. Kawakami, “Strontium Oxide Tunnel Barriers for High Quality Spin Transport and Large Spin Accumulation in Graphene”, *Nano Letters* **17**, 7578–7585 (2017).
  - [77] Y. Anugrah, J. Hu, G. Stecklein, P. A. Crowell, and S. J. Koester, “Independent gate control of injected and detected spin currents in CVD graphene nonlocal spin valves”, *AIP Advances* **8**, 015129 (2018).
  - [78] B. Behin-Aein, D. Datta, S. Salahuddin, and S. Datta, “Proposal for an all-spin logic device with built-in memory”, *Nature Nanotechnology* **5**, 266–270 (2010).
  - [79] S. Srinivasan, A. Sarkar, B. Behin-Aein, and S. Datta, “All-spin logic device with inbuilt nonreciprocity”, in *IEEE Transactions on Magnetics*, Vol. 47, 10 (2011), pp. 4026–4032.
  - [80] H. Dery, P. Dalal, Cywiński, and L. J. Sham, “Spin-based logic in semiconductors for reconfigurable large-scale circuits”, *Nature* **447**, 573–576 (2007).
  - [81] H. Dery, H. Wu, B. Ciftcioglu, M. Huang, Y. Song, R. Kawakami, J. Shi, I. Krivorotov, I. Žutić, and L. J. Sham, “Nanospintronics based on magnetologic gates”, *IEEE Transactions on Electron Devices* **59**, 259–262 (2012).
  - [82] L. Su, W. Zhao, Y. Zhang, D. Querlioz, Y. Zhang, J. O. Klein, P. Dollfus, and A. Bournel, “Proposal for a graphene-based all-spin logic gate”, *Applied Physics Letters* **106**, 072407 (2015).
  - [83] Q. An, L. Su, J. O. Klein, S. Le Beux, I. O’Connor, and W. Zhao, “Full-adder circuit design based on all-spin logic device”, in *Proceedings of the 2015 IEEE/ACM International Symposium on Nanoscale Architectures, NANOARCH 2015* (2015), pp. 163–168.
  - [84] S. Manipatruni, D. E. Nikonov, C. C. Lin, T. A. Gosavi, H. Liu, B. Prasad, Y. L. Huang, E. Bonturim, R. Ramesh, and I. A. Young, “Scalable energy-efficient magnetoelectric spin-orbit logic”, *Nature* **565**, 35–42 (2019).
  - [85] H. M. Sheffer, “A set of five independent postulates for Boolean algebras, with application to logical constants”, *Transactions of the American Mathematical Society* **14**, 481–481 (1913).

- [86] H. Wen, H. Dery, W. Amamou, T. Zhu, Z. Lin, J. Shi, I. Žutić, I. Krivorotov, L. J. Sham, and R. K. Kawakami, “Experimental Demonstration of xor Operation in Graphene Magnetologic Gates at Room Temperature”, *Physical Review Applied* **5**, 44003 (2016).
- [87] R. Ishihara, Y. Ando, S. Lee, R. Ohshima, M. Goto, S. Miwa, Y. Suzuki, H. Koike, and M. Shiraishi, “Gate-Tunable Spin xor Operation in a Silicon-Based Device at Room Temperature”, *Physical Review Applied* **13**, 044010 (2020).
- [88] Y. Acremann, X. W. Yu, A. A. Tulapurkar, A. Scherz, V. Chembrolu, J. A. Katine, M. J. Carey, H. C. Siegmann, and J. Stöhr, “An amplifier concept for spintronics”, *Applied Physics Letters* **93**, 102513 (2008).
- [89] C. C. Lin, A. V. Penumatcha, Y. Gao, V. Q. Diep, J. Appenzeller, and Z. Chen, “Spin transfer torque in a graphene lateral spin valve assisted by an external magnetic field”, *Nano Letters* **13**, 5177–5181 (2013).
- [90] C. C. Lin, Y. Gao, A. V. Penumatcha, V. Q. Diep, J. Appenzeller, and Z. Chen, “Improvement of spin transfer torque in asymmetric graphene devices”, *ACS Nano* **8**, 3807–3812 (2014).
- [91] M. König, S. Wiedmann, C. Brüne, A. Roth, H. Buhmann, L. W. Molenkamp, X. L. Qi, and S. C. Zhang, “Quantum spin hall insulator state in HgTe quantum wells”, *Science* **318**, 766–770 (2007).
- [92] S. Wu, V. Fatemi, Q. D. Gibson, K. Watanabe, T. Taniguchi, R. J. Cava, and P. Jarillo-Herrero, “Observation of the quantum spin Hall effect up to 100 kelvin in a monolayer crystal”, *Science* **359**, 76–79 (2018).
- [93] D Hsieh, Y Xia, D Qian, L Wray, F Meier, J. H. Dil, J Osterwalder, L Patthey, A. V. Fedorov, H Lin, A Bansil, D Grauer, Y. S. Hor, R. J. Cava, and M. Z. Hasan, “Observation of time-reversal-protected single-dirac-cone topological-insulator states in Bi<sub>2</sub>Te<sub>3</sub> and Sb<sub>2</sub>Te<sub>3</sub>”, *Physical Review Letters* **103** (2009) 10.1103/PhysRevLett.103.146401.
- [94] Y Xia, D Qian, D Hsieh, L Wray, A Pal, H Lin, A Bansil, D Grauer, Y. S. Hor, R. J. Cava, and M. Z. Hasan, “Observation of a large-gap topological-insulator class with a single Dirac cone on the surface”, *Nature Physics* **5**, 398–402 (2009).
- [95] D. Hsieh et al., “A tunable topological insulator in the spin helical Dirac transport regime”, *Nature* **460**, 1101–1105 (2009).
- [96] X. L. Qi and S. C. Zhang, “The quantum spin Hall effect and topological insulators”, *Physics Today* **63**, 33–38 (2010).
- [97] Y. Shi, J. Kahn, B. Niu, Z. Fei, B. Sun, X. Cai, B. A. Francisco, D. Wu, Z.-X. Shen, X. Xu, D. H. Cobden, and Y.-T. Cui, “Imaging quantum spin Hall edges in monolayer WTe<sub>2</sub>”, *Science Advances* **5**, eaat8799 (2019).

- 
- [98] C. Z. Chang et al., “Experimental observation of the quantum anomalous Hall effect in a magnetic topological Insulator”, *Science* **340**, 167–170 (2013).
  - [99] L. Fu and C. L. Kane, “Topological insulators with inversion symmetry”, *Physical Review B - Condensed Matter and Materials Physics* **76**, 045302 (2007).
  - [100] L. Fu, C. L. Kane, and E. J. Mele, “Topological insulators in three dimensions”, *Physical Review Letters* **98**, 106803 (2007).
  - [101] Y. L. Chen, J. G. Analytis, J.-H. Chu, Z. K. Liu, S.-K. Mo, X. L. Qi, H. J. Zhang, D. H. Lu, X. Dai, Z. Fang, S. C. Zhang, I. R. Fisher, Z. Hussain, and Z.-X. Shen, “Experimental Realization of a Three-Dimensional Topological Insulator,  $\text{Bi}_2\text{Te}_3$ ”, *Science* **325**, 178–181 (2009).
  - [102] Z. Ren, A. A. Taskin, S. Sasaki, K. Segawa, and Y. Ando, “Optimizing  $\text{Bi}_{2-x}\text{Sb}_x\text{Te}_{3-y}\text{Se}_y$  solid solutions to approach the intrinsic topological insulator regime”, *Physical Review B - Condensed Matter and Materials Physics* **84**, 165311 (2011).
  - [103] C. H. Li, O. M. J. van ’t Erve, J. T. Robinson, Y. Liu, L. Li, and B. T. Jonker, “Electrical detection of charge-current-induced spin polarization due to spin-momentum locking in  $\text{Bi}_2\text{Se}_3$ ”, *Nature Nanotechnology* **9**, 218–224 (2014).
  - [104] A. Dankert, J. Geurs, M. V. Kamalakar, S. Charpentier, and S. P. Dash, “Room Temperature Electrical Detection of Spin Polarized Currents in Topological Insulators”, *Nano Letters* **15**, 7976–7981 (2015).
  - [105] J. S. Lee, A. Richardella, D. R. Hickey, K. A. Mkhoyan, and N. Samarth, “Mapping the chemical potential dependence of current-induced spin polarization in a topological insulator”, *Physical Review B* **92**, 155312 (2015).
  - [106] A. R. Mellnik, J. S. Lee, A. Richardella, J. L. Grab, P. J. Mintun, M. H. Fischer, A. Vaezi, A. Manchon, E.-A. Kim, N. Samarth, and D. C. Ralph, “Spin-transfer torque generated by a topological insulator”, *Nature* **511**, 449–451 (2014).
  - [107] Y. Fan et al., “Magnetization switching through giant spin-orbit torque in a magnetically doped topological insulator heterostructure”, *Nature Materials* **13**, 699–704 (2014).
  - [108] J. Han, A. Richardella, S. A. Siddiqui, J. Finley, N. Samarth, and L. Liu, “Room-Temperature Spin-Orbit Torque Switching Induced by a Topological Insulator”, *Physical Review Letters* **119**, 077702 (2017).

- [109] J.-C. Rojas-Sánchez, S Oyarzún, Y Fu, A Marty, C Vergnaud, S Gambarelli, L Vila, M Jamet, Y Ohtsubo, A Taleb-Ibrahimi, P Le Fèvre, F Bertran, N Reyren, J.-M. George, and A Fert, “Spin to Charge Conversion at Room Temperature by Spin Pumping into a New Type of Topological Insulator:  $\alpha$ -Sn Films”, *Physical Review Letters* **116**, 96602 (2016).
- [110] K. Kondou, R. Yoshimi, A. Tsukazaki, Y. Fukuma, J. Matsuno, K. S. Takahashi, M. Kawasaki, Y. Tokura, and Y. Otani, “Fermi-level-dependent charge-to-spin current conversion by Dirac surface states of topological insulators”, *Nature Physics* **12**, 1027–1031 (2016).
- [111] Y. Wang, D. Zhu, Y. Wu, Y. Yang, J. Yu, R. Ramaswamy, R. Mishra, S. Shi, M. Elyasi, K.-L. Teo, Y. Wu, and H. Yang, “Room temperature magnetization switching in topological insulator-ferromagnet heterostructures by spin-orbit torques”, *Nature Communications* **8**, 1364 (2017).
- [112] N. H. D. Khang, Y. Ueda, and P. N. Hai, “A conductive topological insulator with large spin Hall effect for ultralow power spin-orbit torque switching”, *Nature Materials* **17**, 808–813 (2018).
- [113] Y. Ando, T. Hamasaki, T. Kurokawa, K. Ichiba, F. Yang, M. Novak, S. Sasaki, K. Segawa, Y. Ando, and M. Shiraishi, “Electrical Detection of the Spin Polarization Due to Charge Flow in the Surface State of the Topological Insulator  $\text{Bi}_{1.5}\text{Sb}_{0.5}\text{Te}_{1.7}\text{Se}_{1.3}$ ”, *Nano Letters* **14**, 6226–6230 (2014).
- [114] J. Tian, I. Childres, H. Cao, T. Shen, I. Miotkowski, and Y. P. Chen, “Topological insulator based spin valve devices: Evidence for spin polarized transport of spin-momentum-locked topological surface states”, *Solid State Communications* **191**, 1–5 (2014).
- [115] J. Tang, L.-T. Chang, X. Kou, K. Murata, E. S. Choi, M. Lang, Y. Fan, Y. Jiang, M. Montazeri, W. Jiang, Y. Wang, L. He, and K. L. Wang, “Electrical Detection of Spin-Polarized Surface States Conduction in  $(\text{Bi}_{0.53}\text{Sb}_{0.47})_2\text{Te}_3$  Topological Insulator”, *Nano Letters* **14**, 5423–5429 (2014).
- [116] K. Vaklinova, A. Hoyer, M. Burghard, and K. Kern, “Current-Induced Spin Polarization in Topological Insulator-Graphene Heterostructures”, *Nano Letters* **16**, 2595–2602 (2016).
- [117] E. K. De Vries, A. M. Kamerbeek, N. Koirala, M. Brahlek, M. Salehi, S. Oh, B. J. Van Wees, and T. Banerjee, “Towards the understanding of the origin of charge-current-induced spin voltage signals in the topological insulator  $\text{Bi}_2\text{Se}_3$ ”, *Physical Review B - Condensed Matter and Materials Physics* **92**, 201102 (2015).
- [118] J. A. Voerman, C. Li, Y. Huang, and A. Brinkman, “Spin-Momentum Locking in the Gate Tunable Topological Insulator  $\text{BiSbTeSe}_2$  in Non-Local Transport Measurements”, *Advanced Electronic Materials* **5**, 1900334 (2019).



- 
- [119] A. H. Castro Neto and F. Guinea, “Impurity-induced spin-orbit coupling in graphene”, *Physical Review Letters* **103**, 026804 (2009).
  - [120] K. Pi, W. Han, K. M. McCreary, A. G. Swartz, Y. Li, and R. K. Kawakami, “Manipulation of spin transport in graphene by surface chemical doping”, *Physical Review Letters* **104**, 187201 (2010).
  - [121] M. Wojtaszek, I. J. Vera-Marun, T. Maassen, and B. J. Van Wees, “Enhancement of spin relaxation time in hydrogenated graphene spin-valve devices”, *Physical Review B - Condensed Matter and Materials Physics* **87**, 081402 (2013).
  - [122] J. Balakrishnan, G. Kok Wai Koon, M. Jaiswal, A. H. Castro Neto, and B. Özyilmaz, “Colossal enhancement of spin-orbit coupling in weakly hydrogenated graphene”, *Nature Physics* **9**, 284–287 (2013).
  - [123] M. Gmitra, D. Kochan, and J. Fabian, “Spin-orbit coupling in hydrogenated graphene”, *Physical Review Letters* **110**, 246602 (2013).
  - [124] J. Balakrishnan, G. K. W. Koon, A. Avsar, Y. Ho, J. H. Lee, M. Jaiswal, S. J. Baeck, J. H. Ahn, A. Ferreira, M. A. Cazalilla, A. H. Neto, and B. Özyilmaz, “Giant spin Hall effect in graphene grown by chemical vapour deposition”, *Nature Communications* **5**, 1–7 (2014).
  - [125] D. Soriano, D. V. Tuan, S. M.-M. Dubois, M. Gmitra, A. W. Cummings, D. Kochan, F. Ortman, J.-C. Charlier, J. Fabian, and S. Roche, “Spin transport in hydrogenated graphene”, *2D Materials* **2**, 022002 (2015).
  - [126] C. R. Dean, L. Wang, P. Maher, C. Forsythe, F. Ghahari, Y. Gao, J. Katoch, M. Ishigami, P. Moon, M. Koshino, T. Taniguchi, K. Watanabe, K. L. Shepard, J. Hone, and P. Kim, “Hofstadter’s butterfly and the fractal quantum Hall effect in moiré superlattices”, *Nature* **497**, 598–602 (2013).
  - [127] B. Hunt, J. D. Sanchez-Yamagishi, A. F. Young, M. Yankowitz, B. J. LeRoy, K. Watanabe, T. Taniguchi, P. Moon, M. Koshino, P. Jarillo-Herrero, and R. C. Ashoori, “Massive dirac fermions and hofstadter butterfly in a van der Waals heterostructure”, *Science* **340**, 1427–1430 (2013).
  - [128] L. A. Ponomarenko et al., “Cloning of Dirac fermions in graphene superlattices”, *Nature* **497**, 594–597 (2013).
  - [129] A. Avsar, J. Y. Tan, T. Taychatanapat, J. Balakrishnan, G. Koon, Y. Yeo, J. Lahiri, A. Carvalho, A. S. Rodin, E. O’Farrell, G. Eda, A. H. Castro Neto, and B. Özyilmaz, “Spin-orbit proximity effect in graphene”, *Nature Communications* **5**, 4875 (2014).
  - [130] Z. Wang, D. Ki, H. Chen, H. Berger, A. H. MacDonald, and A. F. Morpurgo, “Strong interface-induced spin-orbit interaction in graphene on WS<sub>2</sub>”, *Nature Communications* **6**, 8339 (2015).

- [131] M. Gmitra and J. Fabian, “Graphene on transition-metal dichalcogenides: A platform for proximity spin-orbit physics and optospintronics”, *Physical Review B - Condensed Matter and Materials Physics* **92**, 155403 (2015).
- [132] M. Gmitra, D. Kochan, P. Högl, and J. Fabian, “Trivial and inverted Dirac bands and the emergence of quantum spin Hall states in graphene on transition-metal dichalcogenides”, *Physical Review B* **93**, 155104 (2016).
- [133] Z. Wang, D.-K. Ki, J. Y. Khoo, D. Mauro, H. Berger, L. S. Levitov, and A. F. Morpurgo, “Origin and Magnitude of ‘Designer’ Spin-Orbit Interaction in Graphene on Semiconducting Transition Metal Dichalcogenides”, *Physical Review X* **6**, 041020 (2016).
- [134] B. Yang, M. Lohmann, D. Barroso, I. Liao, Z. Lin, Y. Liu, L. Bartels, K. Watanabe, T. Taniguchi, and J. Shi, “Strong electron-hole symmetric Rashba spin-orbit coupling in graphene/monolayer transition metal dichalcogenide heterostructures”, *Physical Review B* **96**, 041409 (2017).
- [135] M. Gmitra and J. Fabian, “Proximity Effects in Bilayer Graphene on Monolayer WSe<sub>2</sub>: Field-Effect Spin Valley Locking, Spin-Orbit Valve, and Spin Transistor”, *Physical Review Letters* **119**, 146401 (2017).
- [136] S Omar and B. J. van Wees, “Spin transport in high-mobility graphene on WS<sub>2</sub> substrate with electric-field tunable proximity spin-orbit interaction”, *Physical Review B* **97**, 45414 (2018).
- [137] S. Zihlmann, A. W. Cummings, J. H. Garcia, M. Kedves, K. Watanabe, T. Taniguchi, C. Schönenberger, and P. Makk, “Large spin relaxation anisotropy and valley-Zeeman spin-orbit coupling in WSe<sub>2</sub>/graphene/*h*-BN heterostructures”, *Physical Review B* **97**, 75434 (2018).
- [138] C. Song, W. Xiao, P. Lin, J. Wang, J. Pan, C. Cui, C. Li, and J. Wang, “Proximity exchange induced gap opening and topological feature in graphene / 1T'-MX<sub>2</sub> (M = Mo,W; X = S,Se,Te) Dirac heterostructures”, *Journal of Physics Condensed Matter* **30**, 275001 (2018).
- [139] J. O. Island, X. Cui, C. Lewandowski, J. Y. Khoo, E. M. Spanton, H. Zhou, D. Rhodes, J. C. Hone, T. Taniguchi, K. Watanabe, L. S. Levitov, M. P. Zaletel, and A. F. Young, “Spin-orbit-driven band inversion in bilayer graphene by the van der Waals proximity effect”, *Nature* **571**, 85–89 (2019).
- [140] Y. Li and M. Koshino, “Twist-angle dependence of the proximity spin-orbit coupling in graphene on transition-metal dichalcogenides”, *Physical Review B* **99**, 075438 (2019).
- [141] D. Wang, S. Che, G. Cao, R. Lyu, K. Watanabe, T. Taniguchi, C. N. Lau, and M. Bockrath, “Quantum Hall Effect Measurement of Spin-Orbit Coupling Strengths in Ultraclean Bilayer Graphene/WSe<sub>2</sub> Heterostructures”, *Nano Letters* **19**, 7028–7034 (2019).

- 
- [142] B. Fülöp, A. Márffy, S. Zihlmann, M. Gmitra, E. Tóvári, B. Szentpéteri, M. Kedves, K. Watanabe, T. Taniguchi, J. Fabian, C. Schönenberger, P. Makk, and S. Csonka, “Boosting proximity spin orbit coupling in graphene/WSe<sub>2</sub> heterostructures via hydrostatic pressure”, arXiv, 2103.13325 (2021).
  - [143] M. Gmitra, S. Konschuh, C. Ertler, C. Ambrosch-Draxl, and J. Fabian, “Band-structure topologies of graphene: Spin-orbit coupling effects from first principles”, *Physical Review B - Condensed Matter and Materials Physics* **80**, 235431 (2009).
  - [144] K. Zollner, M. Gmitra, and J. Fabian, “Swapping Exchange and Spin-Orbit Coupling in 2D van der Waals Heterostructures”, *Physical Review Letters* **125**, 196402 (2020).
  - [145] W. Yan, O. Txoperena, R. Llopis, H. Dery, L. E. Hueso, and F. Casanova, “A two-dimensional spin field-effect switch”, *Nature Communications* **7**, 13372 (2016).
  - [146] A. Dankert and S. P. Dash, “Electrical gate control of spin current in van der Waals heterostructures at room temperature”, *Nature Communications* **8**, 16093 (2017).
  - [147] N Tombros, S Tanabe, A Veligura, C Jozsa, M Popinciuc, H. T. Jonkman, and B. J. van Wees, “Anisotropic Spin Relaxation in Graphene”, *Physical Review Letters* **101**, 46601 (2008).
  - [148] B. Raes, J. E. Scheerder, M. V. Costache, F. Bonell, J. F. Sierra, J. Cuppens, J. Van de Vondel, and S. O. Valenzuela, “Determination of the spin-lifetime anisotropy in graphene using oblique spin precession”, *Nature Communications* **7**, 11444 (2016).
  - [149] S. Ringer, S. Hartl, M. Rosenauer, T. Völkl, M. Kadur, F. Hopperdietzel, D. Weiss, and J. Eroms, “Measuring anisotropic spin relaxation in graphene”, *Physical Review B* **97**, 205439 (2018).
  - [150] J. C. Leutenantsmeyer, J. Ingla-Aynés, J. Fabian, and B. J. van Wees, “Observation of Spin-Valley-Coupling-Induced Large Spin-Lifetime Anisotropy in Bilayer Graphene”, *Physical Review Letters* **121**, 127702 (2018).
  - [151] J. Xu, T. Zhu, Y. K. Luo, Y.-M. Lu, and R. K. Kawakami, “Strong and Tunable Spin-Lifetime Anisotropy in Dual-Gated Bilayer Graphene”, *Physical Review Letters* **121**, 127703 (2018).
  - [152] M. Offidani, M. Milletari, R. Raimondi, and A. Ferreira, “Optimal Charge-to-Spin Conversion in Graphene on Transition-Metal Dichalcogenides”, *Physical Review Letters* **119** (2017) 10.1103/PhysRevLett.119.196801.
  - [153] J. H. Garcia, A. W. Cummings, and S. Roche, “Spin Hall Effect and Weak Antilocalization in Graphene/Transition Metal Dichalcogenide Heterostructures”, *Nano Letters* **17**, 5078–5083 (2017).

- [154] L. A. Benítez, J. F. Sierra, W. Savero Torres, A. Arrighi, F. Bonell, M. V. Costache, and S. O. Valenzuela, “Strongly anisotropic spin relaxation in graphene-transition metal dichalcogenide heterostructures at room temperature”, *Nature Physics* **14**, 303–308 (2018).
- [155] A. W. Cummings, J. H. Garcia, J. Fabian, and S. Roche, “Giant Spin Lifetime Anisotropy in Graphene Induced by Proximity Effects”, *Physical Review Letters* **119**, 206601 (2017).
- [156] T. S. Ghiasi, J. Ingla-Aynés, A. A. Kaverzin, and B. J. van Wees, “Large Proximity-Induced Spin Lifetime Anisotropy in Transition-Metal Dichalcogenide/Graphene Heterostructures”, *Nano Letters* **17**, 7528–7532 (2017).
- [157] L. A. Benítez, J. F. Sierra, W. Savero Torres, M. Timmermans, M. V. Costache, and S. O. Valenzuela, “Investigating the spin-orbit interaction in van der Waals heterostructures by means of the spin relaxation anisotropy”, *APL Materials* **7**, 120701 (2019).
- [158] J. Sinova, S. O. Valenzuela, J. Wunderlich, C. H. Back, and T. Jungwirth, “Spin Hall effects”, *Reviews of Modern Physics* **87**, 1213–1260 (2015).
- [159] C. K. Safeer, J. Ingla-Aynés, F. Herling, J. H. Garcia, M. Vila, N. Ontoso, M. R. Calvo, S. Roche, L. E. Hueso, and F. Casanova, “Room-Temperature Spin Hall Effect in Graphene/MoS<sub>2</sub> van der Waals Heterostructures”, *Nano Letters* **19**, 1074–1082 (2019).
- [160] L. A. Benítez, W. Savero Torres, J. F. Sierra, M. Timmermans, J. H. Garcia, S. Roche, M. V. Costache, and S. O. Valenzuela, “Tunable room-temperature spin galvanic and spin Hall effects in van der Waals heterostructures”, *Nature Materials* **19**, 170–175 (2020).
- [161] C. K. Safeer, N. Ontoso, J. Ingla-Aynés, F. Herling, V. T. Pham, A. Kurzmam, K. Ensslin, A. Chuvilin, I. Robredo, M. G. Vergniory, F. De Juan, L. E. Hueso, M. R. Calvo, and F. Casanova, “Large Multidirectional Spin-to-Charge Conversion in Low-Symmetry Semimetal MoTe<sub>2</sub> at Room Temperature”, *Nano Letters* **19**, 8758–8766 (2019).
- [162] T. S. Ghiasi, A. A. Kaverzin, P. J. Blah, and B. J. van Wees, “Charge-to-Spin Conversion by the Rashba-Edelstein Effect in Two-Dimensional van der Waals Heterostructures up to Room Temperature”, *Nano Letters* **19**, 5959–5966 (2019).
- [163] F. Herling, C. K. Safeer, J. Ingla-Aynés, N. Ontoso, L. E. Hueso, and F. Casanova, “Gate tunability of highly efficient spin-to-charge conversion by spin Hall effect in graphene proximitized with WSe<sub>2</sub>”, *APL Materials* **8**, 071103 (2020).

- 
- [164] C. K. Safeer, J. Ingla-Aynés, N. Ontoso, F. Herling, W. Yan, W. Yan, L. E. Hueso, L. E. Hueso, F. Casanova, and F. Casanova, “Spin Hall Effect in Bilayer Graphene Combined with an Insulator up to Room Temperature”, *Nano Letters* **20**, 4573–4579 (2020).
- [165] W. Yan, E. Sagasta, M. Ribeiro, Y. Niimi, L. E. Hueso, and F. Casanova, “Large room temperature spin-to-charge conversion signals in a few-layer graphene/Pt lateral heterostructure”, *Nature Communications* **8**, 1–7 (2017).
- [166] L. Li, J. Zhang, G. Myeong, W. Shin, H. Lim, B. Kim, S. Kim, T. Jin, S. Cavill, B. S. Kim, C. Kim, J. Lischner, A. Ferreira, and S. Cho, “Gate-Tunable Reversible Rashba-Edelstein Effect in a Few-Layer Graphene/2H-TaS<sub>2</sub> Heterostructure at Room Temperature”, *ACS Nano* **14**, 5251–5259 (2020).
- [167] S. D. Ganichev, E. L. Ivchenko, V. V. Bel’kov, S. A. Tarasenko, M Sollinger, D Weiss, W Wegscheider, and W Prettel, “Spin-galvanic effect”, *Nature* **417**, 153–156 (2002).
- [168] D. Pesin and A. H. MacDonald, “Spintronics and pseudospintronics in graphene and topological insulators”, *Nature Materials* **11**, 409–416 (2012).
- [169] K. Song, D. Soriano, A. W. Cummings, R. Robles, P. Ordejón, and S. Roche, “Spin Proximity Effects in Graphene/Topological Insulator Heterostructures”, *Nano Letters* **18**, 2033–2039 (2018).
- [170] J. Zhang, C Triola, and E Rossi, “Proximity Effect in Graphene-Topological-Insulator Heterostructures”, *Physical Review Letters* **112**, 096802 (2014).
- [171] L. Kou, F. Hu, B. Yan, T. Wehling, C. Felser, T. Frauenheim, and C. Chen, “Proximity enhanced quantum spin Hall state in graphene”, *Carbon* **87**, 418–423 (2015).
- [172] L. Kou, B. Yan, F. Hu, S.-C. Wu, T. O. Wehling, C. Felser, C. Chen, and T. Frauenheim, “Graphene-Based Topological Insulator with an Intrinsic Bulk Band Gap above Room Temperature”, *Nano Letters* **13**, 6251–6255 (2013).
- [173] M Rodriguez-Vega, G Schwiete, J Sinova, and E Rossi, “Giant Edelstein effect in topological-insulator-graphene heterostructures”, *Physical Review B* **96**, 235419 (2017).
- [174] W. Cao, R.-X. Zhang, P. Tang, G. Yang, J. Sofo, W. Duan, and C.-X. Liu, “Heavy Dirac fermions in a graphene/topological insulator heterojunction”, *2D Materials* **3**, 034006 (2016).
- [175] S. Rajput, Y.-Y. Li, M. Weinert, and L. Li, “Indirect Interlayer Bonding in Graphene-Topological Insulator van der Waals Heterostructure: Giant Spin-Orbit Splitting of the Graphene Dirac States”, *ACS Nano* **10**, 8450–8456 (2016).

- [176] I. Popov, M. Mantega, A. Narayan, and S. Sanvito, “Proximity-induced topological state in graphene”, *Physical Review B* **90**, 035418 (2014).
- [177] K. H. Jin and S. H. Jhi, “Proximity-induced giant spin-orbit interaction in epitaxial graphene on a topological insulator”, *Physical Review B - Condensed Matter and Materials Physics* **87**, 75442 (2013).
- [178] K. Zollner and J. Fabian, “Single and bilayer graphene on the topological insulator  $\text{Bi}_2\text{Se}_3$ : Electronic and spin-orbit properties from first principles”, *Physical Review B* **100**, 165141 (2019).
- [179] C De Beule, M Zarenia, and B Partoens, “Transmission in graphene-topological insulator heterostructures”, *Physical Review B* **95**, 1–11 (2017).
- [180] K. Zollner and J. Fabian, “Heterostructures of Graphene and Topological Insulators  $\text{Bi}_2\text{Se}_3$ ,  $\text{Bi}_2\text{Te}_3$ , and  $\text{Sb}_2\text{Te}_3$ ”, *Physica Status Solidi (B) Basic Research* **258**, 2000081 (2021).
- [181] P. Lee, K.-h. Jin, S. J. Sung, J. G. Kim, M.-t. Ryu, H.-m. Park, S.-h. Jhi, N. Kim, Y. Kim, S. U. Yu, K. S. Kim, D. Y. Noh, J. Chung, and L. E.E.E. T. Al, “Proximity Effect Induced Electronic Properties of Graphene on  $\text{Bi}_2\text{Te}_2\text{Se}$ ”, *ACS Nano* **9**, 10861–10866 (2015).
- [182] X. Chen, X.-C. Ma, K. He, J.-F. Jia, and Q.-K. Xue, “Molecular Beam Epitaxial Growth of Topological Insulators”, *Advanced Materials* **23**, 1162–1165 (2011).
- [183] H Steinberg, L. A. Orona, V Fatemi, J. D. Sanchez-Yamagishi, K Watanabe, T Taniguchi, and P Jarillo-Herrero, “Tunneling in graphene-topological insulator hybrid devices”, *Physical Review B* **92**, 241409 (2015).
- [184] L. Zhang, Y. Yan, H. C. Wu, D. Yu, and Z. M. Liao, “Gate-Tunable Tunneling Resistance in Graphene/Topological Insulator Vertical Junctions”, *ACS Nano* **10**, 3816–3822 (2016).
- [185] S. Jafarpisheh, A. W. Cummings, K. Watanabe, T. Taniguchi, B. Beschoten, and C. Stampfer, “Proximity-induced spin-orbit coupling in graphene /  $\text{Bi}_{1.5}\text{Sb}_{0.5}\text{Te}_{1.7}\text{Se}_{1.3}$  heterostructures”, *Physical Review B* **98**, 241402 (2018).
- [186] L. Zhang, B. C. Lin, Y. F. Wu, H. C. Wu, T. W. Huang, C. R. Chang, X. Ke, M. Kurttepeli, G. V. Tendeloo, J. Xu, D. Yu, and Z. M. Liao, “Electronic Coupling between Graphene and Topological Insulator Induced Anomalous Magnetotransport Properties”, *ACS Nano* **11**, 6277–6285 (2017).
- [187] T Maassen, F. K. Dejene, M. H. D. Guimarães, C Józsa, and B. J. van Wees, “Comparison between charge and spin transport in few-layer graphene”, *Physical Review B* **83**, 115410 (2011).

- 
- [188] B. Zhao, D. Khokhriakov, B. Karpiak, A. M. Hoque, L. Xu, L. Shen, Y. P. Feng, X. Xu, Y. Jiang, and S. P. Dash, “Electrically controlled spin-switch and evolution of Hanle spin precession in graphene”, *2D Materials* **6**, 035042 (2019).
  - [189] M. Johnson and R. H. Silsbee, “Calculation of nonlocal baseline resistance in a quasi-one-dimensional wire”, *Physical Review B* **76**, 153107 (2007).
  - [190] F. L. Bakker, A. Slachter, J. P. Adam, and B. J. Van Wees, “Interplay of peltier and seebeck effects in nanoscale nonlocal spin valves”, *Physical Review Letters* **105** (2010) 10.1103/PhysRevLett.105.136601.
  - [191] T. Ariki, T. Nomura, K. Ohnishi, and T. Kimura, “Effective suppression of thermoelectric voltage in nonlocal spin-valve measurement”, *Applied Physics Express* **10** (2017) 10.7567/APEX.10.063004.
  - [192] C. H. Li, O. M. J. van ’t Erve, Y. Y. Li, L. Li, and B. T. Jonker, “Electrical Detection of the Helical Spin Texture in a p-type Topological Insulator Sb<sub>2</sub>Te<sub>3</sub>”, *Scientific Reports* **6**, 29533 (2016).
  - [193] S Hikami, A. I. Larkin, and Y Nagaoka, “Spin-Orbit Interaction and Magnetoresistance in the Two Dimensional Random System”, *Progress of Theoretical Physics* **63**, 707–710 (1980).
  - [194] S. P. Dash, S. Sharma, J. C. Le Breton, J. Peiro, H. Jaffrès, J. M. George, A. Lemaître, and R. Jansen, “Spin precession and inverted Hanle effect in a semiconductor near a finite-roughness ferromagnetic interface”, *Physical Review B - Condensed Matter and Materials Physics* **84**, 054410 (2011).
  - [195] P. Zhang and M. W. Wu, “Electron spin relaxation in graphene with random Rashba field: Comparison of the D’yakonov-Perel’ and Elliott-Yafet-like mechanisms”, *New Journal of Physics* **14**, 33015 (2012).
  - [196] H. Ochoa, A. H. Castro Neto, and F. Guinea, “Elliot-Yafet Mechanism in Graphene”, *Physical Review Letters* **108**, 206808 (2012).
  - [197] J. C. R. Sánchez, L Vila, G Desfonds, S Gambarelli, J. P. Attané, J. M. De Teresa, C Magén, and A Fert, “Spin-to-charge conversion using Rashba coupling at the interface between non-magnetic materials”, *Nature Communications* **4**, 2944 (2013).
  - [198] E. Lesne et al., “Highly efficient and tunable spin-to-charge conversion through Rashba coupling at oxide interfaces”, *Nature Materials* **15**, 1261–1266 (2016).
  - [199] F. He, Y. Zhou, Z. Ye, S.-H. Cho, J. Jeong, X. Meng, and Y. Wang, “Moiré Patterns in 2D Materials: A Review”, *ACS Nano*, acsnano.0c10435 (2021).

